POLITECNICO DI TORINO

Master's Degree in
AUTOMOTIVE ENGINEERING

Master's Degree Thesis

A.Y. 2023/2024

Kinematic and dynamic modelling of an innovative softening vehicle suspension

Supervisors

Prof. Carlo Rosso
Dott. Simone Venturini

Candidate

Chuansong Zhang

March 2024

Kinematic and dynamic modelling of an innovative softening vehicle suspension

Chuansong Zhang

Politecnico di Torino, Department of Mechanical and Aerospace Engineering
Corso Duca degli Abruzzi, 24 – 10129 Torino, Italy

Index

Abstract

The objective of this study is to present a novel suspension topology for vehicles, designed to significantly enhance ride comfort while simultaneously maintain the satisfactory handling performance by incorporating an effective variable stiffness mechanism. The innovative suspension structure allows for fine-tuning the suspension without altering the suspension kinematics. This theoretical analysis begins by proposing the fundamental principles of the revolutionary suspension. The construction of the equivalent quadrilateral structure is followed by the presentation of Free Body Diagrams (FBDs) to assess the effectiveness of the novel mechanism. The initial physical model, excluding inertia effects, is established to reveal the inherent softening characteristics. Subsequently, a detailed explanation of the inertia of all elements refines the model, and reasonable approximations are made for simplification. The kinematic modal of the equivalent structure is then derived, which evaluates the equivalent stiffness of this system. The dynamics of the physical model are considered based on the system's equation of motion (EOM), resulting in the creation of the system's dynamical model. Nonlinear features of the novel structure are identified through the evaluation of three nonlinear functions $f_1(h), f_2(h), f_3(h)$, within the EOM. The dynamic performance of the system is examined by analysing the linearized response at three specific positions within the structure, as it is difficult to analyse the nonlinear system's vibration response when the jump phenomenon occurs. This simplified evaluation provides insights into the transformation of the nonlinear response across various positions, and by doing so, a comprehensive understanding of the nonlinear structure is achieved, leading to the development of a nonlinear dynamical model in Simulink to numerically estimate the nonlinear response. The subsequent phase proceeds to investigate the nonlinear step response of the system, the effectiveness of the novel equivalent suspension is discussed through comparison with the traditional linear suspension. Then, the instantaneous natural frequency of the nonlinear system is revealed by post-processing the system's nonlinear response using the Hilbert transform. In the final phase, a double-wishbone suspension based on a commercial product is encountered to visualise the proposed concept. The effect of the proposed structure is demonstrated by comparing the original linear spring with the equivalent nonlinear spring system, and the adaptability of the system to different suspension settings are discussed.

1. Introduction

The suspension links the entire vehicle and the road profile, which primarily composes of springs, shock absorbers and linkages, and acts like a filter between the road profile and the car body. The main tasks of the suspension system are to copy the road surfaces limiting the tyre fluctuation and providing a vertical compliance; to permit safe manoeuvres while maintaining the wheel control; to ensure that the vehicle reacts favourably to the external road forces; and to isolate the passengers from the road unevenness. Irregular terrain with lots of potholes, bumps and sudden impacts while driving, requires a sturdy and responsive suspension system in the vehicle. Although the study of the suspension design continues for decades already, many talents have brought some brilliant ideas to the automotive industry to either improve the dynamic performance or save the unsprang space, the design of the suspension still strikes a compromise between ride comfort and handling performance. Where, the ride comfort is considered as the motion environment involving the vehicle's vibration, shock, and translational and rotational accelerations in response to road excitations [1]; the handling refers to describe the lateral behaviour of a vehicle, the road holding ability pertaining to tire grip, and the agility and preciseness of the vehicle's response during manoeuvrings [2]. We have to admit that the design which perfects each suspension parameter simultaneously does not exist yet.

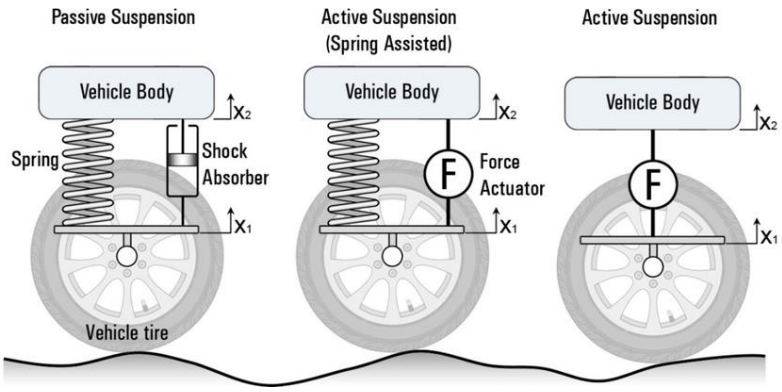

Figure 1.1 – Active suspension concept [4].

For the conflicting demand on ride comfort and good handling performance together, the compromised parameters tunning of passive suspensions has motivated the exploration of controlled suspension systems, including active and semi-active suspension. These systems have been created to address this conflict by adjusting various parameters online. Semi-active suspension is similar to a passive design with only difference being having a variable damper alongside a fixed spring [3]. An active suspension system has an actuator that can supply active force regulated by a controlling algorithm which uses information gathered from attached vehicle sensors, and the damping as well as stiffness are regulated through the application of actuator [3]. Extensive efforts have been paid to enhance the working efficiency and user satisfaction of the active suspension in the automotive industry, however, the enhanced ride and handling come at the cost of increased system complexity, high power consumption, and higher price. Despite the active suspension demonstrates superior performance among the three types, its widespread application is challenging and the passive suspension is still prevalent in the cars due to its simpler construction and affordable expanse.

Given the shortcomings of the passive suspension, it is sense to introduce an innovative structure which exhibits a high level of flexibility to adjust the characteristics of the suspension according to the design goals and a variable stiffness property to improve ride quality. Supposing that we want to isolate the car body further from road surface disturbances, which is accomplished via a relatively

low stiffness setting in a conventional suspension, as the investigation of the effect of spring stiffness on real vehicle performance did by Muhammad Zahir Hassan et al [5]. Reducing the stiffness would further improve the ride comfort by providing better isolation from the road surface, but it might adversely affect the vehicle handling as well as result in large static deformation, both unaffordable in road vehicles. To get around this issue, a nonlinear spring might combine a high load-bearing capacity with a low stiffness when subjected to light loads. The nonlinearity of the spring is incurred by an equivalent quadrilateral structure, whose geometry can be easily modified to achieve desired stiffness at the loaded position, meanwhile, with a simple structure and low cost. The remainder of this chapter presents the state-of-art about the variable stiffness suspension, and the underlying principle of our proposal.

1.1 State of art

It is evident that suspension performance significantly depends on the spring and damper, i.e., spring stiffness and damping coefficient. The canonical suspension system consists of passive spring and damper which are immutable once installed, the stiffness and damping coefficient are constant, little room for improvement in terms of suspension performance under different working scenarios. The damping performance of the suspension can be boosted by the semi-active and active suspension using variable dampers, such as MR damper and solenoid valve damper. However, obtaining variable stiffness in the suspension system is rarely mentioned which requires more complex mechanisms. Therefore, designing an equivalent spring system for vehicle suspension becomes crucial since its stiffness characteristics affect the car behaves on the road. Moreover, dynamically varying stiffness is possible to promote ride quality and ride stability, which calls for the use the suspensions with variable stiffness.

1.1.1 Springs with variable stiffness

Joseph Jerz Jr. [6] introduced a variable stiffness suspension system characterized by two springs arranged in series. Notably, one of the springs possesses greater stiffness than the other. Under normal load conditions, the softer spring comes into play, providing a delicately cushioned ride. However, when heavier loads are applied, the vehicle experiences stiffer support primarily from the stronger spring. Jacky Rhein [7] disclosed a variable stiffness suspension system with deformable bushings which imparts the variable stiffness characteristic. The bushing is made of elastomer material and a predefined thickness which determines the overall stiffness characteristic. This design ensures a comfortable experience during lighter loads and facilitates the creation of a more compact suspension mechanism, a significant advantage in rear axle design for motor vehicles. Conversely, this invention also makes it possible to stiffen the suspension when overloaded.

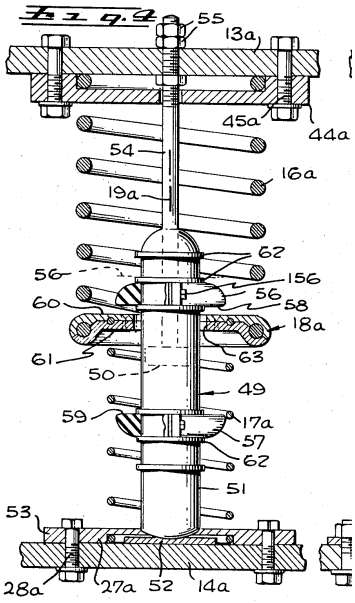

Figure 1.1.1.1 – Series Arrangement of Spring with Stopper and Flanges [6].

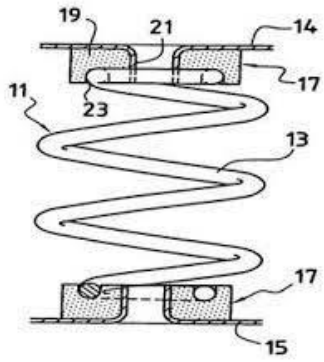

Figure 1.1.1.2 – Coil Spring with Compressible Bushings [7].

Substantial research has also been conducted on altering the spring rate in vehicle suspension systems, leading to the prevalence of two noteworthy types: the progressive spring and the dual-rate spring, illustrated in Figure 1.1.1.3. Compared to the linear rate spring, dual or progressive rate springs represent a practical compromise, striking a balance between low-speed comfort and preventing excessive bottoming out. Progressive springs offer a worthy advantage by significantly increasing in rate as compression extends beyond the ride height, which plays a crucial role in minimizing the impact force of axles on bump stops, making them a preferred choice for leading long-travel suspension cars. On the other hand, the dual-rate spring, a subtype of progressive rate springs, exhibits a distinctive progression—from a first rate (Firm Rate) to a second rate (Ride or Road Rate). This stands in contrast to the continuously changing rate of a traditional progressive rate spring. A dual-rate spring excels in providing a smoother rate of transition during compression and heavy load, while it introduces a potential trade-off in ride quality when reaching the top coils. Both progressive springs and dual rate springs, while offering enhanced performance characteristics, come with certain challenges. They tend to be more expensive to manufacture, harder to design, harder to inspect and lack the ride height consistency characteristic of linear rate springs.

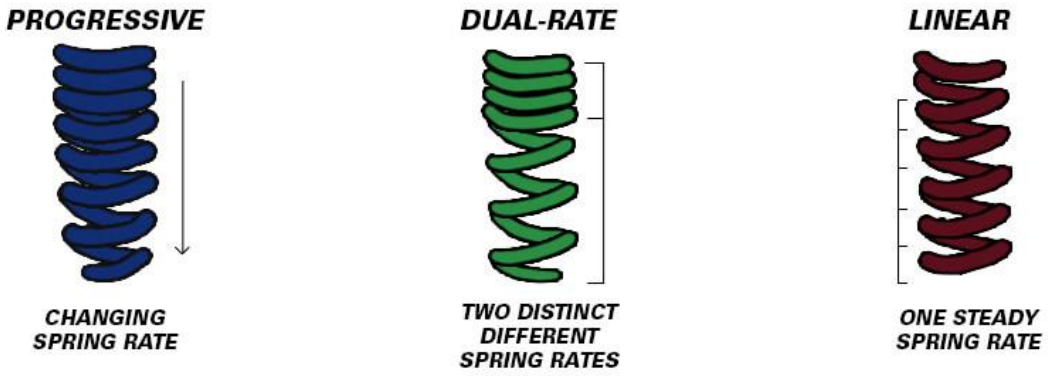

Figure 1.1.1.3 – Progressively spring, dual-rate spring, and linear rate spring [8].

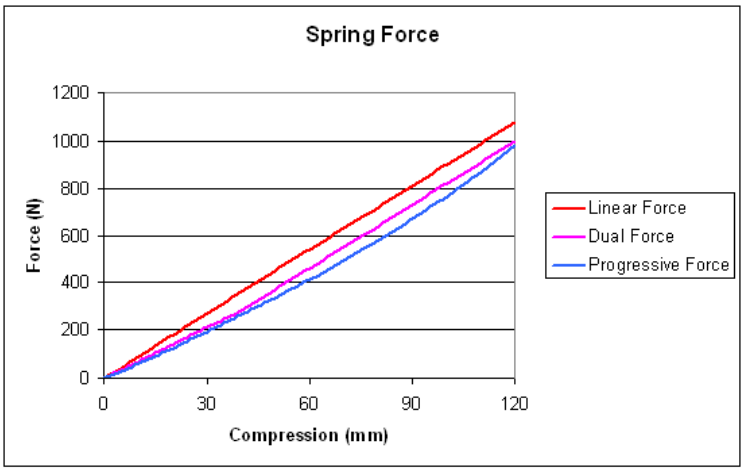

Figure 1.1.1.4 – Spring force with different types of spring under certain deformations [9].

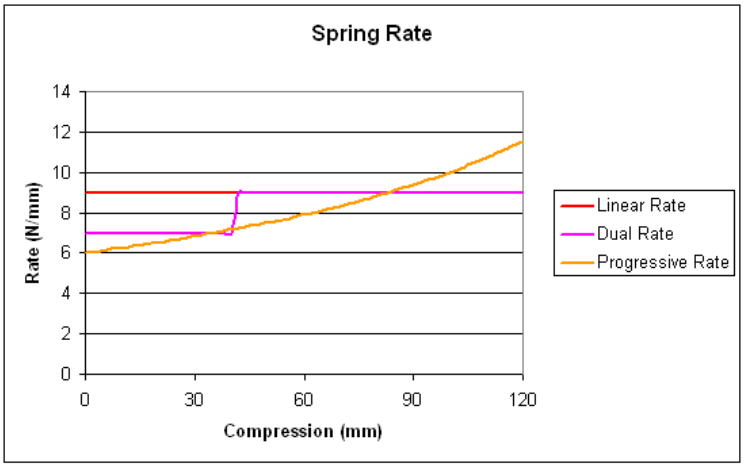

Figure 1.1.1.5 – Spring rate with different types of spring under certain deformations [9].

1.1.2 Variable stiffness suspension

Recent advancements in semi-active suspension systems have expanded beyond the consideration of damping performance alone, offering the opportunity to dynamically vary stiffness of the

suspension during operation. Yanqing Liu et al. proposed a concept of the suspension system featuring both variable stiffness and variable damping, achieved by incorporating a Voigt element in series with the linear spring [10]. Similarly, Shuaishuai Sun et al. proposed an innovative mechanism for variable stiffness utilizing a magnetorheological (MR) damper with two chambers and two springs in series as shown in Figure 1.1.2.2 [11]. In these mechanisms, the equivalent stiffness can be adjusted by manipulating the current in the two chambers. The equivalent stiffness is proportional to ratio of stiffness of two springs and to the current supplied to the MR damper chamber. The experimental research done on these newly proposed systems indicates superior performance compared to both passive and only variable damping suspensions. The ability to dynamically modify stiffness during operation represents a significant advancement, enhancing the adaptability and overall effectiveness of semi-active suspension systems in responding to varying road conditions and driving scenarios.

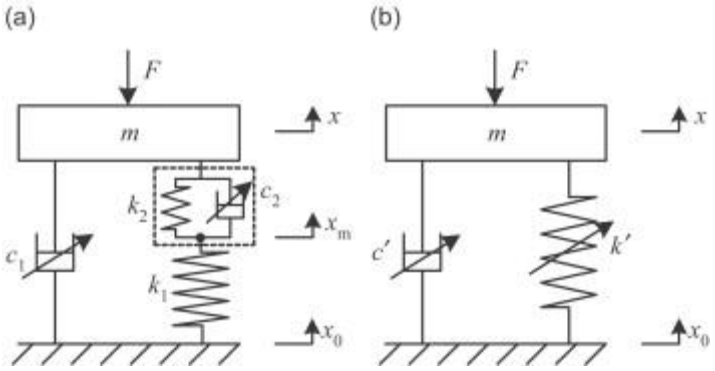

Figure 1.1.2.1 – Mechanical configuration of variable stiffness and damping: (a) original model and (b) equivalent model [10].

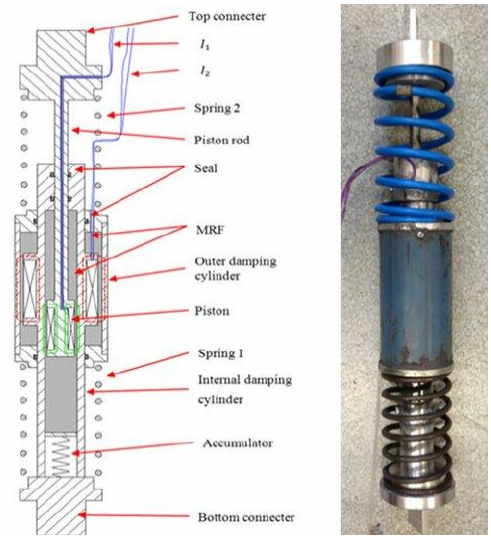

Figure 1.1.2.2 – Design and photograph of the variable stiffness shock absorber [11].

Anubi et al. [12] introduced a variable stiffness suspension system using a combination of horizontal and vertical suspension structure, thoroughly investigated its performance. The main idea is to control the load transfer ratio by strategically relocating the attachment point of the vertical structure to the car body. This adjustment is achieved passively through the utilization of the horizontal structure as shown in Figure 1.1.2.3. This research delved into various scenarios, including a semi-active case where the conventional passive spring/damper system was substituted with a semi-active element, specifically the MR damper. Additionally, an active case was explored,

replacing the horizontal structure with a force generator, such as hydraulic actuators. Through numerical simulations and practical testing, including a drop test, the study demonstrated that incorporating a variable stiffness mechanism into the suspension design yielded significant improvements in terms of ride comfort, suspension deflection, and road holding with passive, semi-active and active structure at the same time. This comprehensive exploration underscores the potential of variable stiffness suspension systems in elevating the overall performance and adaptability of vehicle suspensions across diverse operational conditions.

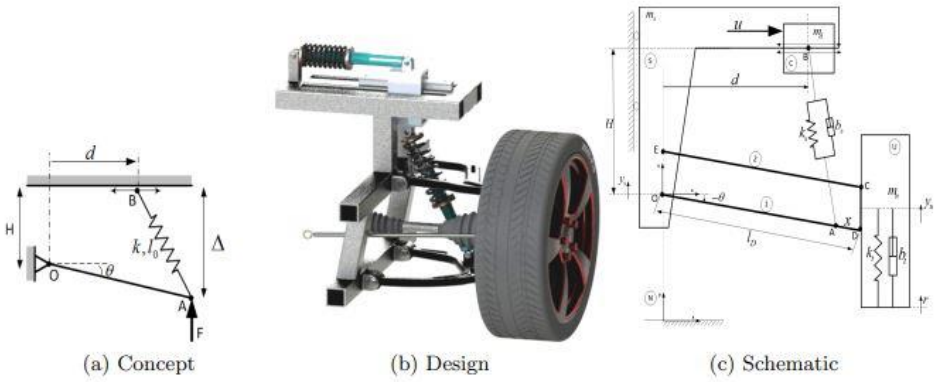

Figure 1.1.2.3 – Variable Stiffness Suspension System [12].

1.2. Principle of the new topology

In recent years, the advantages of leveraging nonlinearity in vibration isolation and energy harvesting domain have garnered growing recognition. The quasi-zero stiffness (QZS) [13] of the nonlinear term provided by the negative stiffness element can achieve vibration isolation under low-frequency environments while improving the efficiency of energy harvesting. [14] The implementation of geometrically nonlinear QZS introduces a distinctive aspect, wherein the force-displacement relationship becomes nonlinear due to factors such as structural deformation, variable disturbances, etc. This nonlinearity due to geometric instability provides a mechanism for generating negative stiffness. Zou et al. [15] proposed a QZS vibration isolator by using a shear structure, as shown in Figure 1.2.1. Then, negative stiffness was provided with by two scissor-like structures and springs. Each scissor-like structure comprised a coil spring and a linear damper. The geometrically nonlinear stiffness was calculated by parametric analysis and the result shows that the system exhibits a broad frequency band for effective vibration isolation. Moreover, the isolator could be tailored to achieve a sizable frequency band, showcasing its adaptability and versatility in meeting specific engineering requirements.

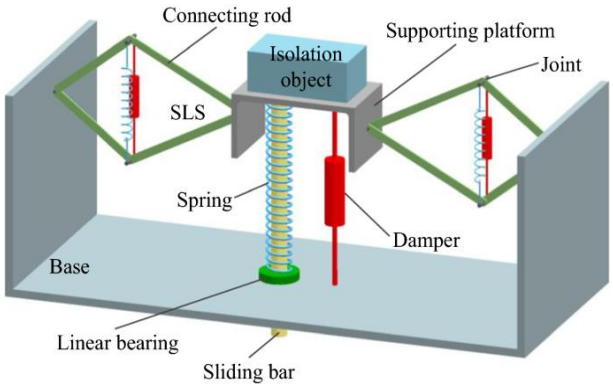

Figure 1.2.1 – Schematic diagram of the proposed QZS vibration system [15].

Li et al. [16] proposed a novel QZS-based bistable electromagnetic energy harvesting device for ocean wave energy. As illustrated in Figure 1.2.2, the structure consisted of two biomimetic X structures. The new biomimetic X-structure has QZS and bistable properties which is achieved by an auxiliary spring, it can experience both quasi-zero stiffness (for ultralow frequency) and negative stiffness regions (for large excitation amplitude). This duality can be regarded as a very beneficial property for ultra-low frequency and large amplitude vibration isolation and wave energy harvesting. The novel X-structured system demonstrates very designable nonlinear bistable and QZS behaviour, contributing significantly to the overall performance of wave energy conversion.

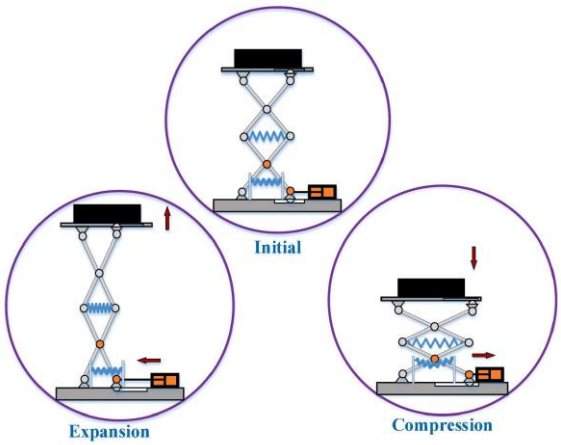

Figure 1.2.2 – Schematic of motion of the proposed X-structure [16].

Besides, in automotive domain, QZS has been investigated to improve the riding comfort of vehicle suspension systems. A. Abolfathi [17] explores the possibility of using a nonlinear QZS spring in a vehicle suspension, it reveals that the QZS suspension provides better isolation of road disturbances. The transient responses of a quarter car model with a QZS suspension to a road bump and random road profile are analysed. The maximum vertical acceleration of the vehicle with the QZS suspension traversing a speed hump is considerably lower than a vehicle with a conventional linear suspension. And due to inverse dependency of the road profile amplitude to spatial frequency, a shorter working range for the specific application of vehicle suspension, the response of the nonlinear system is bounded and negative stiffness characteristic of the nonlinear structure is limited. Additionally, the study conducted by Zeng et al. [18] introduces a suspension vibration control scheme that combines the advantages of QZS, inerter, and nonlinear energy sink (NES). The scheme aims to achieve low transmissibility, low amplitude, and low additional weight in both low-order and high-order resonance. The authors establish a 2-degree-of-freedom quarter-vehicle (2-DOFQV) suspension system integrated with QZS and inerter-NES. They obtain approximate analytic solutions of vibration responses using the harmonic balance method. The results show that the new suspension system greatly improves vehicle riding comfort and handling stability. Overall, the findings underscore the potential for a vehicle equipped with QZS suspension to provide an elevated level of ride quality, thereby enhancing overall comfort and performance across diverse driving conditions.

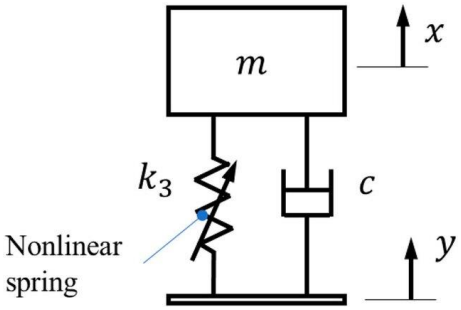

Figure 1.2.3 – The schematic of a single degree of freedom model with a QZS spring [17].

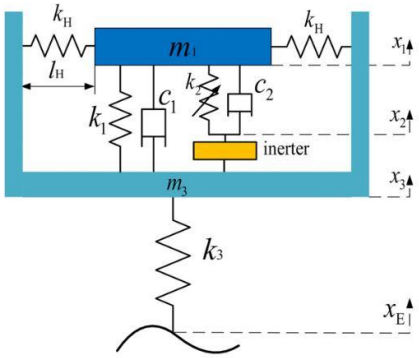

Figure 1.2.4 – 2-DOFQV integrated with the QZS and inerter-NES [18].

Based on that, our work focuses on the development of a novel suspension structure. Instead of the conventional linear springs, an equivalent system with a quadrilateral structure similar to the scissor structure in Figure 1.2.1 and X-structure in Figure 1.2.2 is proposed. This novel structure retains a passive design to minimize costs while simultaneously introducing a broad variable stiffness effect on the vehicle's suspension. As shown in the left of the Figure 1.2.5, the schematic of a typical double wishbone suspension for the front left wheel of a vehicle in a static position is depicted in 2D. The suspension is represented by a planar linkage connected by common joints, with the instantaneous configuration determined by the designed geometry and dominated by the wheel travel at each moment. A spring is traditionally mounted in the lower control arm, linking the suspension to the car body and responsible for the body support and shock absorption. While on the right-hand side of Figure 1.2.5, the original coil spring is replaced by an equivalent quadrilateral structure where two springs work together, aiming to achieve a variable stiffness effect on the vehicle suspension.

As we know the kinematics of the suspension is dictated by its geometry, typically designed in the static state, and confined by some designing targets. In other words, the static layout of the arms and springs directly impact the kinematic behaviour of the suspension and thus the vehicle stiffness at the wheel. Our assumption is that the hard points of the suspension have been predetermined with reasonable hypothetical data, and we aim to analyse the effectiveness of the proposed spring system in terms of our objective, evaluating its impact on the kinematic behaviour of the suspension.

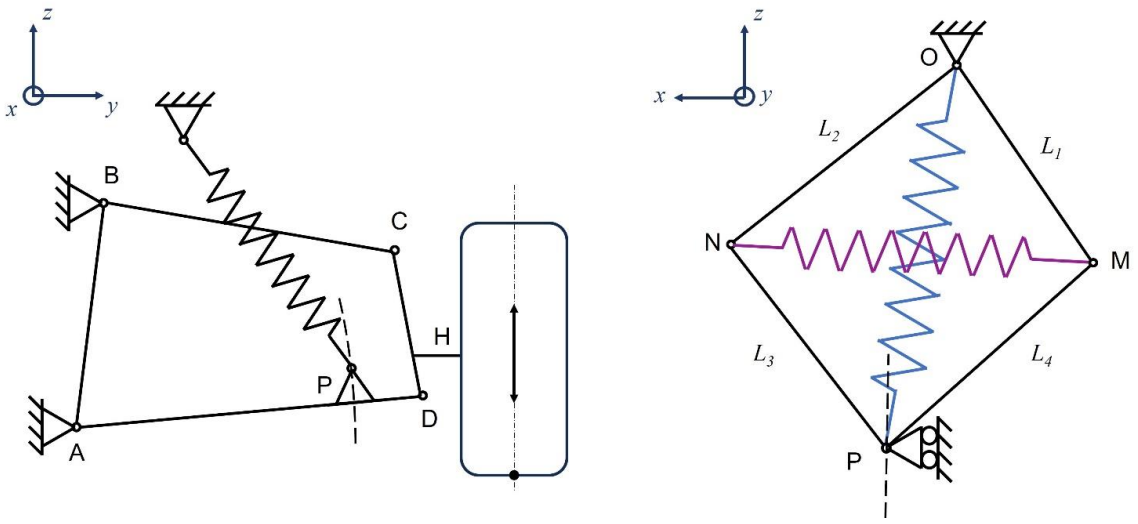

Figure 1.2.5 – The schematics of a general suspension and the equivalent structure.

The underlying principle of the equivalent spring suspension is shown in Figure 1.2.6. In such a quadrilateral-shaped mechanism, the vertical spring of stiffness k_{s1} is mounted directly on the A-arm or knuckle of the suspension, as the normal arrangement. However, the transverse spring, an additional component with stiffness k_{s2}, is mounted horizontally. Between the two springs, four beams are interconnected to transmit the relevant movement and force within the system. When an external force stretches the vertical spring, the transverse spring tends to compress through the linkages, then a compressive force is generated along its centreline and vice versa if the perch P moves upward. It's important to note that the suspension is not in a static position but in a state of dynamic equilibrium when the vehicle is running on the ground. By setting the structural parameters of the suspension and the quadrilateral mechanism at the steady state, the kinematic and kinetic model of the novel structure can be constructed, which allows us to evaluate the nonlinear characteristics resulting from geometric instability and assess the dynamic performance of the system.

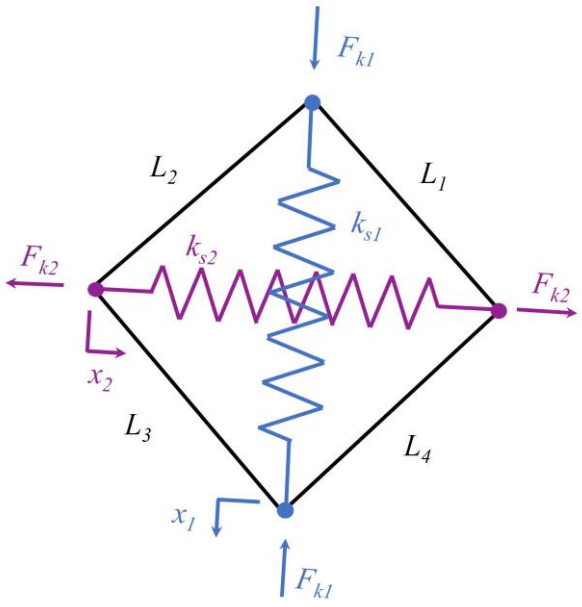

Figure 1.2.6 – Principle of the new topology.

In conclusion, the main idea for this novel method is to introduce a quadrilateral structure instead of the ordinary coil spring in the suspension, by cooperating two springs the equivalent structure will obtain a nonlinear characteristic and benefits the ride comfort and stability of the vehicle. Our research aims to investigate how the static layout of the quadrilateral and the springs directly influences the dynamic performance of the vehicle. Understanding the equivalent effect of the proposed suspension system is at the core of our research objectives.

1.3 Thesis organization

This research focuses on smoothing the ride experience of the road car by developing an equivalent suspension system that shows a wide variable stiffness effect, characterized by a simple structure and broad adjustability. The remainder of this thesis is organized as follows: In chapter 2, some different types of independent suspension are introduced, and the stiffness related design and parameters of a suspension are briefly discussed, laying the foundation for understanding the proposed system. In chapter 3, the simplified model of our proposal based on a double wishbone suspension is shown. In chapter 4, the model will be refined by incorporating the inertia effect into the elements. In chapter 5, the EOM of the system will be evaluated, and the nonlinear characteristic of the system will be discussed in chapter 6. The linearised frequency response and the nonlinear step response of the nonlinear system will be analysed in chapter 7 and chapter 8 correspondingly. Chapter 9 contains the verification of the nonlinear system by introducing a standard double-wishbone suspension. Finally, the conclusions and future work are made in the end.

2 Theory

The problem is initially simplified to a 2D system and solved by analysing some trigonometric relations and static equilibrium functions within the proposed quadrilateral structure. The effectiveness of the novel structure is subsequently assessed through a collaborative approach involving MATLAB and Simulink. While this novel structure is verified based on a double-wishbone suspension in this thesis, it's not exclusively tailored for this suspension. The adaptability of the equivalent spring suspension extends to other suspension configurations, such as Macpherson suspension, provided the geometry of the suspension is known. To better comprehend the effectiveness of the proposed structure, some different types of independent suspension layouts and the critical parameters regarding the vertical stiffness of the suspension will be introduced in this chapter.

2.1 Different types of suspension

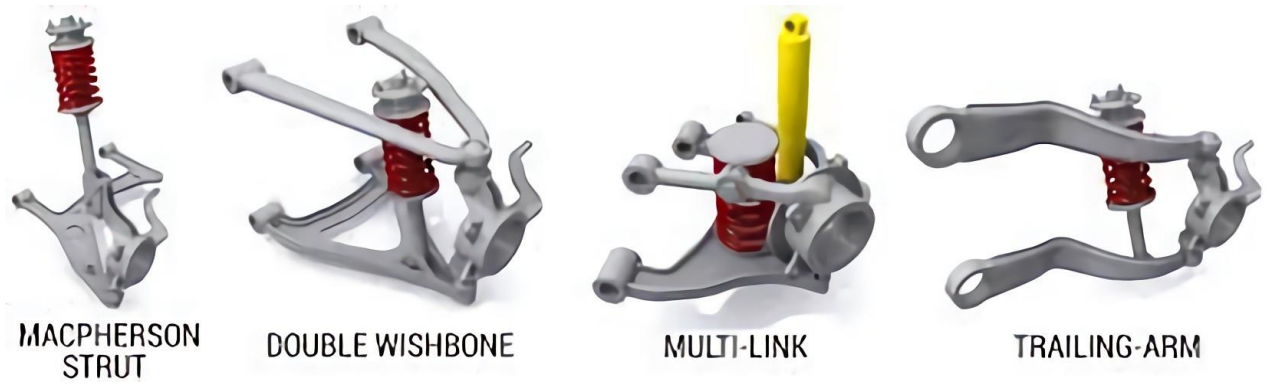

Figure 2.1.1 – Prevalent types of independent suspension [19].

We will start the work with a focus on the double wishbone suspension, but we anticipate that the novel method has broader applicability and can be extended to various types of suspension. In this context, the prevalent independent suspensions in the start of art will be introduced briefly.

- The McPherson suspension: usually employed in family cars, relies on struts without an upper arm. It allows for individual impact absorption for each front wheel, contributing to a smoother ride for passengers. However, the absence of an upper arm can lead to reduced stability during cornering, as the suspension exhibits greater compliance in such scenarios.
- The double wishbone suspension: generally adopted on higher vehicle segments and sports cars, known for providing superior handling and a comfortable ride when compared to other suspension systems.
- The multilink suspension: offers the greatest customizability and allow the greatest control over the ride of the vehicle but consequently increase the complexity and cost of the suspension.
- The trailing arm suspension: commonly used on the rear axle of vehicles, featuring a rigid attachment to the wheels. This design may result in inevitably more shock transfer to the car body, making it a more cost-effective solution often employed in budget-friendly vehicles for effective cost control.

2.2 Suspension kinematics and characteristic parameters

Suspension kinematics and the critical suspension geometric parameters can be designed by defining the suspension hardpoints. Once the suspension hardpoints are determined, the kinematic of the suspension is also aligned. For the purpose of this report, which focuses on evaluating the effectiveness of a new suspension typology, specific vehicle types will not be discussed. Instead, an analytical analysis will be presented. Nonetheless, some valuable information about defining and optimizing the suspension kinematics can be learned from Carlo's project [20] and the method for creating the MATLAB multibody suspension model to visualize the kinematics of the suspension can be learned from Giulio Allora's work [21].
Upon setting the suspension kinematics, it becomes feasible to determine the characteristic parameter values as a function of wheel travel. Some essential parameters, e.g., camber angle, toe angle, caster angle, roll angle, etc., should be validated following the design target and some general regularizations, the hardpoints and length of the control arm can be modified to meet the specific requirement [20].

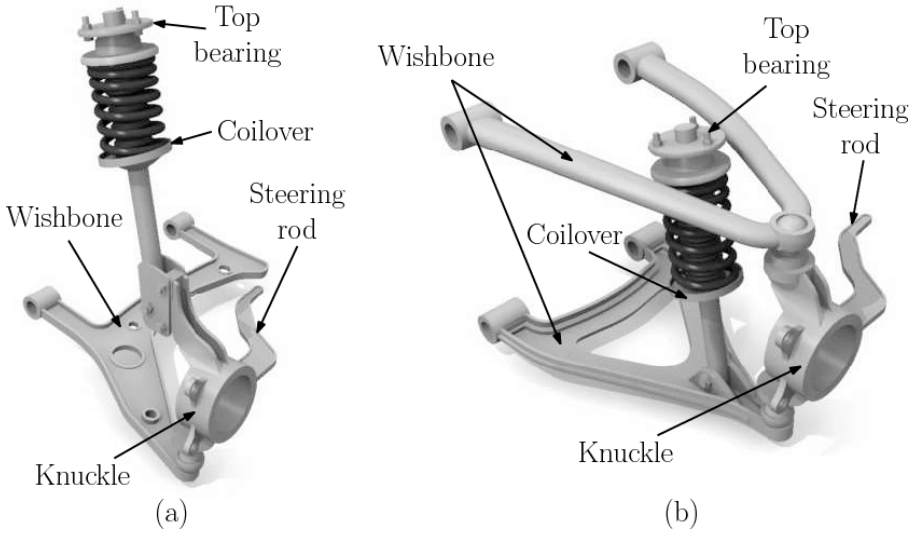

Figure 2.2.1 – Components of the Macpherson (a) and double wishbone suspension (b) [22].

2.3 Wheel rate

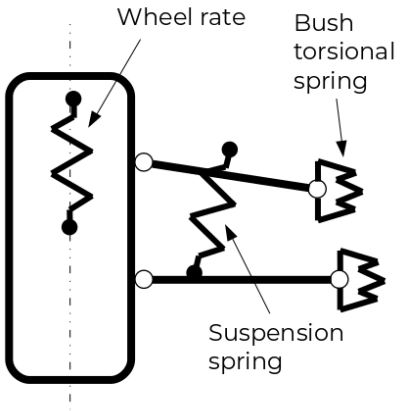

Figure 2.3.1 – Wheel rate schematic [23].

The wheel rate, in essence, is basically the spring rate measured at the wheel instead of where the spring attaches to the linkage. This parameter signifies the vertical stiffness of the vehicle at each wheel and stands as a critical hyperparameter that we aim to optimize. We could tell that this rate ultimately determines the performance of the car through its influence on wheel loads. In the context of the novel suspension typology, it implies a strategic approach to reduce the vertical stiffness at the wheel. This reduction aims to smooth the ride comfort and keep the tire in contact with the ground when the wheel encounters external excitations. The figure above shows how the wheel rate is determined. It is basically estimated by the spring rate of the spring multiplied by the square of the motion ratio. The motion ratio, a concept to be further elaborated in Section 2.4, is a crucial factor in this calculation.

2.4 Motion ratio

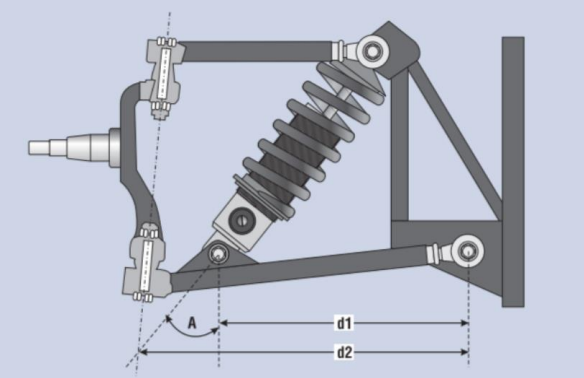

Figure 2.4.1 – Motion ratio of suspension [24].

The motion ratio is defined as the ratio between the relative movement of the lower spring perch to the upper spring perch and the movement of the wheel itself. This motion ratio can be estimated by knowing the distance of the wheel to the pivot point (d_2) of the suspension arm and the distance to the spring from the pivot point (d_1) shown in the upper figure.
The motion ratio can be used for the calculation of the wheel force and wheel stiffness evaluation. In cases where the spring inclination angle is substantial, a spring angle correction factor cannot be ignored and needs to consider the correction value cos(A). The equations linking the motion ratio (MR) and wheel rate (WR) are given below.

$$MR = \frac{d_1}{d_2} \tag{2.4.1}$$

$$F_{wheel} = MR \cdot F_{spring} \cos(\mathrm{A}) \tag{2.4.2}$$

$$WR = k_{spring} \cdot MR^2 \cos(\mathrm{A}) \tag{2.4.3}$$

Where the k_{spring} is the stiffness of the coil spring in the suspension. We need to mention that the equation for calculating wheel rate from spring rate in its simplest form just gives an estimation. During the dynamic motion phases, the spring may compress a very different amount than what the wheel actually moves, leading to variations in the motion ratio throughout the wheel travel. There are additional corrections for spring spatial angle, wheel offset from the ball joint, camber change, etc. But the value we approximate at the steady state can provide a useful initial value at the very beginning for the forward analysis.

2.5 Vehicle natural frequency

The suspension's natural frequency is calculated by eq. (2.5.1), in which k is the wheel rate and m is the sprung mass.

$$f = \frac{1}{2\pi}\sqrt{\frac{k}{m}} \tag{2.5.1}$$

The natural frequency of the vehicle depends on its type and intended mission. To ensure the proper setting of the suspension, it is possible to take into account the general recommendations reported by Milliken [25] and Woods [26] here below summarized in Table 2.5.1.

Table 2.5.1 – General suspension natural frequency settings [21].

Vehicle type	Ride frequency	Unit of measure
Road cars	0.8-1.5	Hz
Non aero formula cars	around 2	Hz
Aero cars	5-7	Hz

Indeed, the design of a suspension system is inherently unique for each type of car and varies based on the diverse challenges the vehicle is expected to confront. In the case of race cars, it demands the highest performance regardless any care about durability and comfort hence the suspension can be designed exceptionally stiff to resist the downforce. On the contrary, the design of a suspension system for road cars necessitates a different set of priorities. Here, the focus is not only on optimizing handling but also on mitigating wear on the wheels and addressing the sensitive vibration frequencies experienced by the human body [27], so the reduction of the vibrations and the optimization of the comfort for the passengers while offering good handling are on demand.

3. Model and simplify the structure

The aforementioned principle discussed in chapter 1 provides an initial insight into the novel equivalent spring suspension, and now it's time to simplify the complex structure to a 2D problem in order to assess the effectiveness of this method. The proposed double wishbone suspension is depicted in 2D within the y-z plane, specifically focusing on the front left wheel. In this representation, the suspension system is conceptualized as a planar linkage interconnected by common joints. The instantaneous configuration of the system requires just one input parameter, which, in this case, is the wheel travel or the inclination of the LCA. The kinematics of this simplified system can be verified using the Grubler's formula [28].

$$F = 3(N-1) - 2C_1 - C_2 \tag{3.1}$$

Where F is the total degrees of freedom in the mechanism, N is the number of elements, C_1 is the number of lower pairs (each removes 2 d.o.f) and C_2 is the number of high pairs (each removes 1 d.o.f). In our problem there are four hinges at A, B, C, and D, each removes two degrees of freedom. Thus, the d.o.f of the system can be verified by eq. (3.2), and we assume the motion of suspension is governed by the wheel displacement h in the reset of the article.

$$F = 3\times(4-1) - 4\times 2 - 0 = 1 \tag{3.2}$$

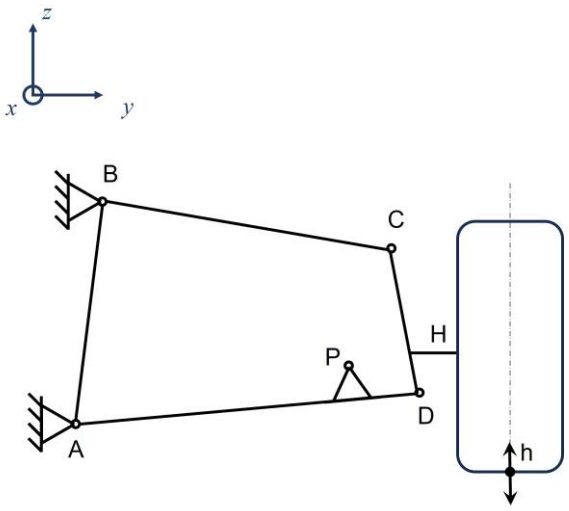

Figure 3.1 – Double wishbone suspension geometry at 2D level (FL).

With the suspension parameters assumed to be established, our focus now shifts to analysing the effectiveness of the equivalent spring mechanism, specifically in terms of its variable stiffness effect. The initial step in this study involves constructing an equivalent model to analyse the FBD, kinematics, and kinetics of the system. The model of the novel spring system can be analysed independently of the entire suspension, and for better uniformity in the analysis process, we will discuss it in another global *x-y* coordinate instead of the vehicle coordinate system. The analysis of the FBD and the motion of the system will be given step by step, laying the foundation for the subsequent development of kinetic and kinematic models in this chapter. It's essential to note that this analysis is theoretical, considering hypothetical data and not accounting for spatial limits in the structural arrangement.

3.1 Free body diagrams

The starting point of drawing the FBDs is to simplify the problem by making some reasonable approximations. The analysis commences from a steady state, acknowledging that the entire suspension system operates in a quasi-static state during the vertical motion of the wheel. So the two springs can be considered as two rods in the model at each equilibrium position correspondingly, and the spring force can be calculated by the displacement of itself as shown in eq. (3.1.13) and eq. (3.1.14), given the spring stiffness. The trajectory of the spring lower perch P is considered here as a vertical line for simplicity, which is determined by the geometry of the suspension and should follow a curve in reality. Without factoring the inertia effect at this stage, the model can be considered as a structure comprising sting six rods interconnected by hinges. There is a hinge support at point O and a horizontal roller support at point P, as shown in Figure 3.1.1.

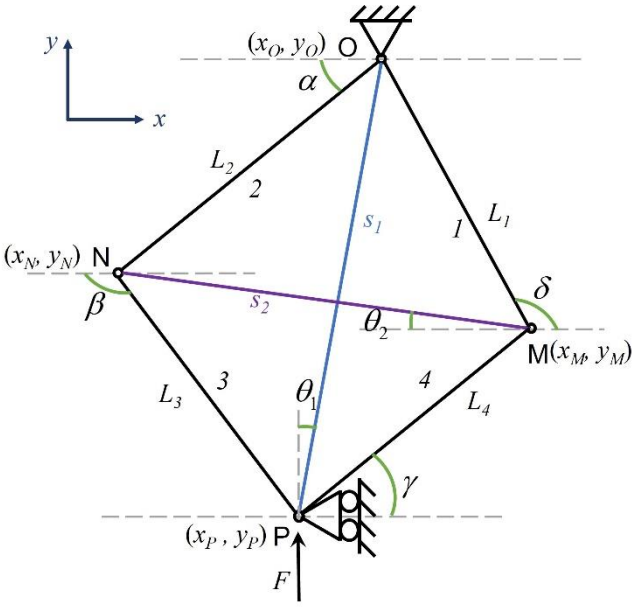

Figure 3.1.1 – The simplified physical model.

In the model, the point O serves as a pickup point, and its coordinate (x_O, y_O) should be determined at first, and the x position of point P (x_P) is set because it's determined by the spring perch position in the knuckle. Furthermore, in our specific problem, the four lengths of the edges (L_1, L_2, L_3, L_4) and angles (α, δ) are considered as design parameters, to be decided in the static steady. Once these parameters are defined, the motion of the system is determined, as well as the coordinate of points N, M, angles β, γ, θ_1, θ_2, and two diagonal lengths $\overline{OP}$, $\overline{MN}$ can be extrapolated using the equations listed below.

By simply considering the trigonometric relations in the frame, the ordinate of point P (y_P) and the coordinates of point N (x_N, y_N) and point M (x_M, y_M) can be evaluated.

$$y_P = y_O - \left(L_2 \sin(\alpha) + L_3 \sin(\beta)\right) \tag{3.1.1}$$

$$x_N = x_O - L_2 \cos(\alpha) \tag{3.1.2}$$

$$y_N = y_O - L_2 \sin(\alpha) \tag{3.1.3}$$

$$x_M = x_O + L_1 \cos(\pi - \delta) \tag{3.1.4}$$

$$y_M = y_O - L_1 \sin(\pi - \delta) \tag{3.1.5}$$

Using the derived coordinates, the length of two diagonals can be obtained.

$$\overline{OP} = \sqrt{\left(x_O - x_P\right)^2 + \left(y_O - y_P\right)^2} \tag{3.1.6}$$

$$\overline{MN} = \sqrt{\left(x_M - x_N\right)^2 + \left(y_M - y_N\right)^2} \tag{3.1.7}$$

Extrapolate the values of angles β, γ, θ_1, and θ_2 using the trigonometric relations in the quadrilateral.

$$\beta = \pi - \cos^{-1}\left(\frac{\left|x_N - x_P\right|}{L_3}\right) \tag{3.1.8}$$

$$\gamma = \tan^{-1}\left(\frac{y_M - y_P}{x_M - x_P}\right) \tag{3.1.9}$$

$$\theta_1 = \tan^{-1}\left(\frac{x_O - x_P}{y_O - y_P}\right) \tag{3.1.10}$$

$$\theta_2 = \tan^{-1}\left(\frac{y_N - y_M}{\left|x_N - x_M\right|}\right) \tag{3.1.11}$$

$$L_4 = \frac{y_M - y_P}{\sin(\gamma)} \tag{3.1.12}$$

The next step involves decomposing the entire model down to the element level and analysing the free body diagram of each element.

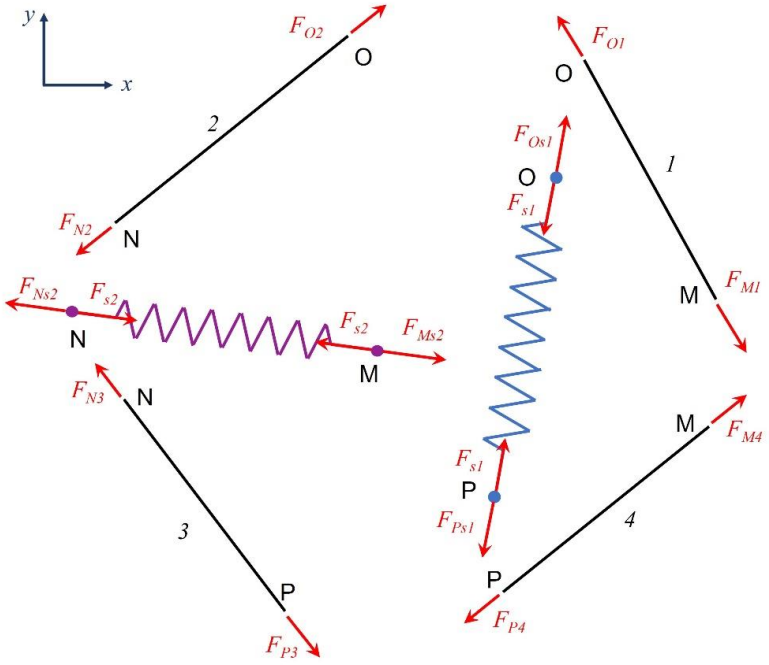

Figure 3.1.2 – Free body diagram of each element.

The two spring forces can be initially calculated using Hooke's law.

$$F_{s1} = k_{s1}\Delta l = k_{s1}(\overline{OP} - l_{o1}) \tag{3.1.13}$$

$$F_{s2} = k_{s2}\Delta l = k_{s2}(\overline{MN} - l_{o2}) \tag{3.1.14}$$

Where k_{s1} and k_{s2} are the spring stiffnesses, l_{o1} and l_{o2} are the lengths of the two springs at rest, correspondingly. It is assumed that the spring force is positive when the spring is stretched and negative when compressed.

Each element is interconnected by a pair of hinges to the structure, and balanced by two forces of equal magnitude but the opposite directions. Consequently, all elements are considered as rod elements here, and the loads are axial forces applied to the nodes. The loads in elements 1, 2, 3, and 4 are identical in magnitude accordingly, for consistency, it is assumed that the loads are positive when the rods are stretched and negative when they are compressed. The force relationship in each rod can be expressed as follow:

$$F_1 = F_{O1} = F_{M1} \tag{3.1.15}$$

$$F_2 = F_{O2} = F_{N2} \tag{3.1.16}$$

$$F_3 = F_{N3} = F_{P3} \tag{3.1.17}$$

$$F_4 = F_{P4} = F_{M4} \tag{3.1.18}$$

Employing the relationships outlined above, we can proceed to determine the loading conditions at each node in the entire structure. The free body diagrams of the overall system at nodes O, P, N, M, are shown in Figure 3.1.3. The forces denoted with the prime characters signify the reaction force from the rods to the corresponding nodes, they have the same magnitude as the action force but act in opposite direction within each element.

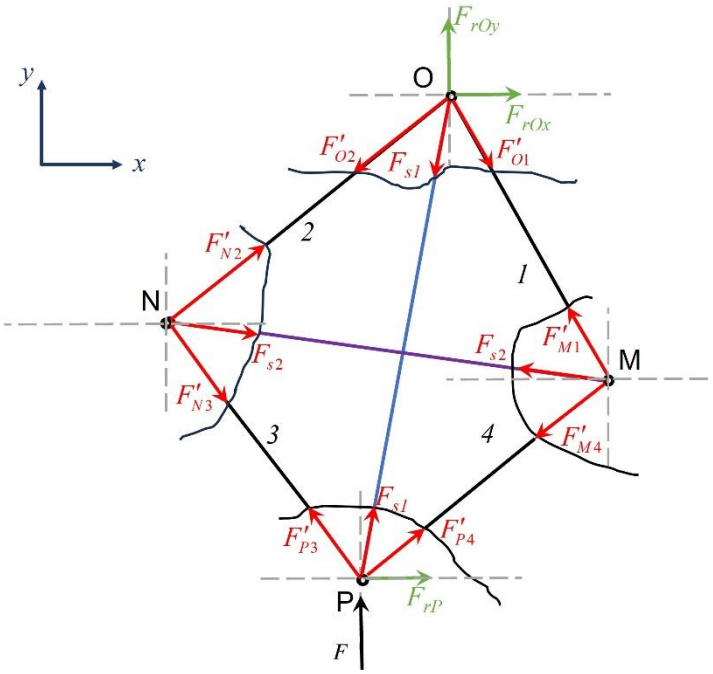

Figure 3.1.3 – Free body diagram of the whole system.

Extract the concurrent forces at each node, and solve the equilibrium equation along the x and y directions correspondingly.

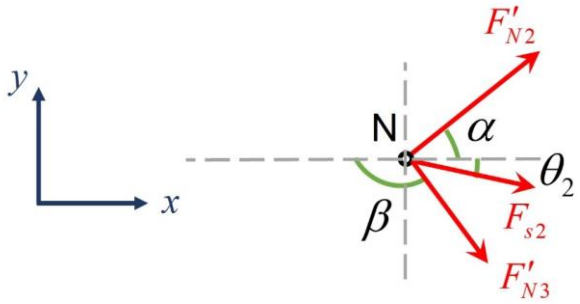

Figure 3.1.4 – Free body diagram at node N.

Solve the equilibrium equations around point N and extrapolate the axial forces in element 2 and element 3.

$$F'_{N3}\cos(\pi-\beta)+F'_{N2}\cos(\alpha)=-F_{s2}\cos(\theta_2) \tag{3.1.19}$$

$$F'_{N3}\sin(\pi-\beta)-F'_{N2}\sin(\alpha)=-F_{s2}\sin(\theta_2) \tag{3.1.20}$$

$$F_2=F'_{N2}=\frac{-F_{s2}\cos(\theta_2)-F'_{N3}\cos(\pi-\beta)}{\cos(\alpha)} \tag{3.1.21}$$

$$F_3=F'_{N3}=F_{s2}\tau_3=F_{s2}\frac{-\sin(\theta_2)-\cos(\theta_2)\tan(\alpha)}{\sin(\pi-\beta)+\cos(\pi-\beta)\tan(\alpha)} \tag{3.1.22}$$

To streamline the upcoming expressions and enhance clarity, an intermediate coefficient τ_3 will be introduced here. A similar role is played by the coefficient τ_4 in the subsequent formulas.

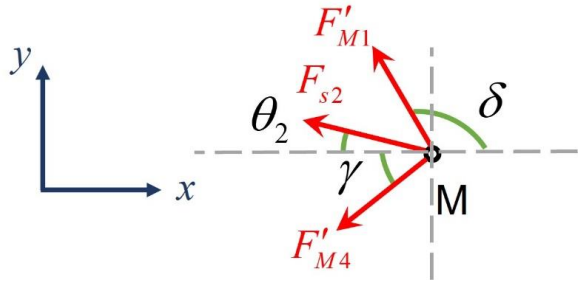

Figure 3.1.5 – Free body diagram at node M.

Solve equilibrium function around point *M* and extrapolate the axial forces in element 1 and element 4.

$$F'_{M1}\cos(\pi-\delta)+F'_{M4}\cos(\gamma)=-F_{s2}\cos(\theta_2) \tag{3.1.23}$$

$$F'_{M1}\sin(\pi-\delta)-F'_{M4}\sin(\gamma)=-F_{s2}\sin(\theta_2) \tag{3.1.24}$$

$$F_1=F'_{M1}=\frac{-F_{s2}\sin(\theta_2)+F'_{M4}\sin(\gamma)}{\sin(\pi-\delta)} \tag{3.1.25}$$

$$F_4=F'_{M4}=F_{s2}\tau_4=F_{s2}\frac{\sin(\theta_2)-\cos(\theta_2)\tan(\pi-\delta)}{\sin(\gamma)+\cos(\gamma)\tan(\pi-\delta)} \tag{3.1.26}$$

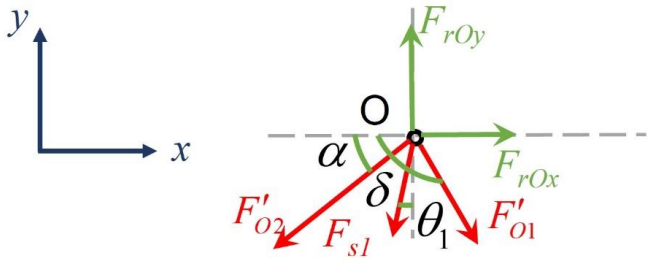

Figure 3.1.6 – Free body diagram at node O.

Solve equilibrium function around point *O* and extrapolate the reaction forces in hinge O.

$$F_{rOx} = F_{s1}\sin(\theta_1) - F'_{O1}\cos(\pi - \delta) + F'_{O2}\cos(\alpha) \tag{3.1.27}$$

$$F_{rOy} = F_{s1}\cos(\theta_1) + F'_{O1}\sin(\pi - \delta) + F'_{O2}\sin(\alpha) \tag{3.1.28}$$

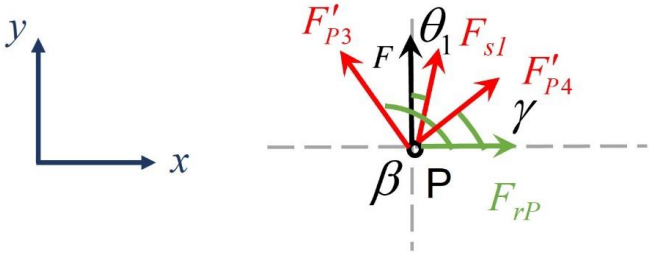

Figure 3.1.7 – Free body diagram at node P.

Considering the state of equilibrium along the *x* direction, the reaction force of the roller support F_{rP} can be evaluated.

$$F_{rP} = -F'_{P4}\cos(\gamma) + F'_{P3}\cos(\pi - \beta) - F_{s1}\sin(\theta_1) \tag{3.1.29}$$

To derive the expression for the load *F*, the equilibrium equation around point P along the *y* direction is analysed. The resultant force along the *y* direction should by be zero as shown in eq. (3.1.30).

$$F_{s1}\cos(\theta_1) + F + F'_{P3}\sin(\pi - \beta) + F'_{P4}\sin(\gamma) = 0 \tag{3.1.30}$$

Rewriting the eq. (3.1.30) and substituting the force F'_{P3} and F'_{P4} with force F_3 and F_4, we now have a general expression for load *F*.

$$F = -F_{s1}\cos(\theta_1) - F_{s2}\left(\tau_3\sin(\pi - \beta) + \tau_4\sin(\gamma)\right) \tag{3.1.31}$$

By harmonising the equation above, it becomes evident that the load *F* can be represented in terms of parameters that can be individuated or extrapolated, as we demonstrated earlier. It implies that the expression is applicable at any position of the wheel, provided the geometry of the suspension in the static state.

$$F = -F_{s1}\cos(\theta_1) - F_{s2}\left(\frac{-\sin(\theta_2)-\cos(\theta_2)\tan(\alpha)}{\sin(\pi-\beta)+\cos(\pi-\beta)\tan(\alpha)}\sin(\pi-\beta)+\frac{\sin(\theta_2)-\cos(\theta_2)\tan(\pi-\delta)}{\sin(\gamma)+\cos(\gamma)\tan(\pi-\delta)}\sin(\gamma)\right) \tag{3.1.32}$$

With obtained such a function for load F, now it's possible to establish the relationship between the wheel travel and the load F when the wheel is in motion, and consequently the value of load F when the structure is in a dynamic state. The kinematic model of the system will be evaluated in the next section.

3.2. Kinematic model analysis

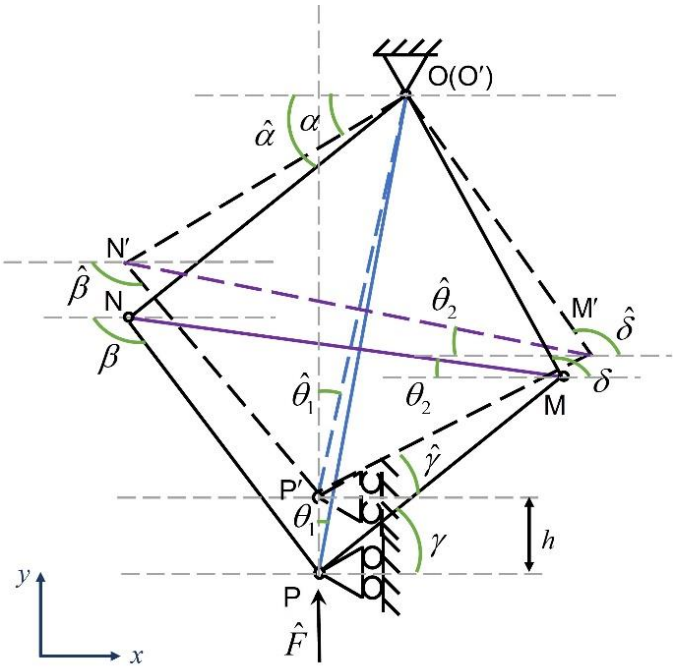

Figure 3.2.1 – The kinematics f the structure.

In our proposal, the equivalent system aims to achieve a wide variable stiffness effect on the wheel to enhance the driving experience, improve the ride comfort, and augment the mechanical grip capability. This implies a focus on improving dynamic performance rather than designing a vehicle that remains in a static state. In this section, we try to explore the kinematic characteristics of the system and give a first evaluation of its the effectiveness.

Supposing that the wheel moves a little due to the road excitation, and correspondingly the perch P moves a displacement h. We hypothesise a quasi-static process in the structure, in any equilibrium position, the new load $\hat{F}$ can be evaluated by eq. (3.1.31) by substituting the parameters with the updated values. The expression of $\hat{F}$ can now be written as eq. (3.2.1).

$$\hat{F} = -\hat{F}_{s1}\cos(\hat{\theta}_1) + \hat{F}_{s2}\left(\hat{\tau}_3\sin(\pi-\hat{\beta}) + \hat{\tau}_4\sin(\hat{\gamma})\right) \tag{3.2.1}$$

In which the two coefficients and two spring forces are given by eq. (3.2.2) to eq. (3.2.5).

$$\hat{\tau}_3 = \frac{\sin(\hat{\theta}_2) + \cos(\hat{\theta}_2)\tan(\hat{\alpha})}{\sin(\pi - \hat{\beta}) + \cos(\pi - \hat{\beta})\tan(\hat{\alpha})} \tag{3.2.2}$$

$$\hat{\tau}_4 = \frac{-\sin(\hat{\theta}_2) + \cos(\hat{\theta}_2)\tan(\pi - \hat{\delta})}{\sin(\hat{\gamma}) + \cos(\hat{\gamma})\tan(\pi - \hat{\delta})} \tag{3.2.3}$$

$$\hat{F}_{s1} = k_{s1}\Delta\hat{l}_1 = k_{s1}(\overline{O'P'} - l_{o1}) \tag{3.2.4}$$

$$\hat{F}_{s2} = k_{s2}\Delta\hat{l}_2' = k_{s2}(\overline{M'N'} - l_{o2}) \tag{3.2.5}$$

The coordinates (x_O', y_O'), (x_P', y_P'), (x_M', y_M'), (x_N', y_N') of the four nodes in the updated quadrilateral $O'N'PM'$ structure can also be extrapolated as shown in Figure 3.2.1.

$$x_O' = x_O \tag{3.2.6}$$

$$y_O' = y_O \tag{3.2.7}$$

$$x_P' = x_P \tag{3.2.8}$$

$$y_P' = y_P + h \tag{3.2.9}$$

$$x_N' = x_O' - L_2\cos(\hat{\alpha}) \tag{3.2.10}$$

$$y_N' = y_O' - L_2\sin(\hat{\alpha}) \tag{3.2.11}$$

$$x_M' = x_O' + L_1\cos(\pi - \hat{\delta}) \tag{3.2.12}$$

$$y_M' = y_O' - L_1\sin(\pi - \hat{\delta}) \tag{3.2.13}$$

Considering the angle $\hat{\alpha}$ and angle $\hat{\delta}$, they can be extrapolated with other angles by making some simple considerations on the quadrilateral $O'N'PM'$.

$$\hat{\alpha} = \frac{\pi}{2} - \hat{\theta}_1 - \angle P'ON' \tag{3.2.14}$$

$$\hat{\delta} = \frac{\pi}{2} - \hat{\theta}_1 + \angle P'OM' \tag{3.2.15}$$

In which the two angles $\angle P'ON'$ and $\angle P'OM'$ can be represented using the cosine theorem.

$$\tan(\hat{\theta}_1) = \frac{x_O' - x_P'}{y_O' - y_P'} \tag{3.2.16}$$

$$\hat{\theta}_1 = \tan^{-1}\left(\frac{x_O' - x_P'}{y_O' - y_P'}\right) \tag{3.2.17}$$

$$\overline{O'P'} = \left|\frac{x_O' - x_P'}{\sin(\hat{\theta})}\right| \tag{3.2.18}$$

$$\angle P'ON' = \cos^{-1}\left(\frac{L_2^2 + OP'^2 - L_3^2}{2L_2OP'}\right) \tag{3.2.19}$$

$$\angle P'OM' = \cos^{-1}\left(\frac{L_1^2 + OP'^2 - L_4^2}{2L_1OP'}\right) \tag{3.2.20}$$

Having determined the angle $\hat{\alpha}$ and angle $\hat{\delta}$, it becomes possible to represent all the other angles using the four coordinates of the four nodes.

$$\hat{\beta} = \pi - \tan^{-1}\left(\frac{y'_N - y'_P}{|x'_N - x'_P|}\right) \tag{3.2.21}$$

$$\hat{\gamma} = \tan^{-1}\left(\frac{y'_M - y'_P}{x'_M - x'_P}\right) \tag{3.2.22}$$

$$\hat{\theta}_2 = \tan^{-1}\left(\frac{y'_N - y'_M}{|x'_N - x'_M|}\right) \tag{3.2.23}$$

Now, we can evaluate each parameter as a function of the wheel displacement *h*. By combining the equations and substituting the parameters into eq. (3.2.1), we can express the dynamic load as a function of the wheel travel *h*. While this function might be sophisticated and cumbersome to solve manually, we can construct the model using MATLAB, as demonstrated in Section 3.3.

3.3. Model the kinematic model

Building upon the kinematic analysis in section 3.2, we have established that the structural parameters of the equivalent system can be evaluated by extrapolating the trigonometric relations in the quadrilateral. This means that the coordinates of each node can be obtained with the extrapolated angles and lengths, and consequently the trajectory of the nodes can be modelled as the wheel moves up and down, assuming a particular wheel travel. With that, the variations in all angles, diagonal lengths, loads in all rods and the reaction forces in the two supports can be discussed here.

The general functions representing the kinematics and kinetics of the system were already evaluated in section 3.1 and section 3.2. In this section, we will focus on a very specific condition. In this specific quadrilateral, there is a diamond shape, the vertical spring is oriented in the vertical direction, the transverse spring aligns horizontally, and the four edges are all equal, as shown in Figure 3.3.1.

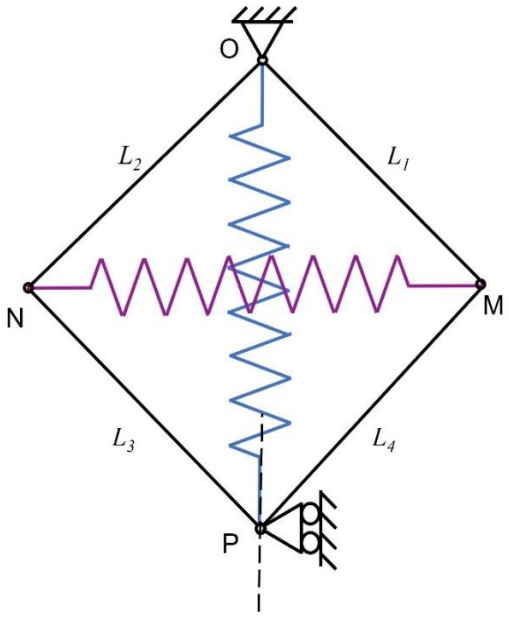

Figure 3.3.1 – Specific quadrilateral with a symmetric setting.

The parameters of the proposed structure are configured in the static state as shown in Table 3.3.1. The data presented here is not the real data from a specific car, instead, it is hypothetical data designed to quantitatively assess the performance of the system.

Table 3.3.1 – Structural parameters setting in the static state.

Parameter	**Value**
(x_O, y_O) [m]	(0, 0)
(x_P, y_P) [m]	(0, -0.7071)
(x_M, y_M) [m]	(0.3536, -0.3536)
(x_N, y_N) [m]	(-0.3536, -0.3536)
L_1 [m]	0.5
L_2 [m]	0.5
L_3 [m]	0.5
L_4 [m]	0.5
α [°]	45
β [°]	135
γ [°]	45
δ [°]	45
$\overline{OP}$ [m]	0.7071
$\overline{MN}$ [m]	0.7071
k_{s1} [N/m]	36000
k_{s2} [N/m]	36000
l_{o1} [m]	$\overline{OP}$
l_{o2} [m]	$\overline{MN}$
Wheel travel [m]	[-0.1, 0.1]

By developing MATLAB code to construct the kinematic and kinetic models of the system, we can generate some useful plots to enhance our understanding of the structure's performance. The results are depicted in Figure 3.3.2 to Figure 3.3.6 below, assuming the wheel displacement is within the range of [-100mm 100mm].

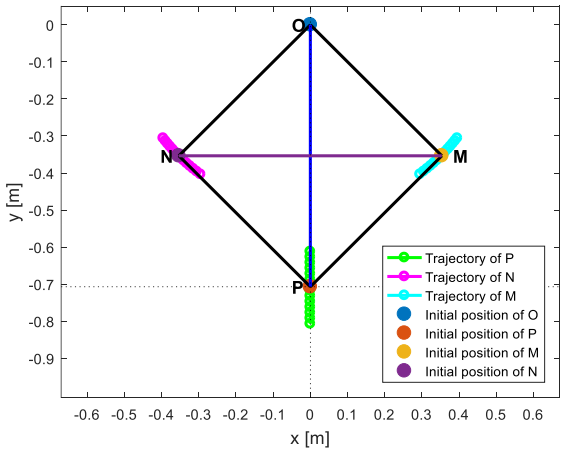

Figure 3.3.2 – Trajectory of the structure vs. wheel travel.

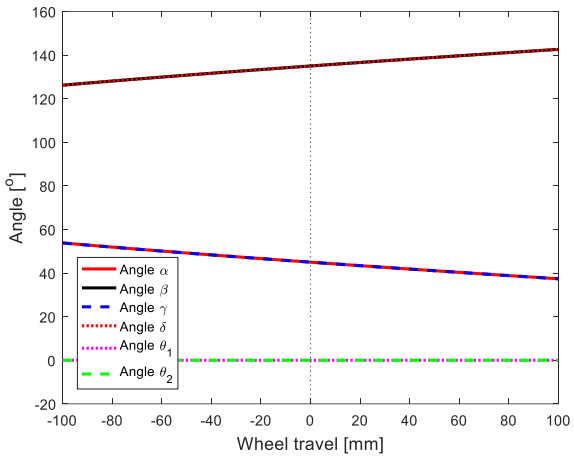

Figure 3.3.3 – Angle vs. wheel travel.

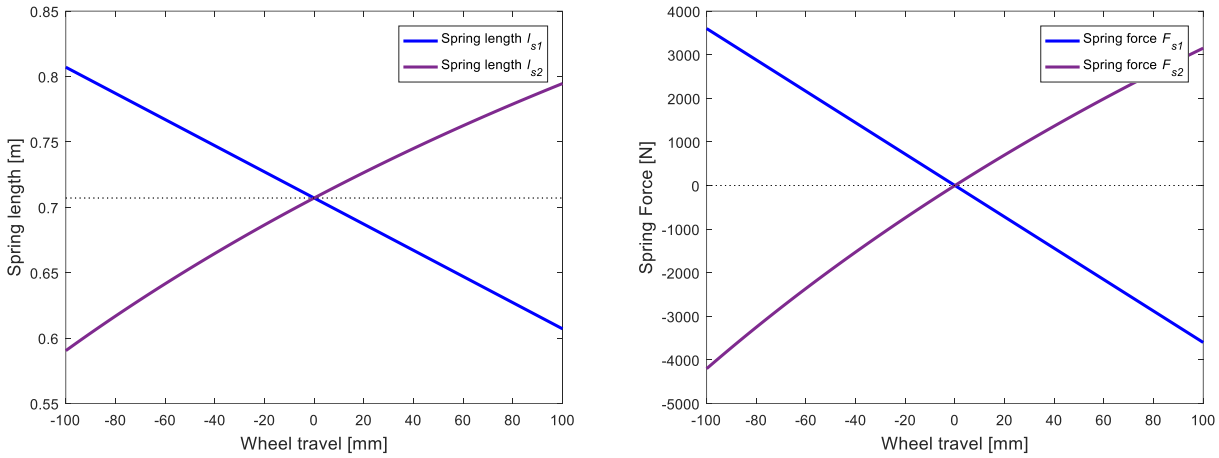

Figure 3.3.4 – Spring length vs. wheel travel (left) and Spring force vs. wheel travel (right).

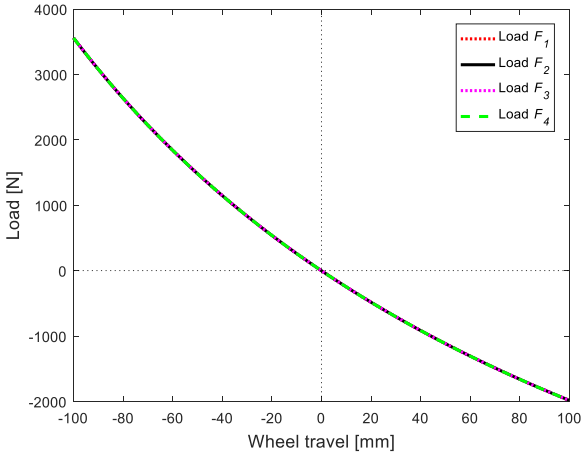

Figure 3.3.5 – Internal loads vs. wheel travel.

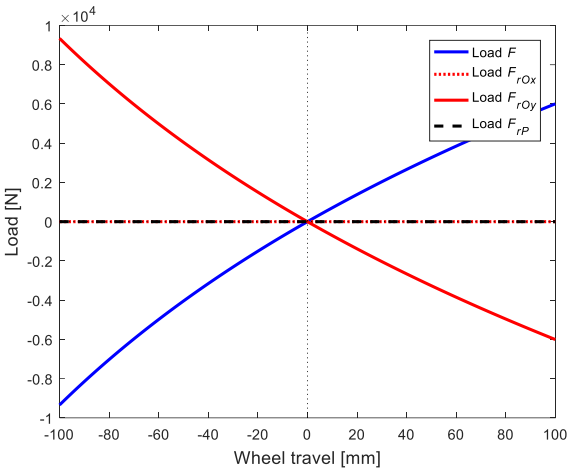

Figure 3.3.6 – Loads at constrains O and P vs. wheel travel.

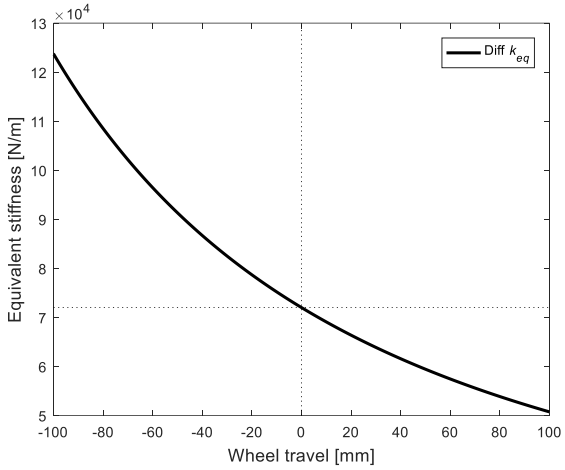

Figure 3.3.7 – Equivalent stiffness vs. wheel travel.

From the presented diagrams, it's evident that in the symmetrical structure, the internal loads in each element are identical. As the wheel approaches the upper bump stop position, the load F successively increases, and when the wheel travels down, the load F decreases, which mirrors the trend of a normal coil spring.

However, our primary interest lies in the equivalent stiffness of the novel system, shown as a black curve in the Figure 3.3.7, which provides us the confidence regarding our main objective. The test was performed with the data as shown in Table 2.3.1, and the result shows a unique equivalent stiffness compared to a traditional suspension. In the jounce phase, the equivalent stiffness of the system bottoms out, indicating a softening effect on the suspension. While in the rebound phase, the system's stiffness behaves a hardening effect. Nevertheless, it's important to note that the nonlinear stiffness characteristic is incurred by the horizontal spring k_{s2} as the spring force of spring k_{s1} changes in a completely linear way, whereas the spring k_{s2} behaves nonlinearly in Figure 3.3.4. Where the fundamental reason for this lies in the inherent geometric instability of the quadrilateral, which make the horizontal diagonal length change nonlinearly when the point P moves up and down. This indicates that the main direction of our analysis should focus on the horizontal spring when such a symmetric structure is involved.

We appreciate the softening effect certainly, it's essential to acknowledge that the stiffening effect in the extension phase may compensates for the handling performance of the vehicle which is weakened by the softening effect in the compression phase when the car accelerates or brakes. As

the vertical stiffness at the wheel is influenced by both the motion ratio and the equivalent stiffness of the suspension, the delightful characteristic of the simple structure gives us an idea to achieve the desired vehicle dynamic performance by cooperating the design of the suspension geometry and the proposed novel spring system.

4. Refine the model

Although we have a model that illustrates the kinematics of our system, it's still insufficient to accurately represent the structure in real condition. We currently assume that each link is a rod element withstanding axial loads. To complete and refine the model, now we will consider the inertia and the weight of the links, as the unsprung mass in the vehicle directly influences the dynamic performance of the suspension, especially if the lightweight material is not considered. The kinematics of the simplified model and refined model should be consistent since the geometric parameters are not modified, but it's necessary to reevaluate the formulas representing the kinetic forces, and the process will be more complicated at this stage for the internal force of each link can no longer be assumed as purely axial.

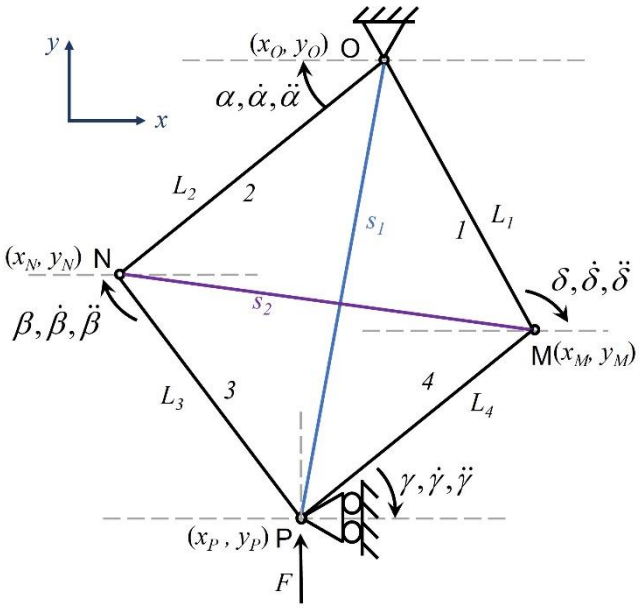

Figure 4.1 – The dynamic schematic of the system.

To start the work, we need to account for the mass of each link and the moment of inertia of each link, as they contribute to the inertial forces and inertial moments. The mass of each component can be calculated from the density of the material and the volume of the element. Here we assume that the masses are lumped at their respective centre of gravity, and all the beams are modelled as cylindrical with rounded ends and a diameter of D_i.

$$m_i = \rho V_i \tag{4.1}$$

$$V_i = \frac{\pi L_i D_i^2}{4} \tag{4.2}$$

Where $i \in [1,2,3,4]$, ρ equals to 7850 kg/m^3 when the steel material is choosen, and the volume V_i is determined by the section area and the length of the beams correspondingly.
The moment of inertia can be evaluated using the eq. (4.3) and the beams will rotate around their centroid.

$$I_i = \frac{1}{12} m_i L_i^2 \tag{4.3}$$

Where $i \in [1,2,3,4]$.

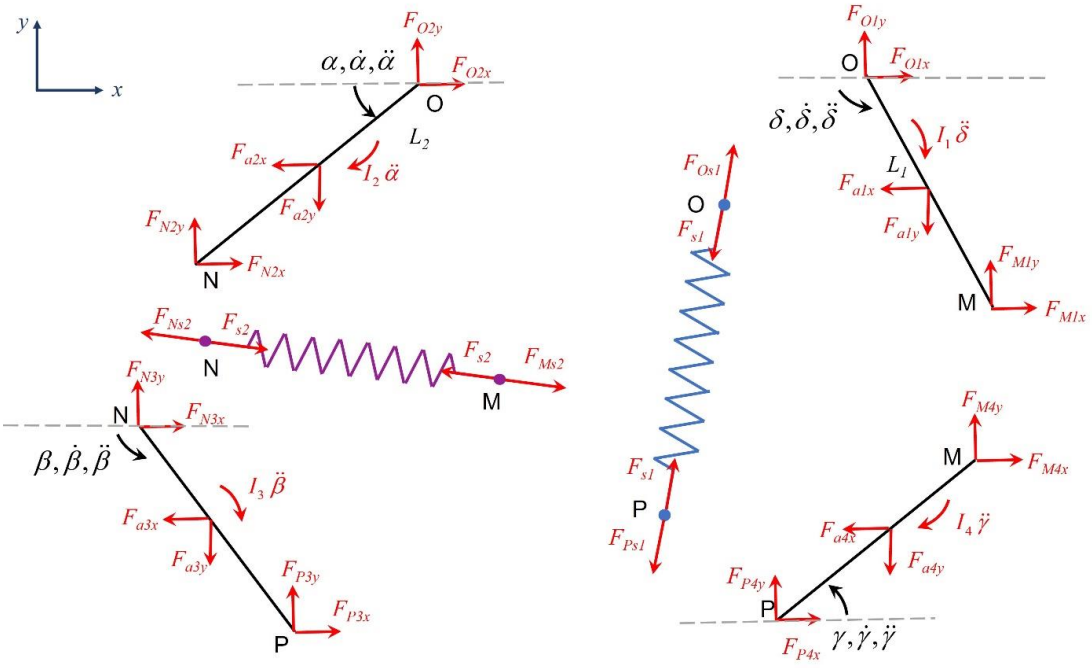

Figure 4.2 – Free body diagrams of each beam considering the effect of inertia.

The next step is similar to the process undertaken in section 3.1, involving the decomposition of the structure and analysis of the FBD of each link. We assume that the mass within each link is concentrated at its centroid, with the angular velocity and the moment considered positive when rotating counterclockwise. Forces are considered positive along the positive direction of the *x* and *y* axes.

The motion trajectory of each centroid can be represented by the vector with respect to an inertial reference point. For instance, the motion vector of the centroid in beam *ON* is depicted in Figure 4.3. The the vector can be expressed using the coordinates of its two ends, where the coordinates of two ends have already been extrapolated in the kinematic model in section 3.2. By taking the first and second derivatives of the vector, the velocity and acceleration vector can be evaluated.

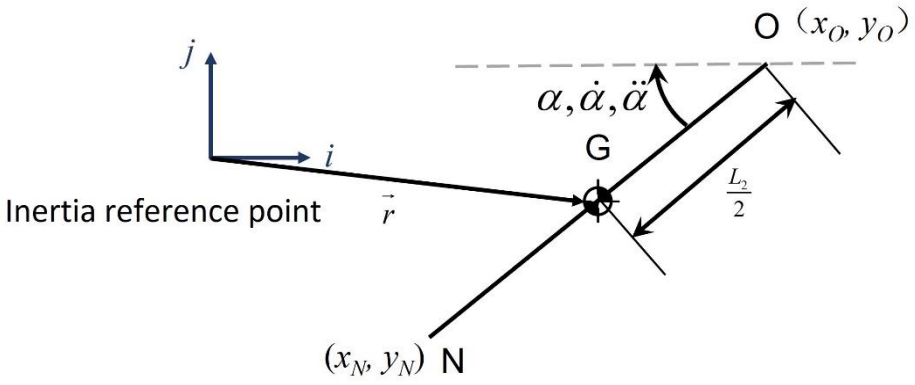

Figure 4.3 – The motion vector in an inertial reference frame.

$$\vec{r} = \frac{x_O + x_N}{2}\vec{i} + \frac{y_O + y_N}{2}\vec{j} \tag{4.4}$$

$$\dot{\vec{r}} = \frac{\dot{x}_O + \dot{x}_N}{2}\vec{i} + \frac{\dot{y}_O + \dot{y}_N}{2}\vec{j} \tag{4.5}$$

$$\ddot{\vec{r}} = \frac{\ddot{x}_O + \ddot{x}_N}{2}\vec{i} + \frac{\ddot{y}_O + \ddot{y}_N}{2}\vec{j} \tag{4.6}$$

$$\ddot{x}_G = \frac{\ddot{x}_O + \ddot{x}_N}{2} \tag{4.7}$$

$$\ddot{y}_G = \frac{\ddot{y}_O + \ddot{y}_N}{2} \tag{4.8}$$

The equations above reveal that the abscissa of the centroid can be expressed as half of the sum of the two ends', and the ordinate can be expressed as half of the summation of the two ends' ordinates. Consequently, the velocity and acceleration of the centroid can be obtained by calculating the first and second derivatives of its coordinate. Given that all elements work in the same reference frame, the conclusions can be applied to other links. The acceleration of each centroid and the inertial forces in each beam can be then evaluated, resulting in following the equations:

$$\begin{array}{llll}
x_{1G} = \frac{x_O + x_M}{2} & x_{2G} = \frac{x_O + x_N}{2} & x_{3G} = \frac{x_P + x_N}{2} & x_{4G} = \frac{x_P + x_M}{2} \\
y_{1G} = \frac{y_O + y_M}{2} & y_{2G} = \frac{y_O + y_N}{2} & y_{3G} = \frac{y_P + y_N}{2} & y_{4G} = \frac{y_P + y_M}{2} \\
a_{1x} = \ddot{x}_{1G} & a_{2x} = \ddot{x}_{2G} & a_{3x} = \ddot{x}_{3G} & a_{4x} = \ddot{x}_{4G} \\
a_{1y} = \ddot{y}_{1G} & a_{2y} = \ddot{y}_{2G} & a_{3y} = \ddot{y}_{3G} & a_{4y} = \ddot{y}_{4G} \\
F_{a1x} = m_1 a_{1x} & F_{a2x} = m_2 a_{2x} & F_{a3x} = m_3 a_{3x} & F_{a4x} = m_4 a_{4x} \\
F_{a1y} = m_1 a_{1y} & F_{a2y} = m_2 a_{2y} & F_{a3y} = m_3 a_{3y} & F_{a4y} = m_4 a_{4y}
\end{array} \tag{4.9}$$

Now, we can list three equilibrium functions in each element, two along the axes and one for moment. As the gravity of each element does not bring any nonlinear effect to the system, the gravitational force of the system is ignored in the analysis. By rewriting the equilibrium formulas, all the other forces in every element can be represented by a force in the *x* direction, as shown below.

Representing all the other forces by F_{M1x} in element 1:

$$F_{O1x} = -F_{M1x} + F_{a1x} \tag{4.10}$$

$$F_{O1y} = -F_{M1y} + F_{a1y} \tag{4.11}$$

$$F_{M1y} = \frac{\left(-F_{M1x} L_1 \sin(\pi - \delta) + F_{a1x} \frac{L_1 \sin(\pi - \delta)}{2} + F_{a1y} \frac{L_1 \cos(\pi - \delta)}{2} + I_1 \ddot{\delta}\right)}{L_1 \cos(\pi - \delta)} \tag{4.12}$$

In element 2, all the other forces can be represented by F_{N2x}:

$$F_{O2x} = -F_{N2x} + F_{a2x} \tag{4.13}$$

$$F_{O2y} = -F_{N2y} + F_{a2y} \tag{4.14}$$

$$F_{N2y} = \frac{\left(F_{N2x} L_2 \sin(\alpha) - F_{a2x} \frac{L_2 \sin(\alpha)}{2} + F_{a2y} \frac{L_2 \cos(\alpha)}{2} - I_2 \ddot{\alpha} \right)}{L_2 \cos(\alpha)} \tag{4.15}$$

Representation of all the other forces using F_{N3x} in element 3:

$$F_{P3x} = -F_{N3x} + F_{a3x} \tag{4.16}$$

$$F_{P3y} = -F_{N3y} + F_{a3y} \tag{4.17}$$

$$F_{N3y} = \frac{\left(-F_{N3x} L_3 \sin(\pi - \beta) + F_{a3x} \frac{L_3 \sin(\pi - \beta)}{2} + F_{a3y} \frac{L_3 \cos(\pi - \beta)}{2} - I_3 \ddot{\beta} \right)}{L_3 \cos(\pi - \beta)} \tag{4.18}$$

All the other forces are represented by F_{M4x} in element 4:

$$F_{P4x} = -F_{M4x} + F_{a4x} \tag{4.19}$$

$$F_{P4y} = -F_{M4y} + F_{a4y} \tag{4.20}$$

$$F_{M4y} = \frac{\left(F_{M4x} L_4 \sin(\gamma) - F_{a4x} \frac{L_4 \sin(\gamma)}{2} + F_{a4y} \frac{L_4 \cos(\gamma)}{2} + I_4 \ddot{\gamma} \right)}{L_4 \cos(\gamma)} \tag{4.21}$$

Now we move on to analyse the concurrent forces in the nodes, the reaction forces from the links to the nodes represented by the force with the prime symbol as in Figure 4.4. We aim to link the internal forces in each element by listing the equilibrium functions along the x direction and y direction in each node. By joining the two y direction forces together, we can get the expression of the force along x direction as a function of the spring force as shown below.

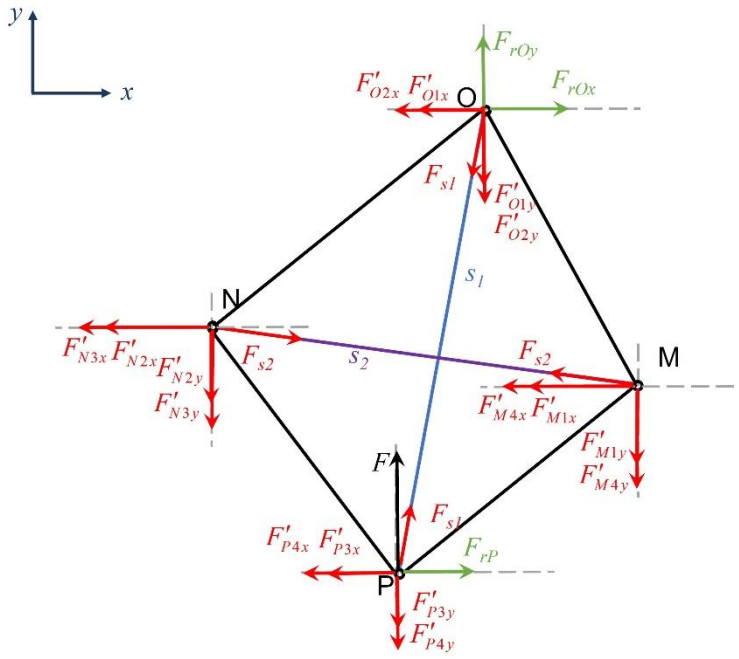

Figure 4.4 – Free body diagram of concurrent forces at each node.

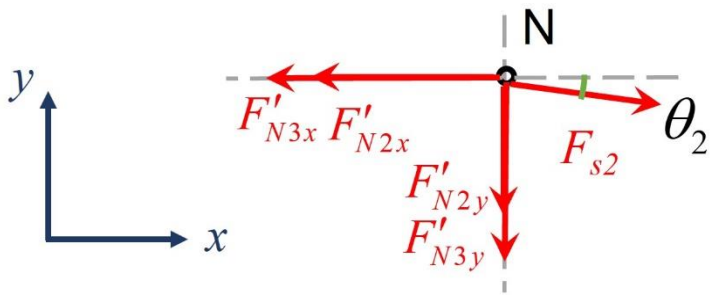

Figure 4.5 – Free body diagram of concurrent forces at node N.

Equilibrium function in both directions at node N.

$$F'_{N2x} + F'_{N3x} - F_{s2}\cos(\theta_2) = 0 \tag{4.22}$$

$$F'_{N2y} + F'_{N3y} + F_{s2}\sin(\theta_2) = 0 \tag{4.23}$$

In which the reaction forces in each element are in the opposite direction but have same magnitude with respect to the action forces.

$$F'_{N2y} = F_{N2y} = \frac{\left(F_{N2x}L_2\sin(\alpha) - F_{a2x}\frac{L_2\sin(\alpha)}{2} + F_{a2y}\frac{L_2\cos(\alpha)}{2} - I_2\ddot{\alpha}\right)}{L_2\cos(\alpha)} \tag{4.24}$$

$$F'_{N3y} = F_{N3y} = \frac{\left(-F_{N3x}L_3\sin(\pi-\beta) + F_{a3x}\frac{L_3\sin(\pi-\beta)}{2} + F_{a3y}\frac{L_3\cos(\pi-\beta)}{2} - I_3\ddot{\beta}\right)}{L_3\cos(\pi-\beta)} \tag{4.25}$$

To clarify the formulas and avoid tedious equations later on, we will introduce two forces $F_{N2\_}$ and $F_{N3\_}$, which are unrelated to the forces under investigation but just associated with known parameters. This strategic introduction aids in simplifying the forthcoming expressions and streamlining the notation.

$$F_{N2\_} = \frac{\left(-F_{a2x}\frac{L_2\sin(\alpha)}{2} + F_{a2y}\frac{L_2\cos(\alpha)}{2} - I_2\ddot{\alpha}\right)}{L_2\cos(\alpha)} \tag{4.26}$$

$$F_{N3\_} = \frac{F_{a3x}\frac{L_3\sin(\pi-\beta)}{2} + F_{a3y}\frac{L_3\cos(\pi-\beta)}{2} - I_3\ddot{\beta}}{L_3\cos(\pi-\beta)} \tag{4.27}$$

With the introduction of the two forces, we can now represent the target forces more succinctly.

$$F'_{N2y} = F_{N2y} = F_{N2x}\tan(\alpha) + F_{N2\_} \tag{4.28}$$

$$F'_{N3y} = F_{N3y} = -F_{N3x}\tan(\pi-\beta) + F_{N3\_} \tag{4.29}$$

By substituting the forces F'_{N2y} and F'_{N3y} into eq. (4.23), we can get the expression of force F'_{N2x}.

$$F'_{N2x} = F_{N2x} = \frac{F_{N3x}\tan(\pi-\beta) - F_{s2}\sin(\theta_2) - F_{N2\_} - F_{N3\_}}{\tan(\alpha)} \tag{4.30}$$

Joining the eq. (4.22) and eq. (4.30) together, the force F_{N3x} can be finally written as a function of the spring force and the trigonometric identities relate to each angle as shown in eq. (4.31).

$$F'_{N3x} = F_{N3x} = \frac{F_{s2}(\cos(\theta_2)\tan(\alpha) + \sin(\theta_2)) + F_{N2\_} + F_{N3\_}}{\tan(\alpha) + \tan(\pi-\beta)} \tag{4.31}$$

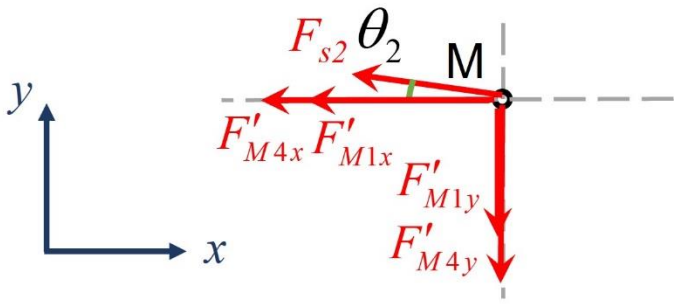

Figure 4.6 – Free body diagram of concurrent forces at node M.

By mirroring the aforementioned manipulations, the force F_{M4x} can also be represented by the spring force F_{s2} and the trigonometric values when analysing the concurrent forces at node M. In addition, we will introduce another two more forces $F_{M1\_\_}$ and $F_{M4\_}$ here.

$$F_{M1x} + F_{M4x} + F_{s2}\cos(\theta_2) = 0 \tag{4.32}$$

$$F_{M1y} + F_{M4y} - F_{s2}\sin(\theta_2) = 0 \tag{4.33}$$

$$F'_{M1y} = F_{M1y} = \frac{\left(-F_{M1x}L_1\sin(\pi-\delta) + F_{a1x}\frac{L_1\sin(\pi-\delta)}{2} + F_{a1y}\frac{L_1\cos(\pi-\delta)}{2} + I_1\ddot{\delta}\right)}{L_1\cos(\pi-\delta)} \tag{4.34}$$

$$F'_{M4y} = F_{M4y} = \frac{\left(F_{M4x}L_4\sin(\gamma) - F_{a4x}\frac{L_4\sin(\gamma)}{2} + F_{a4y}\frac{L_4\cos(\gamma)}{2} + I_4\ddot{\gamma}\right)}{L_4\cos(\gamma)} \tag{4.35}$$

$$F_{M1\_} = \frac{F_{a1x}\frac{L_1\sin(\pi-\delta)}{2} + F_{a1y}\frac{L_1\cos(\pi-\delta)}{2} + I_1\ddot{\delta}}{L_1\cos(\pi-\delta)} \tag{4.36}$$

$$F_{M4\_} = \frac{-F_{a4x}\frac{L_4\sin(\gamma)}{2} + F_{a4y}\frac{L_4\cos(\gamma)}{2} + I_4\ddot{\gamma}}{L_4\cos(\gamma)} \tag{4.37}$$

$$F'_{M1y} = F_{M1y} = -F_{M1x}\tan(\pi-\delta) + F_{M1\_} \tag{4.38}$$

$$F'_{M4y} = F_{M4y} = F_{M4x}\tan(\gamma) + F_{M4\_} \tag{4.39}$$

$$F'_{M1x} = F_{M1x} = \frac{F_{M4x}\tan(\gamma) - Fs2\sin(\theta_2) + F_{M1\_} + F_{M4\_}}{\tan(\pi-\delta)} \tag{4.40}$$

$$F'_{M4x} = F_{M4x} = \frac{-F_{s2}(\cos(\theta_2)\tan(\pi-\delta) - \sin(\theta_2)) - F_{M1\_} - F_{M4\_}}{\tan(\pi-\delta) + \tan(\gamma)} \tag{4.41}$$

At this point, all the forces in each component can be written as a function of the spring force F_{s2} and the corresponding trigonometric identities, where the spring force can be evaluated using Hooke's law and the angles can be calculated based on the analysis in section 3.2. This means we can obtain the internal forces of each link now. In the next step, we will consider the reaction forces at the supports in order to evaluate the load F, additionally, the strength of the material can be validated in the further work if it's a concern.

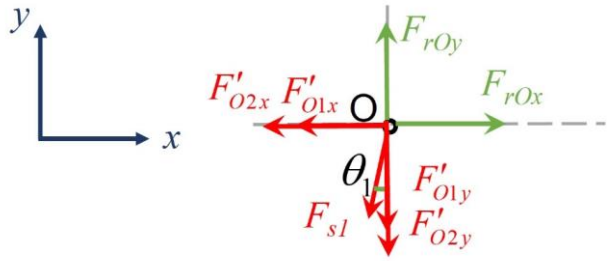

Figure 4.7 – Free body diagram of concurrent forces at node O.

By considering the equilibrium function in both directions at node O, the constraining forces can be calculated correspondingly. The reaction force F_{rO} of the hinge O can be obtained by synthesising the component forces in eq. (4.44).

$$F_{rOx} = F'_{O1x} + F'_{O2x} + F_{s1}\sin(\theta_1) \tag{4.42}$$

$$F_{rOy} = F'_{O1y} + F'_{O2y} + F_{s1}\cos(\theta_1) \tag{4.43}$$

$$F_{rO} = \sqrt{\left(F_{rOx}{}^2 + F_{rOy}{}^2\right)} \tag{4.44}$$

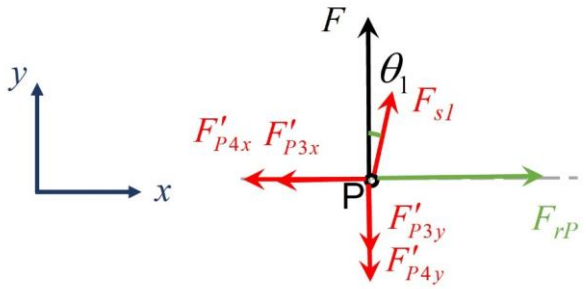

Figure 4.8 – Free body diagram of concurrent forces at node P.

Considering the equilibrium function in both directions at node P, the load F and the constraint force F_{rP} of the roller support P can be evaluated similarly.

$$F_{rP} = F'_{P4x} + F'_{P3x} - F_{s1}\sin(\theta_1) \tag{4.45}$$

$$F = F'_{P4y} + F'_{P3y} - F_{s1}\cos(\theta_1) \tag{4.46}$$

4.1 Kinematic model considering the inertia effect

After evaluating of the forces in the whole system, we have obtained all the formulas of the internal forces in each beam and the constraining forces in each support as a function of the spring forces

and the trigonometric identities derived in section 3.2. With that, we can conduct a simulation in MATLAB using the data provided in Table 4.1.1. The unevenness of the road profile is modelled as a sinusoidal shape with an amplitude of 100mm, and a 5 rad/s frequency as depicted in Figure 4.1.1. Nevertheless, as the vertical spring k_{s1} in the symmetrical structure shows a linear behaviour in section 3.3, and our focus is on the nonlinear characteristics of the system, we will concentrate on the behaviour of the horizontal spring k_{s2}, and the effect of the vertical spring is eliminated by setting its stiffness equals to 0. The dynamical behaviour of the system is illustrated below.

Table 4.1.1 – Structural parameters in the static state.

Parameter	**Value**
(x_O, y_O) [m]	(0, 0)
(x_P, y_P) [m]	(0, -0.7071)
(x_M, y_M) [m]	(0.3536, -0.3536)
(x_N, y_N) [m]	(-0.3536, -0.3536)
L_1 [m]	0.5
L_2 [m]	0.5
L_3 [m]	0.5
L_4 [m]	0.5
α [°]	45
β [°]	135
γ [°]	45
δ [°]	45
$\overline{OP}$ [m]	0.7071
$\overline{MN}$ [m]	0.7071
k_{s1} [N/m]	0
k_{s2} [N/m]	36000
l_{o1} [m]	$\overline{OP}$
l_{o2} [m]	$\overline{MN}$
Wheel travel [m]	[-0.1, 0.1]
D [m]	0.04
ρ [kg/m^3]	7850

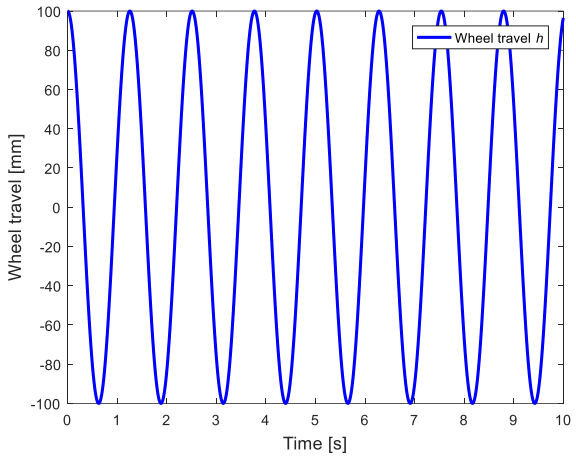

Figure 4.1.1 – Proposed road profile.

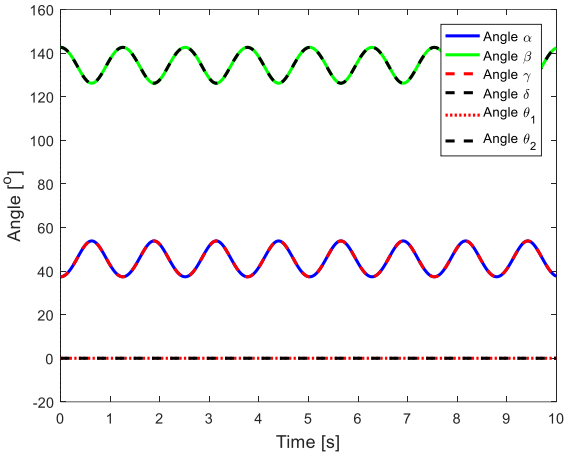

Figure 4.1.2 – The variety of each angle.

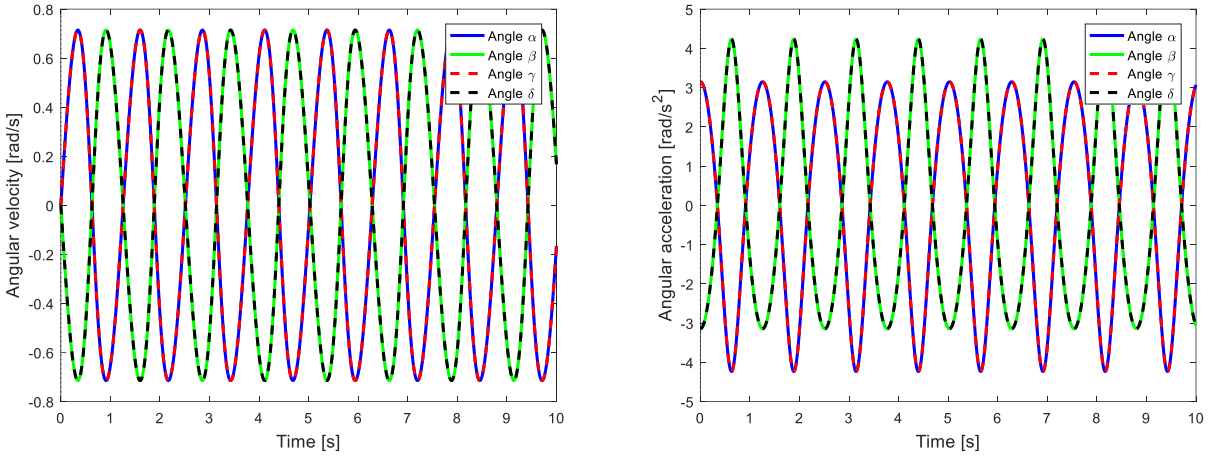

Figure 4.1.3 – Angular velocity and angular acceleration.

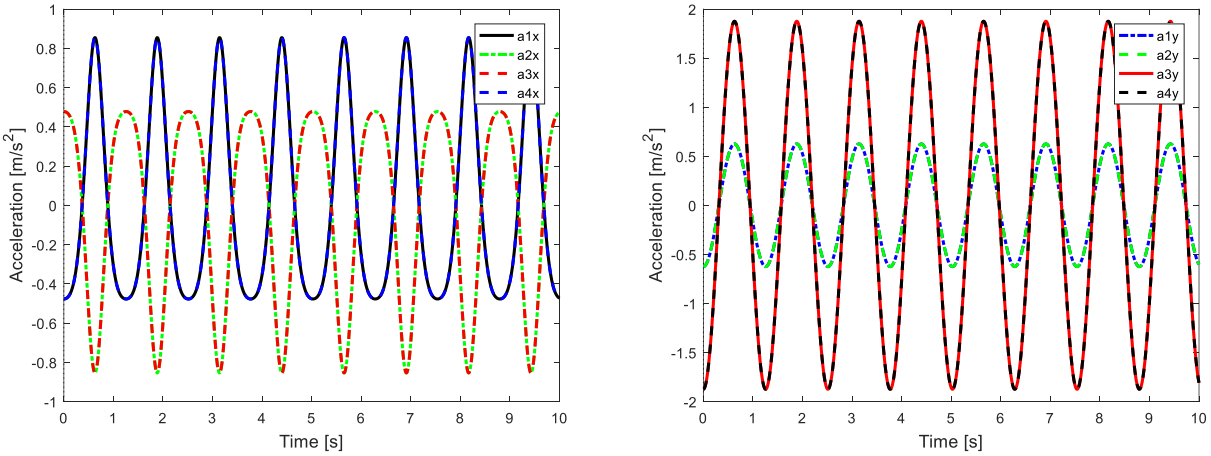

Figure 4.1.4 – Translational acceleration along *x* and *y* directions at the centroid of each beam.

In Figure 4.1.3, the angular dynamics of the system shows that the four angles exhibit relative changes corresponding to the regular harmonic wheel displacement. In the jounce phase, the angle changes more moderately than in the rebound phase, and consequently the angular acceleration has

a smaller magnitude in the jounce phase and a larger magnitude in the rebound phase. This characteristic conforms the geometric instability and the softening and hardening effects in the two corresponding phases. In Figure 4.1.4, similarly, the translational dynamics of the system also show the geometric instability. The translational motion can be decoupled in x and y directions separately, while in the y direction the motion corresponds to the wheel displacement and it behaves linearly, in the x direction the acceleration is flattened as the structure approaches the upper boundary, the shape is sharpened and the peak is increased when it moves downwards, indicating the hardening effect in the rebound phase.

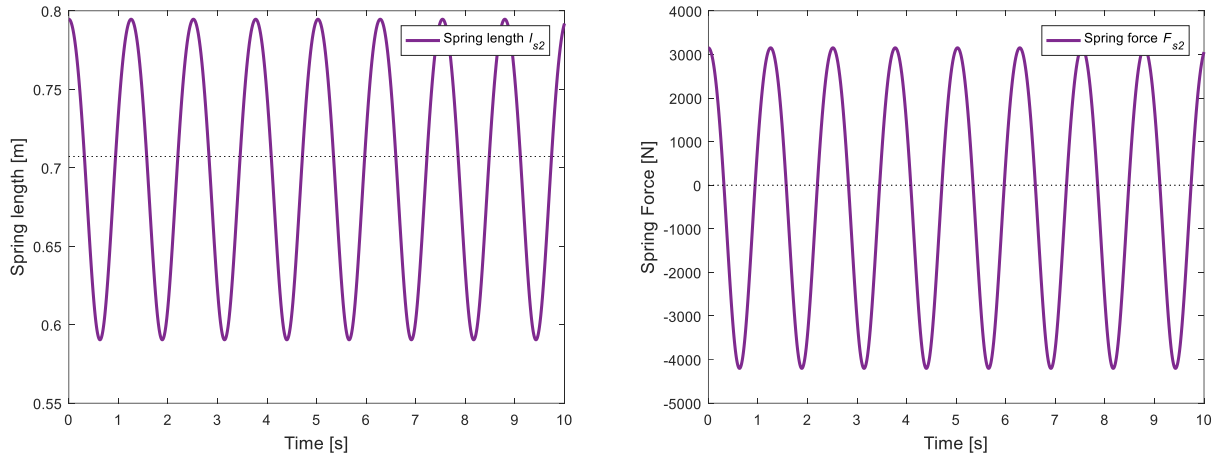

Figure 4.1.5 – Spring length (left) and spring force (right).

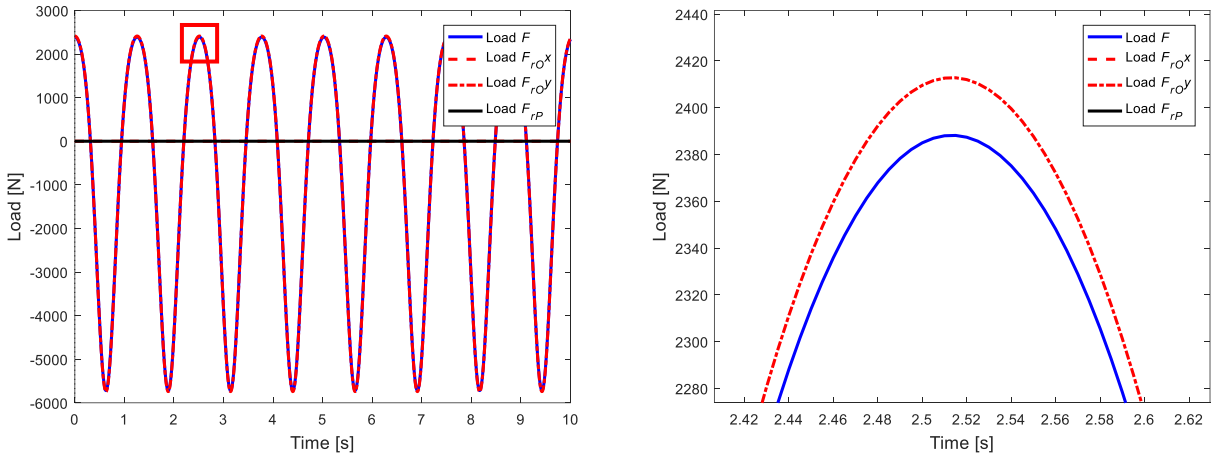

Figure 4.1.6 – Load F and reaction forces at hinge O and P (left) and the zoomed detail (right).

As we are analysing a symmetrical quadrilateral structure now, the lateral forces and inertial moments in the system should be compensated by the left and right parts themselves, which can be confirmed by the transversal constraining forces $F_{rO}x$ and F_{rP} in Figure 4.1.6, where they are both reasonably equal to 0. However, considering the inertia effect, the vertical load F at point P is not identical to the vertical constraining force at hinge O $F_{rO}y$ anymore, there exists a difference between them which is incurred by the inertial force in the system, as shown in the right part of Figure 4.1.6.

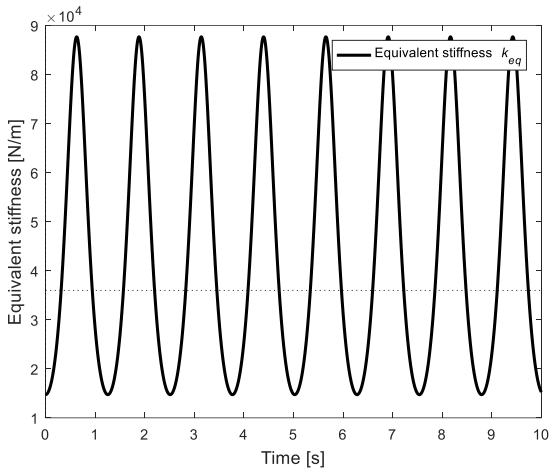

Figure 4.1.7 – Equivalent stiffness.

The equivalent stiffness of the system, when considering the inertial effect, exhibits a similar behaviour as we talked in section 3.3, but it now includes the influence of the inertia effect. The nonlinearity of the system is initially evaluated by the equivalent stiffness in the kinetic model, where the value of the stiffness is coupled with the wheel displacement *h* as shown in Figure 4.1.7. The softening effect and hardening effect will benefit the performance of the suspension regarding different target consequently. In the following content of the thesis, the root cause of the nonlinear characteristic of the system will be discussed by formulating the equation of motion (EOM) of the system, and the effectiveness of the nonlinear behaviour in the system and the vibration response of such a nonlinear system will be discussed based on the EOM.

5. The equation of motion (EOM) of the proposed structure

Vibration is one of the most prevalent phenomena in nature, such as earthquakes and the bumpy ride of a car, and it presents a critical issue in most engineering practices. In many cases, vibration is perceived as a negative factor, such as shortening the service life of equipment and structures, but there are also positive aspects, such as screening of grain. The performance requirements for vibration isolation or suppression include several aspects. A typical example can be seen in the vehicle suspension, crucial for passenger comfort (isolation effect or transmissibility), loading capacity, energy costs, and complexity of implementation. To meet these different demands, various suspension systems are currently employed ranging from conventional spring-damper arrangements to sophisticated active suspensions.

The analysis of vibration response in our proposed novel suspension aims to mitigate the negative aspects of vibration and leverage the positive aspects to optimize the structure. To comprehensively study the vibration response, it's essential to formulate the EOM of the system, which can describe the motion of the system properly. Therefore, this chapter is mainly concentred on the process of defining the expression of the EOM for the system, and the basic idea is to express the load F in the form of ordinary differential equation (ODE), based on the FBDs analysis mentioned before.

5.1 The general EOM

The motion of an undamped vibrating system can be described by the general expression of the ODE as shown in eq. (5.1.1).

$$\mathbf{M}\,\ddot{\mathbf{x}} + \mathbf{K}\,\mathbf{x} = \mathbf{F}(t) \tag{5.1.1}$$

Where **M** is the mass matrix of the system, **K** is the stiffness matrix, **x** is a column matrix in which the generalized coordinates are listed, and **F** is a time-dependent vector containing the forcing functions due to external forces or the motion of the supporting points [30]. Generally speaking, matrices **M** and **K** are symmetrical matrices of order n, where n is the number of degrees of freedom of the system.

For our quadrilateral structure, the motion of the system can be completely described by the wheel motion h as the kinematic model showed before. Therefore, the structure can be considered as a single-degree-of-freedom (SDOF) dynamical system now. The dynamic equilibrium equation of the system can be written as eq. (5.1.2), where the **M** and **K** are all one-dimension values. Due to the nonlinear nature of our system, the mass m and stiffness k are not constant values but are coupled with the displacement h. Hence, they are represented by the equivalent value m_{eq}, and k_{eq} here. The excitation force $F(t)$ on the right hand side of the equation is the load at point P, which is incurred by the external source.

$$m_{eq}\,\ddot{h} + k_{eq}h = F(t) \tag{5.1.2}$$

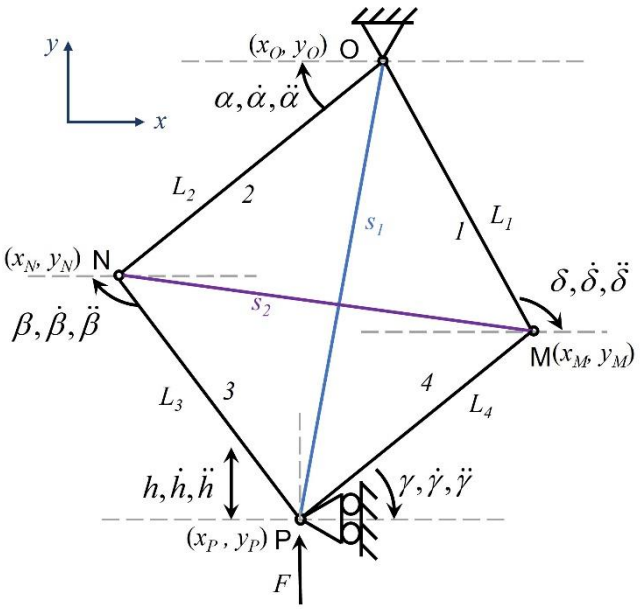

Figure 5.1.1 – Kinematic model of the structure.

5.2 The EOM of each element

Now, to analyse the vibration response of the structure, the main question is how to get the equivalent mass m_{eq} and equivalent stiffness k_{eq} in eq. (5.1.2). Remembering the FBD of the physical model that we already analysed before in Chapter 4, if the suspension works in the normal range of the structure, three equilibrium functions can be listed within each element, and by rewriting the equations, the other three internal forces in each beam can be represented by an unknown force in the *x*-direction. Where the unknown force can be calculated by solving the equilibrium functions at node M and point N. For instance, the force F_{N3x} in element 3 can be explicitly given from aforementioned eq. (4.31).

$$F_{N3x} = \frac{F_{s2}(\cos(\theta_2)\tan(\alpha) + \sin(\theta_2)) + F_{N2\_} + F_{N3\_}}{\tan(\alpha) + \tan(\pi - \beta)} \tag{5.2.1}$$

Where the functions of $F_{N2\_}$ and $F_{N3\_}$ are given below.

$$F_{N2\_} = \frac{\left(-F_{a2x}\frac{L_2\sin(\alpha)}{2} + F_{a2y}\frac{L_2\cos(\alpha)}{2} - I_2\ddot{\alpha}\right)}{L_2\cos(\alpha)} \tag{5.2.2}$$

$$F_{N3\_} = \frac{F_{a3x}\frac{L_3\sin(\pi-\beta)}{2} + F_{a3y}\frac{L_3\cos(\pi-\beta)}{2} - I_3\ddot{\beta}}{L_3\cos(\pi-\beta)} \tag{5.2.3}$$

It should be noted that all the equations are valid only if the angle α is in the range of $\left(0, \frac{\pi}{2}\right)$, and the conditions on the two boundary conditions must be discussed separately. By making a simple consideration of the equations, we can see that the force F_{N3x} is related to the spring force and the inertia force. Therefore, it's possible to represent the force F_{N3x} in the form of an ODE. As we said,

the other forces in element 3 can be represented by F_{N3x}, which means that the motion of element 3 can be described by the EOMs in each direction accordingly. Similarly, by doing the same process in the other beams and summarising the EOMs together, the motion of four elements in three directions respectively can be totally described.

$$\begin{array}{llll}
x_{1G}=\dfrac{x_O+x_M}{2} & x_{2G}=\dfrac{x_O+x_N}{2} & x_{3G}=\dfrac{x_P+x_N}{2} & x_{4G}=\dfrac{x_P+x_M}{2} \\
y_{1G}=\dfrac{y_O+y_M}{2} & y_{2G}=\dfrac{y_O+y_N}{2} & y_{3G}=\dfrac{y_P+y_N}{2} & y_{4G}=\dfrac{y_P+y_M}{2} \\
a_{1x}=\ddot{x}_{1G} & a_{2x}=\ddot{x}_{2G} & a_{3x}=\ddot{x}_{3G} & a_{4x}=\ddot{x}_{4G} \\
a_{1y}=\ddot{y}_{1G} & a_{2y}=\ddot{y}_{2G} & a_{3y}=\ddot{y}_{3G} & a_{4y}=\ddot{y}_{4G} \\
F_{a1x}=m_1a_{1x} & F_{a2x}=m_2a_{2x} & F_{a3x}=m_3a_{3x} & F_{a4x}=m_4a_{4x} \\
F_{a1y}=m_1a_{1y} & F_{a2y}=m_2a_{2y} & F_{a3y}=m_3a_{3y} & F_{a4y}=m_4a_{4y}
\end{array} \tag{5.2.4}$$

The inertial forces in each centroid of each beam have also already been discussed before, they can be represented by the coordinates in the inertial reference frame and the equations are given together in eq. (5.2.4). By writing the inertial force in the coordinate form, the EOM including all components is given by eq. (5.2.5).

$$\mathbf{M}(h)\ddot{\mathbf{z}}+\mathbf{F}_{\mathbf{k}}(h)=\mathbf{F} \tag{5.2.5}$$

Similar but not totally different from the eq. (5.1.2), eq. (5.2.5) serves as the EOM representing the motion of each element, resulting in 12 dofs instead of single dof in the equation. Where **M** is the inertial force incurred mass matrix of order 12, the terms in the matrix **M** are related to displacement h and the general form of the matrix **M** is provided in Appendix A. $\mathbf{F_k}$ is the stiffness force matrix, due to the inclusion of nonlinear trigonometric terms, it can be written as a column vector now instead of a matrix, and the items in the vector $\mathbf{F_k}$ are detailed in Appendix B. The vector **z** contains the translational and rotational motion coordinates of all elements in the system, as listed in eq. (5.2.6). **F** comprises the forces in each element due to the motion of the structure as the vector shown in eq. (5.2.7).

$$\ddot{\mathbf{z}}=\begin{Bmatrix}
\ddot{x}_O \\ \ddot{y}_O \\ \ddot{\delta} \\ \ddot{x}_N \\ \ddot{y}_N \\ \ddot{\alpha} \\ \ddot{x}_P \\ \ddot{y}_P \\ \ddot{\beta} \\ \ddot{x}_M \\ \ddot{y}_M \\ \ddot{\gamma}
\end{Bmatrix} \tag{5.2.6}$$

Where each term in eq. (5.2.6) can be written as a function of the displacement h.

$$\mathbf{F}=\begin{Bmatrix} F_{O1x} \\ F_{O1y} \\ F_{M1y} \\ F_{O2x} \\ F_{O2y} \\ F_{N2y} \\ F_{P3x} \\ F_{P3y} \\ F_{N3y} \\ F_{P4x} \\ F_{P4y} \\ F_{M4y} \end{Bmatrix} \tag{5.2.7}$$

Where the functions $D_1(h)$, $D_2(h)$, $N_1(h)$ and $N_2(h)$ in Appendices A, and B are all trigonometric functions involving the homogeneous denominators and numerators in the matrices. They are expressed by the following equation.

$$D_1(h)=\tan(\gamma)+\tan(\pi-\delta) \tag{5.2.8}$$

$$D_2(h)=\tan(\alpha)+\tan(\pi-\beta) \tag{5.2.9}$$

$$N_1(h)=\cos(\theta_2)\tan(\pi-\delta)-\sin(\theta_2) \tag{5.2.10}$$

$$N_2(h)=\cos(\theta_2)\tan(\alpha)+\sin(\theta_2) \tag{5.2.11}$$

The mass matrix presented in Appendix A seems quite sophisticated for the strong nonlinearity of the system, and it's burdensome to deal with it. However, as we are analysing a special quadrilateral with a symmetrical shape and four identical edges, it's feasible to utilise some special features of the diamond geometry to simplify the terms in the matrices and vectors.

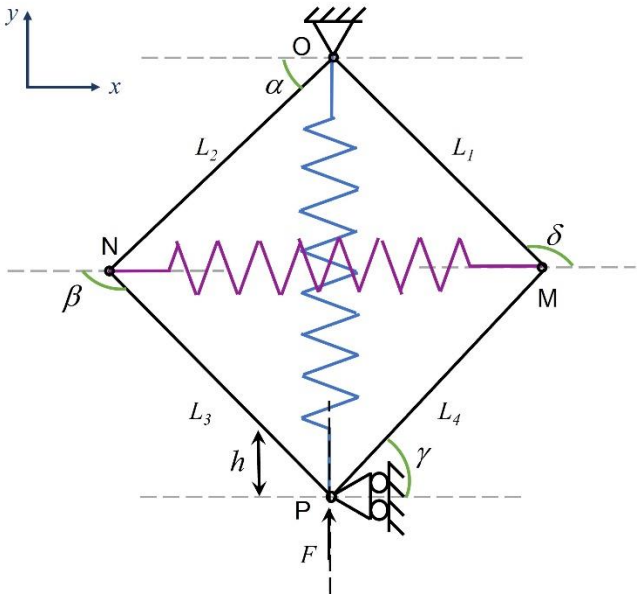

Figure 5.2.1 – Physical model of the specific symmetrical structure.

The relationships between the defined angles are given in eq. (5.2.12) and eq. (5.2.13), and the consistent components in the structure are expected to share the same length, mass, and inertia of moment as shown in eq. (5.2.14) to eq. (5.2.16). By substituting the relations into the general mass matrix and force vector, the simplified formulas and matrices with the specific structure can be derived. The mass matrix **M***(h)* and stiffness vector $\mathbf{F_k}(h)$ under the specific condition are detailed in Appendix C and Appendix D, respectively.

$$\theta_1 = \theta_2 = 0 \tag{5.2.12}$$

$$\alpha = \gamma = \pi - \beta = \pi - \delta \tag{5.2.13}$$

$$L = L_1 = L_2 = L_3 = L_4 \tag{5.2.14}$$

$$m = m_1 = m_2 = m_3 = m_4 \tag{5.2.15}$$

$$I = I_1 = I_2 = I_3 = I_4 \tag{5.2.16}$$

5.3 The EOM of the whole system

Finally, the expression of the excitation force of the whole structure on the right of eq. (5.1.2) can be represented by the internal forces within the corresponding beam by analysing the equilibrium state at point P as shown in Figure 5.3.1.

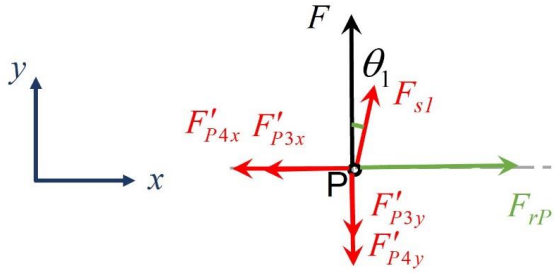

Figure 5.3.1 – Free body diagram of concurrent forces at node P.

$$F = F'_{P4y} + F'_{P3y} - F_{s1}\cos(\theta_1) \tag{5.3.1}$$

Upon analysing the equilibrium function along the *y*-direction at point P, the load *F* is given by the eq. (5.3.1), where, in our specific condition, the angle θ_1 is zero. Extracting the corresponding two internal forces F_{P3y} and F_{P4y} from eq. (5.2.5) and substituting these forces into eq. (5.3.1), we can get the EOM of the system in terms of the displacement *h* and its acceleration $\ddot{h}$. By merging the homogeneous terms in the EOM, m_{eq} and k_{eq} can be determined based on the corresponding coefficient.

The two internal forces F_{P3y} and F_{P4y} are defined by eq. (5.3.3) and eq. (5.3.5) according to the mass matrix in Appendix C and the stiffness force in Appendix D.

$$F'_{P3y} = F_{P3y} \tag{5.3.2}$$

$$F_{P3y} = \frac{\tan(\alpha)}{8}\left(4F_{s2} + m\left(-\ddot{x}_O - 2\ddot{x}_N - \ddot{x}_P\right)\right) + \frac{m}{8}\left(\ddot{y}_O + 4\ddot{y}_N + 3\ddot{y}_P\right) - \frac{I_2\ddot{\alpha}}{L_2\cos(\alpha)} \tag{5.3.3}$$

$$F'_{P4y} = F_{P4y} \tag{5.3.4}$$

$$F_{P4y} = \frac{\tan(\alpha)}{8}\left(4F_{s2} + m\left(\ddot{x}_O + \ddot{x}_P + 2\ddot{x}_M\right)\right) + \frac{m}{8}\left(\ddot{y}_O + 3\ddot{y}_P + 4\ddot{y}_M\right) - \frac{I_4\ddot{\gamma}}{L_4\cos(\alpha)} \tag{5.3.5}$$

By substituting eq. (5.3.3) and eq. (5.3.5) into eq. (5.3.1), we obtain the explicit expression of F, establishing a connection with the structural parameters and the defined angles.

$$F = -F_{s1} + F_{s2}\tan(\alpha) + \frac{\tan(\alpha)}{2}m\ddot{x}_M + \frac{m}{8}\left(2\ddot{y}_O + 6\ddot{y}_P + 4\ddot{y}_N + 4\ddot{y}_M\right) - \frac{2I_2\ddot{\alpha}}{L_2\cos(\alpha)} \tag{5.3.6}$$

Obviously, on the right hand side of the equation, the first two items refer to the stiffness force of the springs, while the remaining terms concern the inertia force of the structure. Hence, the excitation force F now can be represented by two parts of forces: one being the inertia force represented by F_i, and the other one is the stiffness force represented by F_k, which coincide with the general expression of EOM.

$$F = F_i + F_k \tag{5.3.7}$$

Now let's analyse the two parts of force separately. The two forces can be independently given by eq. (5.3.8) and eq. (5.3.9).

$$F_i = \frac{m\ddot{x}_M}{2}\tan(\alpha) + \frac{m}{8}\left(2\ddot{y}_O + 6\ddot{y}_P + 4\ddot{y}_N + 4\ddot{y}_M\right) - \frac{2I_2\ddot{\alpha}}{L_2\cos(\alpha)} \tag{5.3.8}$$

$$F_k = -F_{s1} + F_{s2}\tan(\alpha) \tag{5.3.9}$$

Given the symmetrical nature of the diamond structure, the coordinates of each point and the value of the angle α can be written as a function of displacement h according to the kinematic model, assuming that the angle α is in the range of $\left(0, \frac{\pi}{2}\right)$.

$$x_O = x_P = 0 \tag{5.3.10}$$

$$x_M = -x_N = x_O + L_1\cos(\alpha) \tag{5.3.11}$$

$$y_O = 0 \tag{5.3.12}$$

$$y_P = y_{Po} + h \tag{5.3.13}$$

$$y_M = y_N = \frac{y_O + y_P}{2} = \frac{y_{Po} + h}{2} \tag{5.3.14}$$

$$\alpha = \frac{\pi}{2} - \angle PON \tag{5.3.15}$$

$$\angle PON = \cos^{-1}\left(\frac{\overline{OP}}{2L_2}\right) = \cos^{-1}\left(\frac{-y_{Po} - h}{2L_2}\right) \tag{5.3.16}$$

Where the ordinate y_{Po} is the ordinate of the node P at the static equilibrium position. The second derivative of the coordinates and angles can be directly given by the functions below. Consequently, the motion vector **z** can be written in the form of displacement h by substituting the eq. (5.3.17) to eq. (5.3.20) into the eq. (5.2.6) as shown in Appendix E.

$$\ddot{x}_O = \ddot{x}_P = \ddot{y}_O = 0 \tag{5.3.17}$$

$$\ddot{x}_M = -\ddot{x}_N = -\frac{y_{Po}+h}{2\sqrt{4L_2{}^2-\left(y_{Po}+h\right)^2}}\ddot{h} - \frac{2L_2{}^2}{\left(4L_2{}^2-\left(y_{Po}+h\right)^2\right)^{3/2}}\dot{h}^2 \tag{5.3.18}$$

$$\ddot{y}_P = 2\ddot{y}_M = 2\ddot{y}_N = \ddot{h} \tag{5.3.19}$$

$$\ddot{\alpha} = -\frac{1}{\sqrt{4L_2{}^2-\left(y_{Po}+h\right)^2}}\ddot{h} - \frac{y_{Po}+h}{\left(4L_2{}^2-\left(y_{Po}+h\right)^2\right)^{3/2}}\dot{h}^2 \tag{5.3.20}$$

If we consider the inertial force at first place, we can directly substitute the eq. (5.3.17) to eq. (5.3.20) into the eq. (5.3.8), and consequently, the inertial force is given here in terms of displacement h.

$$F_i = m\left(\frac{5}{4}+\frac{\frac{L_2}{6\cos(\alpha)}-\frac{\left(y_{Po}+h\right)\tan(\alpha)}{4}}{\sqrt{4L_2{}^2-\left(y_{Po}+h\right)^2}}\right)\ddot{h} + m\left(\frac{\frac{\left(y_{Po}+h\right)L_2}{6\cos(\alpha)}-L_2{}^2\tan(\alpha)}{\left(4L_2{}^2-\left(y_{Po}+h\right)^2\right)^{3/2}}\right)\dot{h}^2 \tag{5.3.21}$$

We can observe from the equations above, where the inertia part presents a nonlinear characteristic. The function is not only related to the acceleration of the displacement but also associated with the square of the velocity, which is unusual in the general EOM.

$$F_i = m_{eq}\ddot{h} + F_{ir}\left(h\right)\dot{h}^2 = m(f_1\left(h\right)\ddot{h} + f_2\left(h\right)\dot{h}^2) \tag{5.3.22}$$

$$f_1\left(h\right) = \frac{5}{4}+\frac{\frac{L_2}{6\cos(\alpha)}-\frac{\left(y_{Po}+h\right)\tan(\alpha)}{4}}{\sqrt{4L_2{}^2-\left(y_{Po}+h\right)^2}} \tag{5.3.23}$$

$$f_2\left(h\right) = \frac{\frac{\left(y_{Po}+h\right)L_2}{6\cos(\alpha)}-L_2{}^2\tan(\alpha)}{\left(4L_2{}^2-\left(y_{Po}+h\right)^2\right)^{3/2}} \tag{5.3.24}$$

For a more insightful analysis of the nonlinearity, we will introduce two nonlinear functions $f_1(h)$, and $f_2(h)$ respectively. Here $f_1(h)$ pertains the equivalent mass in the system, and $f_2(h)$ relates to the unique conservative inertia force F_{ir}, which will be discussed in detail in Chapter 6.
Another part is related to the stiffness of the system, which is determined by the springs. By substituting the equations of two spring forces into the eq. (5.3.9), the stiffness force can be expressed as a sum of a linear part and a nonlinear part as eq. (5.3.28) shows. We will also introduce a nonlinear function, $f_3(h)$, to better analyse the characteristic of the equivalent stiffness, which will be discussed further in Chapter 6.

$$F_{s1} = k_{s1}\Delta l_1 = k_{s1}(\overline{OP}-l_{o1}) = -k_{s1}h \tag{5.3.25}$$

$$F_{s2} = k_{s2}\Delta l_2 = k_{s2}(\overline{MN}-l_{o2}) = k_{s2}\left(x_M - x_N - l_{o2}\right) \tag{5.3.26}$$

$$F_k = k_{s1}h + k_{s2}f_3\left(h\right) \tag{5.3.27}$$

$$f_3(h) = 2L\sin(\alpha) - l_{o2}\tan(\alpha) \tag{5.3.28}$$

$$mf_1(h)\ddot{h} + mf_2(h)\dot{h}^2 + k_{s1}h + k_{s2}f_3(h) = F \tag{5.3.29}$$

In the end of this section, we finally obtain an EOM as shown in eq. (5.3.29) by analysing the expression of the load F under a specific condition, where the mass and stiffness of the system have a nonlinear characteristic, attributed to the quadrilateral structure. Also, the equation is valid only if the angle α works in the range of $\left(0, \frac{\pi}{2}\right)$. It's physically meaningless if α equals to 0 or $\frac{\pi}{2}$, since the suspension can never fold together in reality. While it is necessary to consider these boundary conditions mathematically for completeness in the analysis as the discussion in section 5.4.

5.4 Validation of the specific EOM

To validate the effectiveness of the EOM for the whole system as shown in eq. (5.3.29), and to interpret the physical meaning of each part simultaneously, we will analyse the EOM of the physical model without considering inertia effect and stiffness force separately in this section.

5.4.1 Inertia part of the model

To assess the correctness of the nonlinear inertia force derived from eq. (5.2.5) in relation to the motion of each element, the specific quadrilateral structure is modelled without considering the springs. In this section, the behaviour of the system is only determined by the inertial effect.

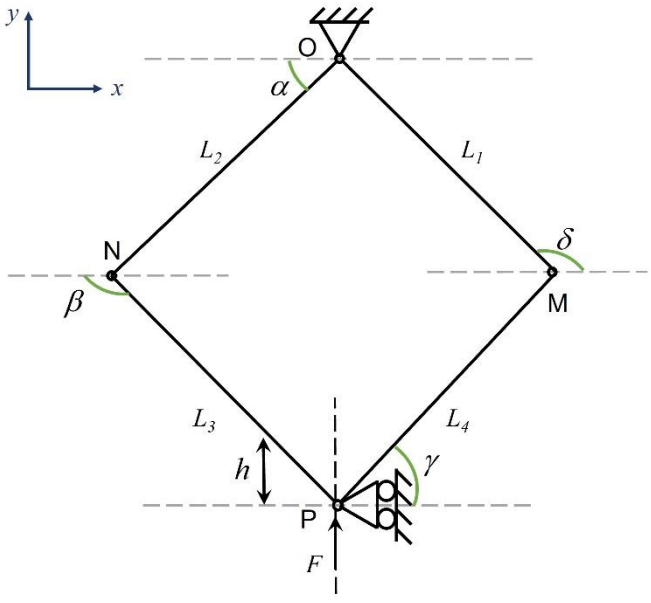

Figure 5.4.1.1 – The model considering the inertia.

Recalling the internal forces in each element from the FBD analysis section in Chapter 4, now let's discard the stiffness component in every equation, and the load F can be rewritten by analysing the equilibrium state at point P again as follows:

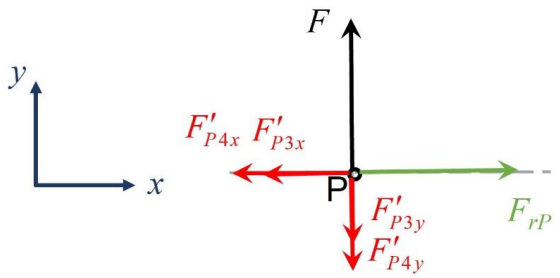

Figure 5.4.1.2 – Free body diagram of concurrent forces at node P without stiffness force.

Still, the load F can be expressed by the internal forces by analysing the equilibrium state at point P along the y direction.

$$F = F'_{P4y} + F'_{P3y} \tag{5.4.1.1}$$

Where the internal forces will be directly given in the context of this specific geometry, the process of substituting all trigonometric identities with the angle α and simplifying the equations will not be elaborated in this section.

$$F'_{P3y} = F_{P3y} = -F_{N3y} + F_{a3y} \tag{5.4.1.2}$$

$$F'_{P4y} = F_{P4y} = -F_{M4y} + F_{a4y} \tag{5.4.1.3}$$

$$F_{N3y} = -\frac{F_{a2y}}{4} + \frac{F_{a3y}}{4} + \frac{F_{a3x}}{2}\tan(\alpha) + \frac{I\ddot{\alpha}}{L\cos(\alpha)} \tag{5.4.1.4}$$

$$F_{M4y} = -\frac{F_{a1y}}{4} + \frac{F_{a4y}}{4} - \frac{F_{a4x}}{2}\tan(\alpha) + \frac{I\ddot{\alpha}}{L\cos(\alpha)} \tag{5.4.1.5}$$

Substituting the eq. (5.4.1.2) to eq. (5.4.1.5) into eq. (5.4.1.1), it becomes apparent that the load F incurred by the inertia effect is given by three parts: the inertial force along x and y directions, and the inertial moment correspondingly as shown in eq. (5.4.1.6).

$$F = \frac{F_{a1y}}{4} + \frac{F_{a2y}}{4} + \frac{3F_{a3y}}{4} + \frac{3F_{a4y}}{4} - \frac{F_{a3x}}{2}\tan(\alpha) + \frac{F_{a4x}}{2}\tan(\alpha) - \frac{2I\ddot{\alpha}}{L\cos(\alpha)} \tag{5.4.1.6}$$

As the inertial forces have already provided in eq. (5.2.4), the load F can be represented in the form of inertial coordinates of each point by substituting the inertial forces into eq. (5.4.1.6). Finally, the load F is given by eq. (5.4.1.7), and obviously, it's equivalent to eq. (5.3.8). It implies that the nonlinear inertia effect, as evaluated in the entire system, is corresponding to the model eliminating the stiffness component.

$$F = \frac{m\ddot{x}_M}{2}\tan(\alpha) + \frac{m}{8}\left(2\ddot{y}_O + 6\ddot{y}_P + 4\ddot{y}_N + 4\ddot{y}_M\right) - \frac{2I\ddot{\alpha}}{L\cos(\alpha)} \tag{5.4.1.7}$$

In conclusion, the analysis of the entire system yields a specific EOM, and modelling the system solely considering the inertia effect results in a more physically meaningful equation that captures the nonlinear inertia characteristic. The consistency between these two approaches confirms the effectiveness of eq. (5.3.8).

5.4.2 Stiffness part of the model

At the beginning of the research, a simplified model, depicted in Figure 5.4.2.1, initially excluded the mass of each element for ease of analysis. In this scenario, where the inertia effect is absent, the structure only exhibits an elastic response. The beams can be considered as rod elements, and consequently the load F can be given by the eq. (5.4.2.1), a formula we previously delved into during our discussion in section 3.1.

$$F = -F_{s1}\cos(\theta_1) - F_{s2}\left(\tau_3 \sin(\pi-\beta) + \tau_4 \sin(\gamma)\right) \tag{5.4.2.1}$$

In which the two coefficients τ_3 and τ_4 are given by.

$$\tau_3 = \frac{-\sin(\theta_2) - \cos(\theta_2)\tan(\alpha)}{\sin(\pi-\beta) + \cos(\pi-\beta)\tan(\alpha)} \tag{5.4.2.2}$$

$$\tau_4 = \frac{\sin(\theta_2) - \cos(\theta_2)\tan(\pi-\delta)}{\sin(\gamma) + \cos(\gamma)\tan(\pi-\delta)} \tag{5.4.2.3}$$

By substituting the symmetrical relationships of defined angles outlined in eq. (5.2.12) and eq. (5.2.13) into τ_3, τ_4 and eq. (5.4.2.1), the expression of load F regarding the stiffness force is finally derived, as presented in eq. (5.4.2.4).

$$F = -F_{s1} + F_{s2}\tan(\alpha) \tag{5.4.2.4}$$

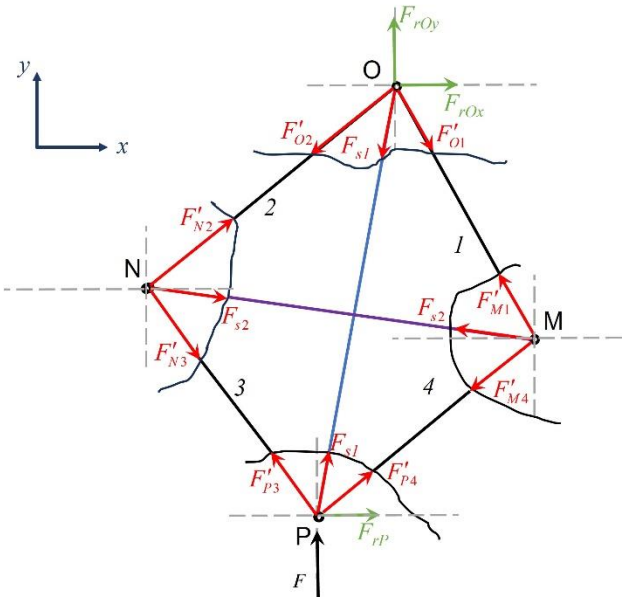

Figure 5.4.2.1 – The stiffness model.

Obviously, the load F of the simplified model as shown in eq. (5.4.2.4) is identical to the nonlinear stiffness force in the whole system, as illustrated in eq. (5.3.9) discussed before. This verification reaffirms the accuracy and effectiveness of the stiffness force in the entire specific EOM.

5.5 The two boundary conditions

It is crucial to emphasise that the FBD, kinematic model and the EOM analysed before are all based on the suspension functioning within its working range. Which means that the angle α should in the boundary of $\left(0,\frac{\pi}{2}\right)$. When the structure reaches the boundary conditions, the four points of the quadrilateral will align in a straight line, leading the dynamical system to cross a zero position. The zero-crossing condition holds significance in a dynamical system, as it has the potential to suddenly alter the behaviour of the system or even constrain its dof. Although our structure can never reach these limits due to the presence of springs, and these situations are practically meaningless for a suspension, examining the boundary conditions can enhance our comprehension of the system's dynamical behaviour later. The boundary analysis will be performed below.

5.5.1 Horizontally aligned condition

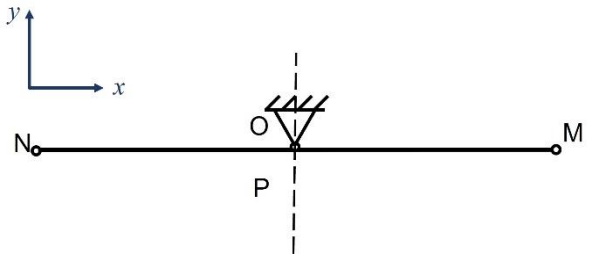

Figure 5.5.1.1 – Boundary state in which the four beams are horizontally aligned.

If the structure is in a position where the four beams are horizontally aligned, the angle $\alpha = 0$, and the FBD of the system in this special state can be analysed as shown below.

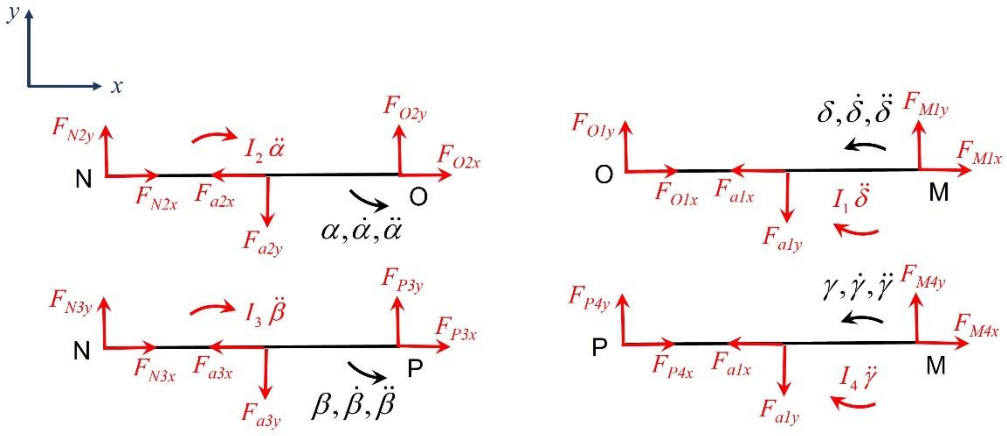

Figure 5.5.1.2 – FBD of each element if the beams are horizontally aligned.

Since the internal force along *x* and *y* directions are decoupled now, the force in the y direction can be calculated directly by the moment balance in each beam, and the forces are given by:

$$F_{M1y} = \frac{F_{a1y}}{2} + \frac{I\ddot{\delta}}{L} \tag{5.5.1.1}$$

$$F_{M4y} = \frac{F_{a4y}}{2} + \frac{I\ddot{\gamma}}{L} \tag{5.5.1.2}$$

$$F_{N2y} = \frac{F_{a2y}}{2} - \frac{I\ddot{\alpha}}{L} \tag{5.5.1.3}$$

$$F_{N3y} = \frac{F_{a3y}}{2} - \frac{I\ddot{\beta}}{L} \tag{5.5.1.4}$$

Where the relationship of the angles is already given in eq. (5.2.13). By considering the equilibrium state at points N and M in the *y* direction, the relations between the internal forces can be expressed as:

$$\frac{F_{a1y}}{2} + \frac{I\dddot{\delta}}{L} + \frac{F_{a4y}}{2} + \frac{I\ddot{\gamma}}{L} = 0 \tag{5.5.1.5}$$

$$F_{a1y} = -F_{a4y} \tag{5.5.1.6}$$

$$\frac{F_{a2y}}{2} - \frac{I\ddot{\alpha}}{L} + \frac{F_{a3y}}{2} - \frac{I\ddot{\beta}}{L} = 0 \tag{5.5.1.7}$$

$$F_{a2y} = -F_{a3y} \tag{5.5.1.8}$$

With the analysis, it becomes evident that in the horizontal alignment position, the acceleration along the *y* direction on the same side of the structure present a negatively equivalent relationship, which is different from the analysis conducted in the working range. It signifies s a discontinuity in the position under investigation. When the system crosses this special position, the performance and state of the system undergo a sudden change. Hence, it is crucial to acknowledge that the analysis of the system is given under the assumption that it operates within its working range. The validity of the EOM is contingent on this assumption, otherwise, the simulation and conclusion of the analysis could incorrectly describe the system.

5.5.2 Vertically aligned condition

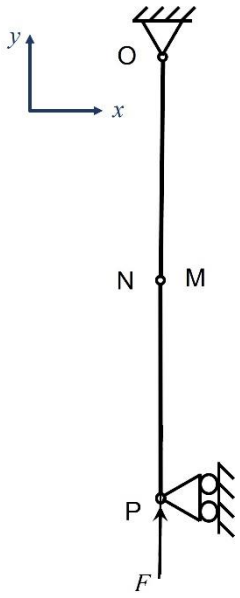

Figure 5.5.2.1 – Boundary state in which the four beams are vertically aligned.

If the beams in the structure are vertically aligned together, as depicted in Figure 5.5.2.1, with the angle $\alpha = \frac{\pi}{2}$, the dynamical system loses its freedom. This is because the forces in the structure and the transmission mechanisms are aligned in a straight line. In this position, the EOM of the system cannot be formulated. The assumption that the beams are rigid bodies leads to an infinite equivalent mass m_{eq} of the system in this situation. Consequently, if we attempt to induce rotation in the beams through a vertical force F, the magnitude of the force required becomes infinite. This can be observed from eq. (5.4.1.6), where the trigonometric identities $\tan(\alpha) = \infty, \cos(\alpha) = 0$ result in an infinite magnitude for load F.

5.6 Conclusion

In this chapter, we have developed the EOM of the specific structure to facilitate the analysis of its dynamical performance later on. The nonlinear EOM is derived based on the FBD analysis discussed in the preceding section. By adopting the form of the ODE and introducing three nonlinear functions $f_1(h)$, $f_2(h)$, and $f_3(h)$, the inherent nonlinear characteristics of the system are captured. Finally, the validation of the EOM is carried out by separately examining the inertia and stiffness effects with two distinct models correspondingly, which not only confirms the effectiveness of the EOM for the entire system but also provides insights into the physical meaning of each component. The equivalent mass and equivalent stiffness of the system in eq. (5.1.2) is evaluated from the three nonlinear functions, in the next chapter we will focus on the nonlinearity and the unique characteristic of each nonlinear part within the system correspondingly.

6. The unique nonlinear features

In Chapter 5, a SDOF nonlinear time-variant mass-spring system was evaluated, according to eq. (5.3.29), the nonlinear characteristics of the novel structure were determined by three nonlinear items: the nonlinear equivalent mass m_{eq} incurred by the inertia effect, the nonlinear force F_{ir} incurred by the rotational unit, and the nonlinear stiffness k_{eq} incurred by the quadrilateral-shaped structures. In this chapter, our focus shifts to understanding the influence of these nonlinear characteristics, which are incurred by the uniquely shaped structure and the rotational effect, actually represented by the three nonlinear functions $f_1(h)$, $f_2(h)$, and $f_3(h)$ in the dynamical system The structural parameters of the assumed diamond structure, as shown in Figure 5.2.1, are detailed in Table 6.1.

Table 6.1 – Structural parameters in the static state.

Parameter	Value
(x_O, y_O) [m]	(0, 0)
(x_P, y_P) [m]	(0, -0.7071)
(x_M, y_M) [m]	(0.3536, -0.3536)
(x_N, y_N) [m]	(-0.3536, -0.3536)
L_1 [m]	0.5
L_2 [m]	0.5
L_3 [m]	0.5
L_4 [m]	0.5
α [°]	45
β [°]	135
γ [°]	45
δ [°]	45
$\overline{OP}$ [m]	0.7071
$\overline{MN}$ [m]	0.7071
k_{s1} [N/m]	0
k_{s2} [N/m]	36000
l_{o1} [m]	$\overline{OP}$
l_{o2} [m]	$\overline{MN}$
Wheel travel [m]	[-0.1, 0.1]
D [m]	0.04
ρ [kg/m^3]	7850

6.1 Nonlinear inertia incurred equivalent mass

The nonlinear inertia part of the EOM gives rise to the nonlinear equivalent mass m_{eq}, determined by the nonlinear function $f_1(h)$. According to eq. (5.3.22), the function $f_1(h)$ is dependent on the displacement h, and is related to the length of the beams and the static geometry of the quadrilateral. Using the structural parameters listed in Table .6.1, the function value of the $f_1(h)$ can be plotted against the displacement h. During the transition from the rebound phase to the jounce phase, the function value progressively decreases from a relatively larger value to a relatively smaller value, with the slope of curve gradually decreasing, indicating a nonlinear behaviour of the equivalent mass in the system.

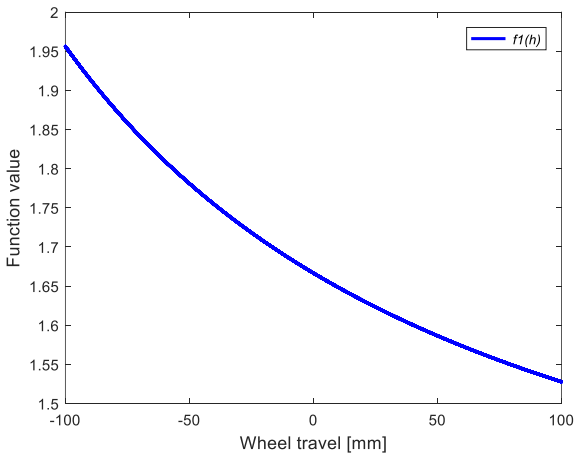

Figure 6.1.1 – The function value of $f_1(h)$ vs. displacement.

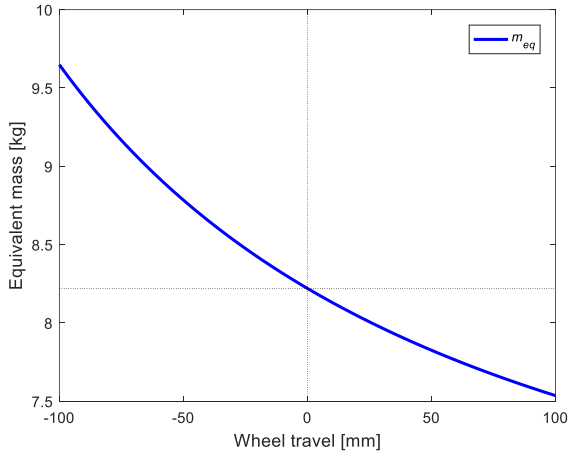

Figure 6.1.2 – The equivalent mass of the system vs. displacement.

As depicted in Figure 6.1.2, the equivalent mass can be evaluated by the nonlinear function, obtained by multiplying the mass of the beam. The plot shows the nonlinear variation of the equivalent mass with displacement h. When the structure is compressed, the equivalent mass becomes smaller, and vice versa when it is stretched. This nonlinear trend is very beneficial for the vibration isolation of our novel suspension, as the smaller mass in compression result in a smaller reactive force when the wheel passes over the humps or obstacles. The customizable nature of the function $f_1(h)$ by adjusting the structural parameters allows tuning the tendency of mass variations with the displacement h, enabling the optimization of the response characteristics by analysing the influence of each structural parameters on the function value.

6.2 Nonlinear inertia incurred conservative force

The nonlinearity of the system introduces a unique part represented by F_{ir}, which is not only dependent on the displacement h but also involves its velocity, and the force was incurred by the rotational motion of the element. The value of nonlinear function $f_2(h)$ is depicted in Figure 6.2.1. This component is distinctive in the motion equation and, due to its complex coupling dynamics with the specific quadrilateral, it can have a more intricate nonlinear effect on the system dynamics. While analysing such a complex part might be challenging initially, Feng et al. [31] conducted

some work on their HBIAVS-NI vibration isolation structure, addressing a similar nonlinear force. Their findings provide valuable insights that can inspire our research. The incurred conservative force undoubtedly is a nonlinear force and can be tuned based on the designed parameters. Feng et al. found that the nonlinear characteristic of the inertia incurred conservative force F_{ir} is highly beneficial for vibration control and improves obviously the stability of the system. The mass centre is maintained with a relatively constant contact force with the ground, as a vehicle suspension on rough ground as shown in Figure 6.2.2. They noted that, compared with the linear system, with the effects of the nonlinear inertia incurred conservative force, the fluctuation of the force in the extension and compression process is obviously reduced and maintained at a stable value. In contrast, the traditional spring system exhibit more significant changes in supporting force. The outcome of their research highlights that this nonlinear force provides a strong benefit for vibration control, however, given that this partition in our system is relatively small, the effect on vibration isolation may not be immediately apparent. Further details on this aspect with be provided in chapter 8.

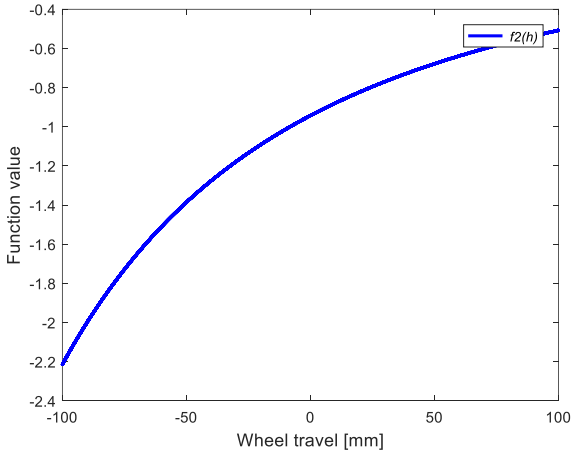

Figure 6.2.1 – The function value of $f_2(h)$.

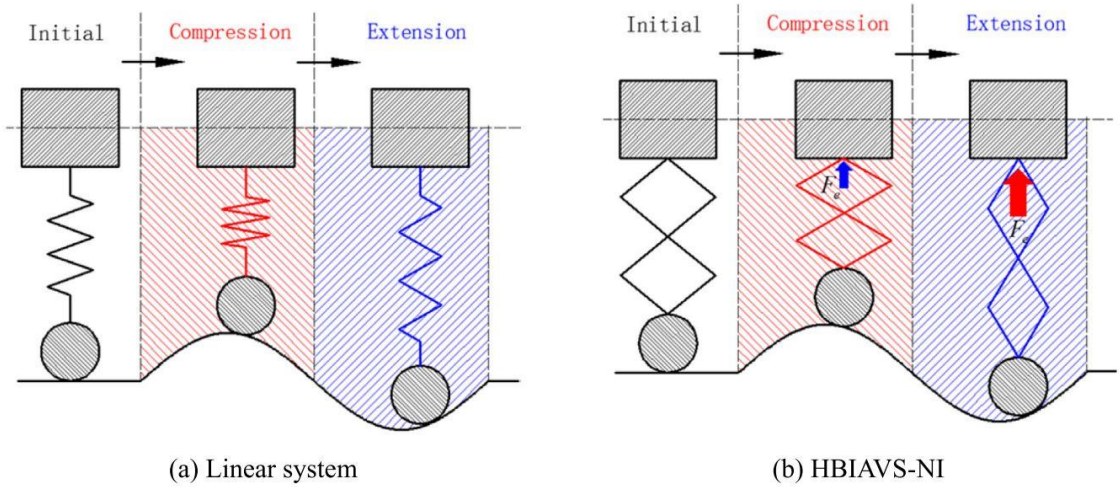

Figure 6.2.2 – Example of energy dissipated by nonlinear inertia incurred conservative force [31].

6.3 Nonlinear stiffness

The nonlinear stiffness part, represented by F_k and determined by the nonlinear function $f_3(h)$, is depicted in Figure 6.3.1 against displacement h. Observing the graph, it is evident that the function value is positive for positive h and negative for negative h correspondingly. The slope of the curve gradually decreases from the max negative h to max positive h, indicating that the nonlinear stiffness force, which results in an equivalent spring in the system, is compressed in the jounce phase and stretched in the rebound phase. The equivalent stiffness of the system is gradually softened from the rebound phase to the jounce phase. The equivalent stiffness is also plotted in Figure 6.3.2.

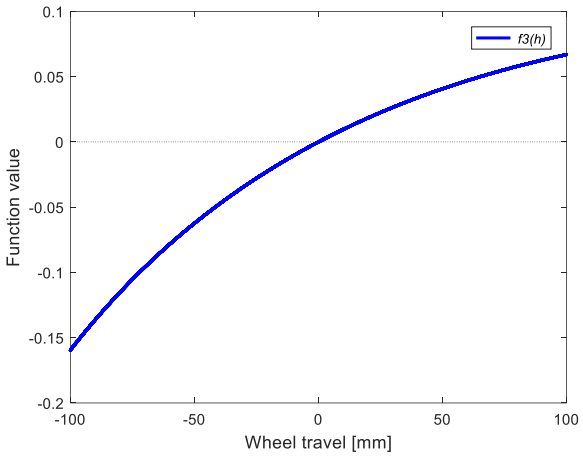

Figure 6.3.1 – The function value of $f_3(h)$.

$$k_{eq} = \frac{dF_k}{dh} = k_{s1} + k_{s2}\frac{df_3(h)}{dh} \tag{6.3.1}$$

$$\frac{df_3(h)}{dh} = -1 + \frac{4l_{o2}L_2^{\,2}}{\left(4L_2^{\,2} - \left(y_{Po} + h\right)^2\right)^{3/2}} \tag{6.3.2}$$

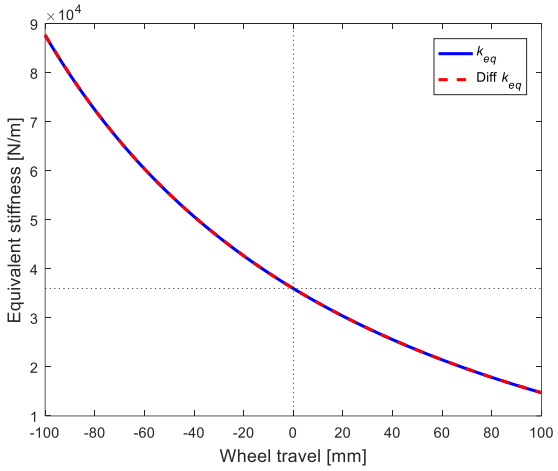

Figure 6.3.2 – The equivalent stiffness of the system.

By calculating the derivative of $f_3(h)$ with respect to h, the equation of equivalent stiffness is given by eq. (6.3.1). To verify the accuracy of the equivalent stiffness, a comparison is made with the differential value of the force F using MATLAB and the simplified model that excludes the inertia

of each element, as discussed in section 3.3. The result depicted in Figure 6.3.2 shows the two curves superimposed, demonstrating the effectiveness of the equivalent stiffness derived from $f_3(h)$. The tendency of the equivalent stiffness has already been discussed before, and the softening effect in the compression contributes to comfort improvement meanwhile the hardening effect in the extension phase provides additional support force in the suspension ensuring the stability of the structure. The agreement between the two methods also indicates that the simplified model is equivalent to a nonlinear time variant spring as shown in Figure 6.3.3.

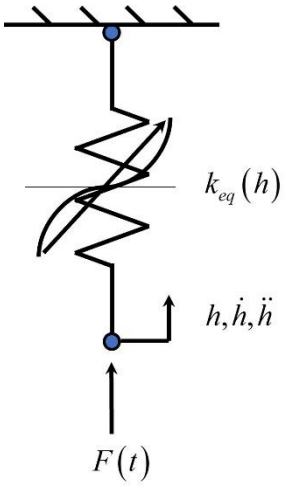

Figure 6.3.3 – The simplified model is equivalent to a nonlinear spring.

7. Linearised frequency response

The nonlinear mass-spring system shows some unique nonlinear characteristics, as discussed in Chapter 6. Analysing its frequency response directly is challenging due to the presence of jump phenomena. To start the evaluation of its dynamical performance, we will begin by analysing three special positions-one in the initial position and two boundary conditions. The EOM will be linearised by assuming a very small displacement imposed by a harmonic excitation force in each equilibrium position, where the inertial force incurred by rotational unit can be discarded temporarily. By calculating the equivalent mass and equivalent stiffness, the natural frequency at each position can be obtained using eq. (7.2.3), and consequently the frequency response of the linearised mass-spring system can be shown finally. The structural parameters remain the same as listed in Table .6.1.

7.1 Three equilibrium positions

To analyse the nonlinear vibration response of the system, we can start by examining the linear behaviour of some particular positions. By finding out how these responses transform from one to another position, we can gain insights into the nonlinear performance of the system better. Three positions will be considered here: the initial position and two boundary positions where the suspension nearly reaches the bump stop. The data for each equilibrium position are given in Table .7.1.1. At each equilibrium position, the system can be linearised by supposing a very small displacement excited by an external harmonic force, and the EOM becomes a linear differential equation now as shown in eq. (7.1.1). For these small displacements in each position, the equivalent mass and equivalent stiffness are assumed constant.

$$m_{eq}\ddot{h} + k_{eq}h = F(t) \tag{7.1.1}$$

Table 7.1.1 – Structural parameters for three positions.

Parameter	Value
Position1 (lower boundary)	
α [°]	35
β [°]	145
γ [°]	35
δ [°]	145
$\overline{OP}$ [m]	0.5736
$\overline{MN}$ [m]	0.8192
Position2 (initial position)	
α [°]	45
β [°]	135
γ [°]	45
δ [°]	135
$\overline{OP}$ [m]	0.7071
$\overline{MN}$ [m]	0.7071
Position3 (upper boundary)	
α [°]	55

β [°]	125
γ [°]	55
δ [°]	125
$\overline{OP}$ [m]	0.8192
$\overline{MN}$ [m]	0.5736

Three positions of the structure are depicted in Figure 7.1.1.

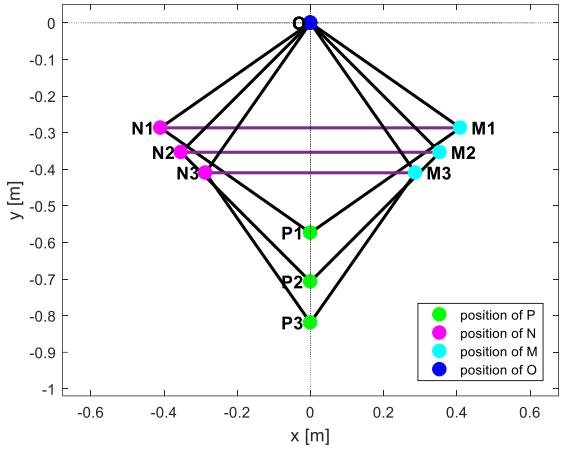

Figure 7.1.1 – Three different equilibrium positions.

7.2 Natural frequency

By rewriting eq. (7.1.1), we can get a more general expression of the linearised EOM, wherein the natural frequency can be calculated using the equivalent mass and stiffness. The value of m_{eq} and k_{eq} can be given by the equation obtained in sections 6.1 and 6.3, with the geometric parameters at each position as detailed in Table 7.1.1.

$$\ddot{h} + \frac{k_{eq}}{m_{eq}} h = \frac{F(t)}{m_{eq}} \tag{7.2.1}$$

$$\ddot{h} + \omega_n{}^2 h = \frac{\omega_n{}^2 F(t)}{k_{eq}} \tag{7.2.2}$$

$$\omega_n = \sqrt{\frac{k_{eq}}{m_{eq}}} \tag{7.2.3}$$

The trend of natural frequency, as depicted in Figure 7.2.1, has a similar characteristic with the equivalent stiffness, further revealing the softening effect in the compression phase and the hardening effect in the rebound phase. The value of equivalent mass, equivalent stiffness and natural frequency at each position are listed in Table 7.2.1.

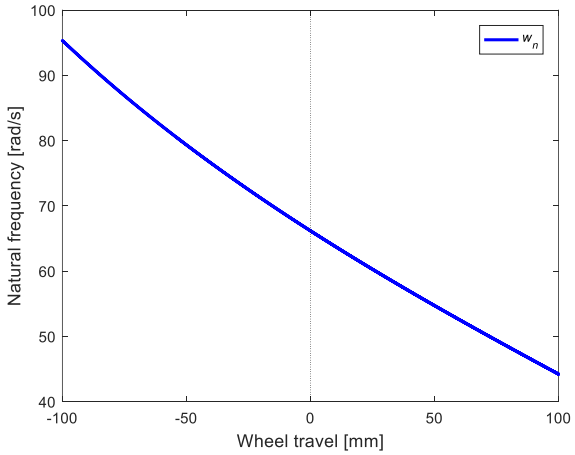

Figure 7.2.1 – The natural frequency vs. displacement.

Table 7.2.1 – Structural parameters for three positions.

Parameter	Value
Position1 (lower boundary)	
k_{eq} [N/m]	176500
m_{eq} [kg]	7.3825
ω_n [rad/s]	48.8964
Position2 (initial position)	
k_{eq} [N/m]	360000
m_{eq} [kg]	8.2205
ω_n [rad/s]	66.1762
Position3 (upper boundary)	
k_{eq} [N/m]	734260
m_{eq} [kg]	9.9297
ω_n [rad/s]	85.9916

7.3 Forced frequency response (Harmonic excitation)

Supposing a harmonic forced excitation with frequency ω as in eq. (7.3.1) is applied to the system at each position, the reactive displacement correspondingly has the same frequency as the excitation, where the transient response at each position is ignored, and it can be expressed by eq. (7.3.2). By calculating the derivative of such a harmonic displacement and substituting it into eq. (7.2.2), the frequency response of the system can be obtained in eq. (7.3.4). The linearised response modulus and response phase can then be calculated by the frequency response function at each position. The bode diagram of the response function is depicted in Figure 7.3.1.

$$F(t) = F_o e^{i\omega t} \tag{7.3.1}$$

$$h(t) = h_o e^{i\omega t} \tag{7.3.2}$$

$$-\omega^2 h_o e^{i\omega t} + {\omega_n}^2 h_o e^{i\omega t} = \frac{{\omega_n}^2 F_o e^{i\omega t}}{k_{eq}} \tag{7.3.3}$$

$$\frac{h_o}{F_o / k_{eq}} = \frac{1}{1 - \frac{\omega^2}{{\omega_n}^2}} \tag{7.3.4}$$

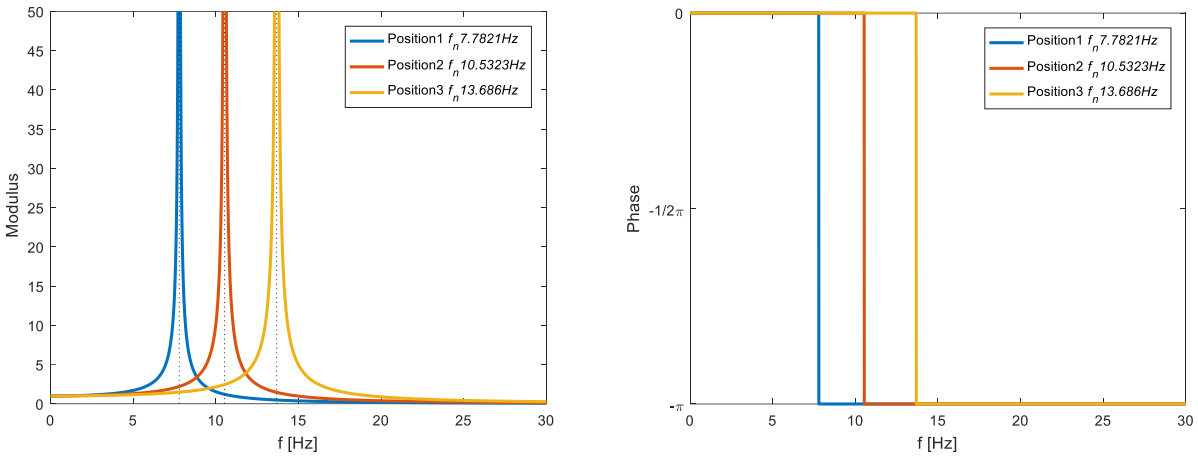

Figure 7.3.1 – The bode diagram of three frequency response at each position.

Three resonant frequencies are marked with dotted black line in the modulus plot. The curves show the typical vibration characteristic of a simple linear undamped mass-spring vibration system. When the frequency ω equals to 0, the modulus of the displacement equals to 1, indicating no increment or suppression in the response. With the increase of the force frequency, the modulus of the response successively increases, approaching to infinity when it approaches the resonant frequency, demonstrating a resonant effect. The evidence of the resonance can be also seen from the phase response plot. The phase becomes $-\frac{\pi}{2}$ from the in-phase state abruptly at the resonant frequency, indicating the accompanying state exists and the reasoning phenomenon occurs. As the frequency increases from the resonant frequency, the response transitions to the out-phase state, the modulus decreases from infinite to nearly 0, and the phase response changes from $-\frac{\pi}{2}$ to $-\pi$, signifying an opposite phase relationship between the excitation and the response, leading to a suppression effect in the displacement response amplitude.

8. Step response

In many situations, the periodic excitation or long term (steady state) response of a vibrating system is of interest. For example, in the case of a motor operating at a fixed speed most of the time, understanding the response at that speed is crucial for designing an effective vibration isolation system. On the other hand, there are scenarios where the non-periodic transient response of the system becomes significant:

- For the motor example above, during the startup of a motor, especially if the system passes through resonance.
- The response of an automobile suspension system when a pothole or other obstacle in the road is encountered.
- The response of various mechanical systems to shock loading.

In these cases, the loading is either non-periodic or is applied for a short duration.
Given that our structure is mounted on a suspension that experiences a non-periodic excitation while the car is in motiom, it is critical to analyse the transient response of the system. In this chapter, we will exam the step responses of our structure and assess its performance compared to the linearised structure. For simplicity, when investigating the step excitation of a dynamical system, we typically focus on undamped linear systems. The general form of the EOM for such system is given by:

$$\mathbf{M}\,\ddot{\mathbf{x}} + \mathbf{K}\,\mathbf{x} = \mathbf{F}(t) \tag{8.1}$$

Where **F**(t) is the disturbing force under consideration. Considering a simple linear spring-mass system subjected to a rectangular step load as shown in Figure 8.1, where the output load F is changed suddenly to F_0 from 0 at step time t_0. The load can be mathematically represented by eq. (8.2), and we will consider the step time t_0 to be 0 in our analysis.

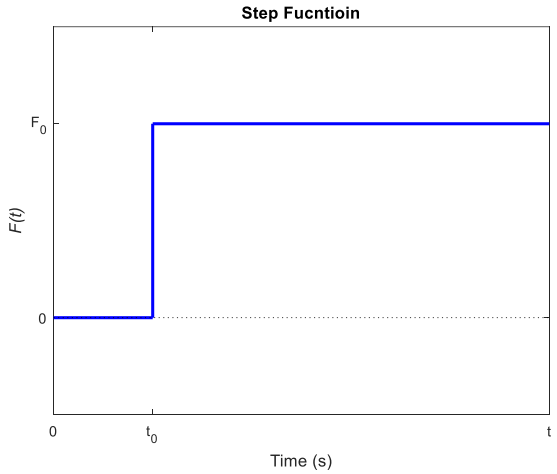

Figure 8.1 – The step function of the excitation force.

$$F(t) = \begin{cases} 0, t < t_0 \\ F_0, t \geq t_0 \end{cases} \tag{8.2}$$

To evaluate the response of the displacement to this transient loading condition, considering the superposition property of the linear dynamical system, the solution should be composed of a homogeneous and a particular part which is given by eq. (8.3).

$$x(t) = A\sin(\omega_n t) + B\cos(\omega_n t) + x_P(t) \tag{8.3}$$

Where ω_n is the natural frequency of the linear system.

For the constant excitation force F_0 after step time, the particular solution can be directly given by considering the application of the force to the structure statically.

$$x_P(t) = \frac{F_0}{k} \tag{8.4}$$

The homogeneous part is related to the initial conditions, and we suppose that the system vibrates always from the zero state where the initial position and initial velocity are given by 0. The natural frequency ω_n is determined by the mass and stiffness of the system, as we talked before.

$$x(0) = 0, \dot{x}(0) = 0 \tag{8.5}$$

By substituting the initial conditions into the eq. (8.3), the two constants A, and B in the homogeneous solution become.

$$A = 0, B = -\frac{F_0}{k} \tag{8.6}$$

So, the complete solution finally can be written as following equation, and the corresponding displacement of the mass in response to the step input in the time domain is shown in Figure 8.2.

$$x(t) = \frac{F_0}{k}\left(1 - \cos(\omega_n t)\right) \tag{8.7}$$

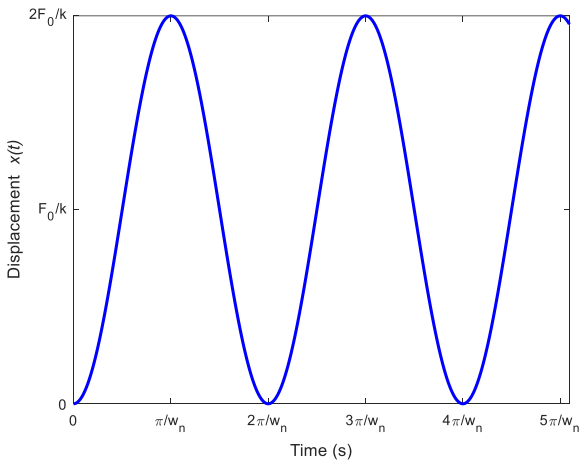

Figure 8.2 – Response of the simple mass-spring system to step input.

We can see that the maximum displacement of the mass is twice the deflection that would have resulted if the load were applied statically when we the step time t_0 equals to 0 and the initial condition is at the zero state. As in the kinetic analysis we performed before, the plot of load F versus a quasi-static wheel displacement in the range of [-100mm, 100mm] is illustrated in Figure 8.3, from which we can see that the step force F_0 should be considered within the boundary

of the maximum positive and negative load. Considering the linearised model at each position, if we set the step Force equal to the max positive load, which is around 2400N, the amplitude of the response could therefore reach 200mm, and the value would be even greater in the nonlinear system due to the softening effect in the compression phase. The range of the responsive wheel travel is sufficient to handle most terrain for a normal passenger car. The magnitude of the negative step force can be larger than the positive one due to the hardening effect in the rebound phase, which makes the system stiffer against the shock, and consequently, the amplitude of response would be smaller than in the linear system.

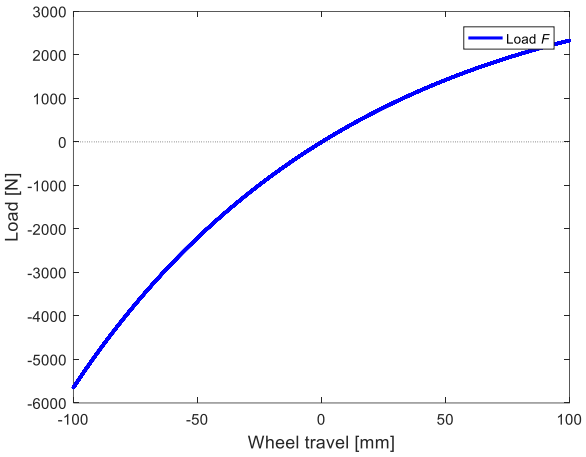

Figure 8.3 – The range of load F from -100mm to 100mm wheel travel.

8.1 Linear step response of the structure

Having explored the general response of a simple spring-mass system to a step response, let us now move on to analyse the step response of our nonlinear structure. Starting with a simpler point to illustrate the problem, we will now consider the equivalent linear structure at the original position first. The equivalent mass and the equivalent stiffness of the system were already evaluated in section 7.2, with values m_{eq}=8.2205kg and k_{eq}=360000N/m, respectively. It's possible to illustrate response of the displacement h of our specific structure to the step response in the time domain by substituting the mass and stiffness into the equation of the general solution, as in eq. (8.2). Suppose the step force is F_0=2400N, and the historical trajectory of the wheel motion $h(t)$ can be analytically given by eq. (8.1.2).

$$\omega_n = \sqrt{\frac{k_{eq}}{m_{eq}}} = 66.176\text{rad/s} \tag{8.1.1}$$

$$h(t) = \frac{1}{15}\left(1-\cos\left(66.176t\right)\right) \tag{8.1.2}$$

To illustrate the special property of our structure in the future, it's useful to compare the responses between the linearised and nonlinear system. By doing so, we can better understand the performance of such a novel suspension. However, given the highly nonlinear characteristic of our system, obtaining the analytical solution for the displacement response to a step force from its EOM is challenging. This is because the mass and stiffness are deeply coupled with the motion in the nonlinear system. Nevertheless, it's possible to estimate the response by modelling the system in Simulink, which provides a numerical solution. The linear system can be modelled as shown in

Figure 8.1.1, where the initial state is zero. Once the excitation of the system is determined, the response of the motion can be evaluated according to the EOM of the linear system.

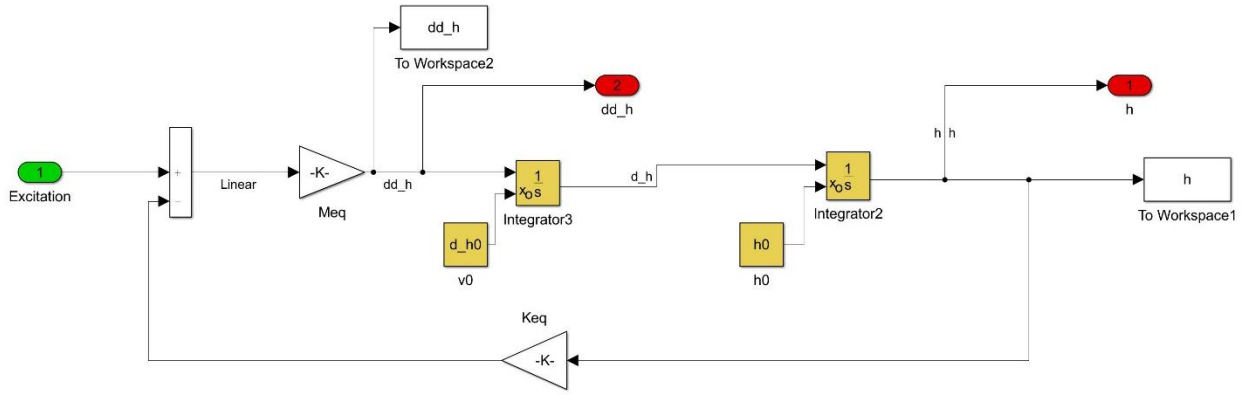

Figure 8.1.1 – Simulink model of the linear system in original system.

To demonstrate the consistency between the analytical solution and numerical solution of the system, we apply the same step input F_0=2400N to the model as before and save both the trajectory of displacement h from Simulink and the analytical solution in the same plot. The two curves superimposed together, as shown in Figure 8.1.2, indicating that the Simulink model of the linear model faithfully represents the performance of the linear system.

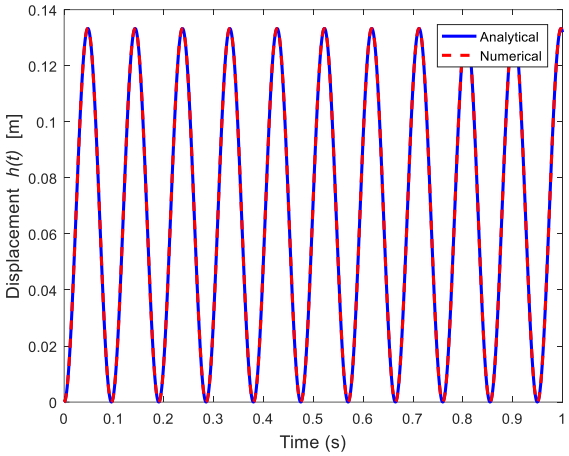

Figure 8.1.2 – Comparison between the analytical and numerical solutions of the response.

8.2 Nonlinear step response of the structure

As previously discussed, the particular EOM of our proposed system and the nonlinear characteristics of the structure are ultimately described by three nonlinear functions $f_1(h)$, $f_2(h)$, $f_3(h)$, as shown in eq. (8.2.1). These nonlinear functions are related to the motion of the structure, which means that the response of the nonlinear system is coupled to the displacement of the structure. Therefore, the performance of the system is customised by the magnitude of the excitation force and the initial condition. Although the general solution of the linear system cannot be adapted directly, the response of the nonlinear system can still be solved numerically. Fortunately, the

nonlinear system can also be modelled in Simulink using the nonlinear EOM of the system as evaluated before, avoiding tremendous manual calculation work. The nonlinear Simulink model is shown in Figure 8.2.1.

$$mf_1(h)\ddot{h} + mf_2(h)\dot{h}^2 + k_{s1}h + k_{s2}f_3(h) = F \tag{8.2.1}$$

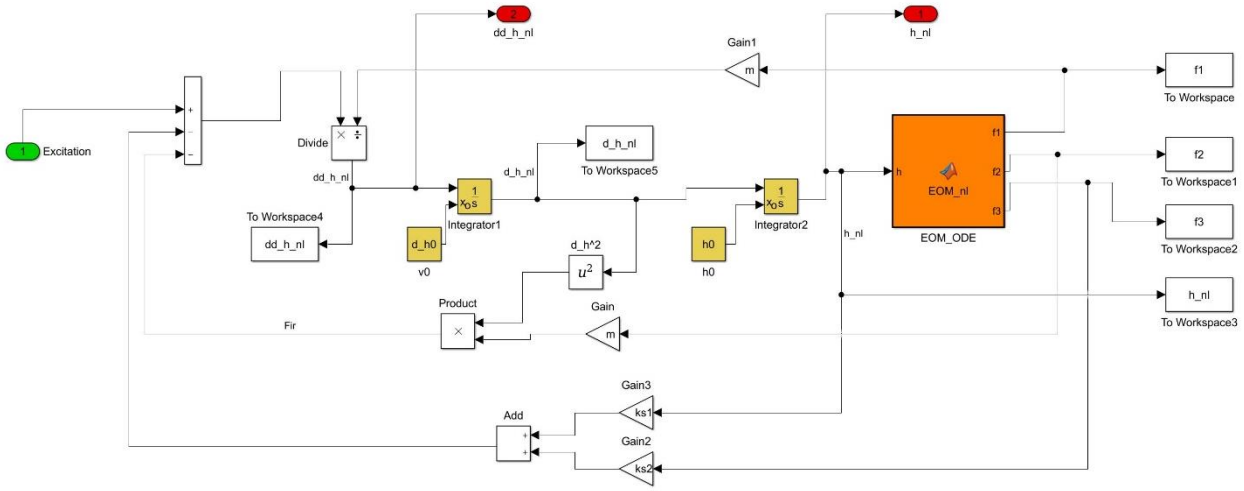

Figure 8.2.1 – Simulink model of the nonlinear system.

Where the code of the MATLAB function **EOM_nl** which contains three nonlinear factors and describes the nonlinearity of the system can be checked in Appendix F.

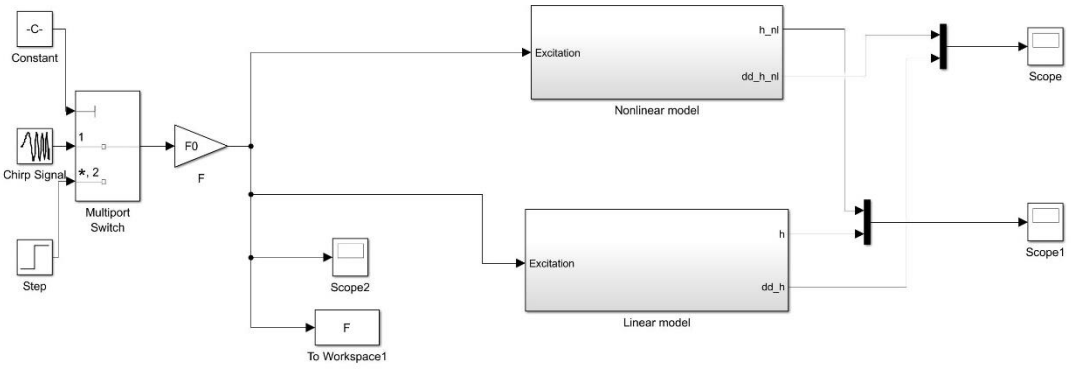

Figure 8.2.2 – Comparison between the linearised and nonlinear system in Simulink.

Now, the nonlinear response of the system to the step input can be illustrated. By comparing with the linear response, some characteristics of the nonlinear system can be reasonably interpreted. Since the properties of the nonlinear system are coupled with the magnitude of the displacement h, we consider serval different magnitudes of the step force F_0 to analyse the influence of the force magnitude on the nonlinear response.

The excitation forces are in the range of [-5000N, 2400N] according to Figure 8.2, where the max positive force is about 2400N, and the max negative force equals to -4400N. The selected step

forces are scaled appropriately to demonstrate the step response with different degrees of impact under the entire wheel travel range. The magnitude of the negative force is larger because the hardening effect in the rebound phase allows the structure to withstand more load, leading to a server bounce in the extension phase. The positive force can represent an instantaneous shock to the suspension, e.g., a bump in the road is encountered, while a negative force may indicate the vehicle riding over a pothole.

8.2.1 Positive step response

We will evaluate the jounce performance of the nonlinear system in the first place, as shown in the following figures. Three positive step excitations (400N, 1400N and 2400N) are evaluated. In each displacement response plot, the black dashed line represents the limit of the displacement when adopting the equivalent softest stiffness in the upper boundary position in the system as discussed in section 7.2. In three pairs of plots, the frequency of the linear response remains constant for the constant mass and stiffness in the system. While the frequency of the nonlinear response is obviously different from the linear one. As the magnitude of the step force increases, the decrease in response frequency becomes more and more pronounced, also the amplitude of the response approaches the reference softest condition more closely. This suggests that as the maximum amplitude of the displacement increases, the natural frequency gradually decreases, in line with the softening tendency of the natural frequency plot discussed earlier. With the softening effect, the shock is alleviated, as evident in the acceleration plot. Compared to the linear system, the maximum reactive acceleration is reduced, and the effect is more salient with larger step force. The discrepancy in the max acceleration between two system increases obviously from small to larger impact. Hence, the ride comfort of the vehicle can be improved with our novel structure, particularly under sever conditions, compared to the ordinary linear system. Nevertheless, the softening effect is achieved by sacrificing the displacement of the wheel, and the discrepancy of displacement increases gradually, which means enough space between the tyre and the wheel arch of the vehicle should be ensured if using the novel suspension.

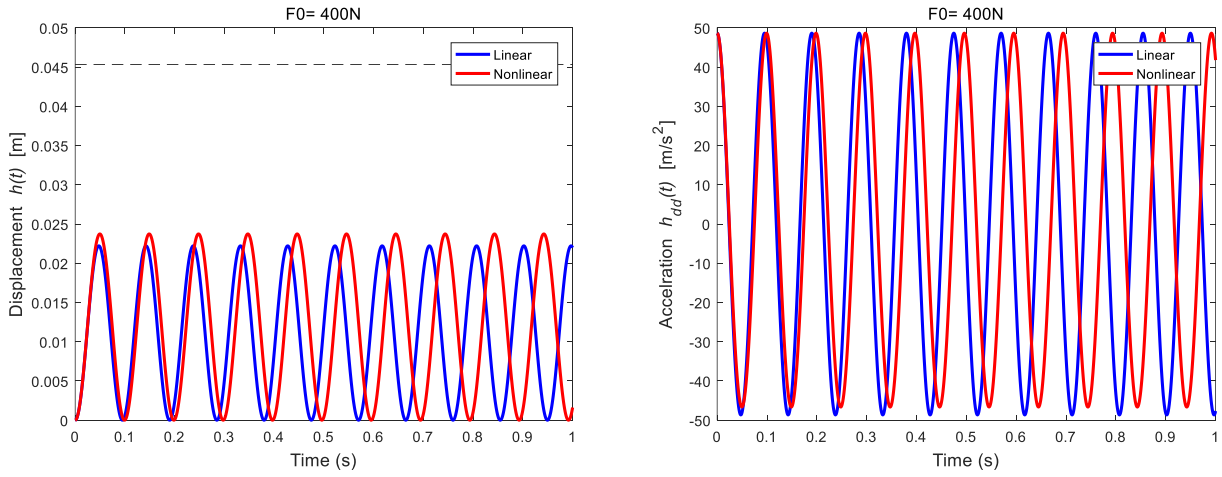

Figure 8.2.1.1 – Displacement and acceleration response of two system when F_0=400N.

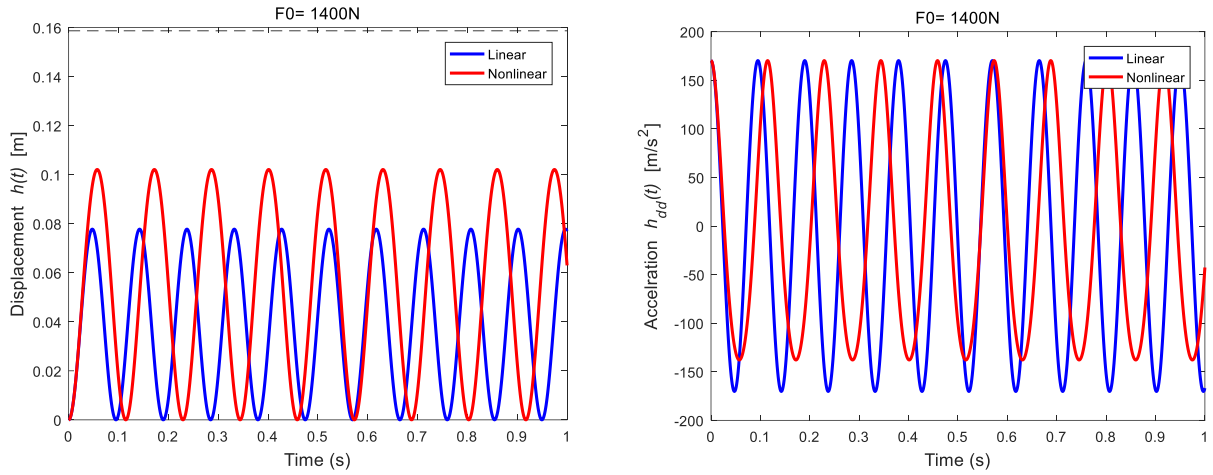

Figure 8.2.1.2 – Displacement and acceleration response of two system when F_0=1400N.

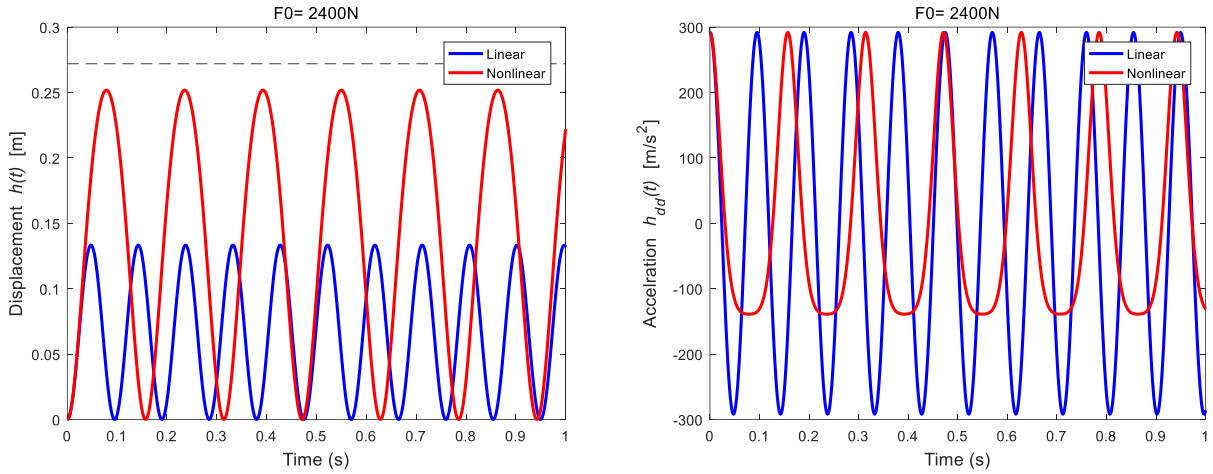

Figure 8.2.1.3 – Displacement and acceleration response of two system when F_0=2400N.

8.2.2 Negative step response

Continuing our analysis, let's now examine the rebound performance, illustrated from Figure 8.2.2.1 to Figure 8.2.2.3. Three negative step forces (-400N, -2400N and -4400N) are considered. Where the black dashed line in each displacement response represents the boundary amplitude of the displacement if we adopt the equivalent hardest stiffness of the lower boundary position in the system, as discussed in the linearised system in section 7.2. In contrast to the jounce performance of the structure, the response of system in rebound phase is also influenced by the magnitude of the displacement but shows a contrasting behaviour that benefits the stability of the structure. In the rebound phase, the main task is shifts from shock absorption to stabilize the vehicle instead. As increasing the excitation magnitude, the displacement and the natural frequency gradually increases, corresponding to the hardening tendency in the extension phase, as mentioned before. Due to the hardening effect, the motion is much shortened compared to the linear system, and the amplitude gets closer to the dashed line. The recovery acceleration is larger, which means that the wheel is pulled back to the initial position faster than in the linear system. This demonstrates the structure's capability to efficiently recover and stabilize the vehicle during the rebound phase.

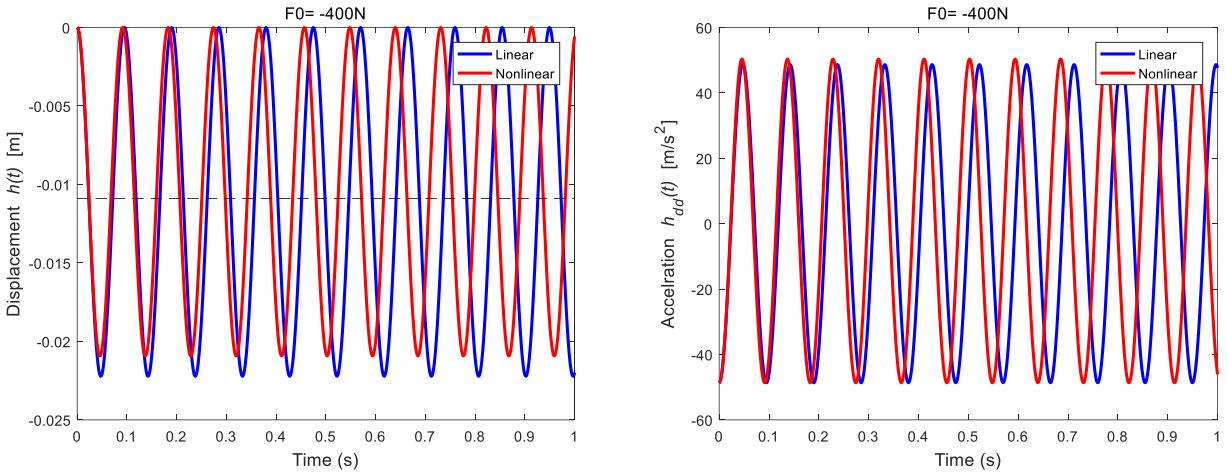

Figure 8.2.2.1 – Displacement and acceleration response of two system when F_0=-400N.

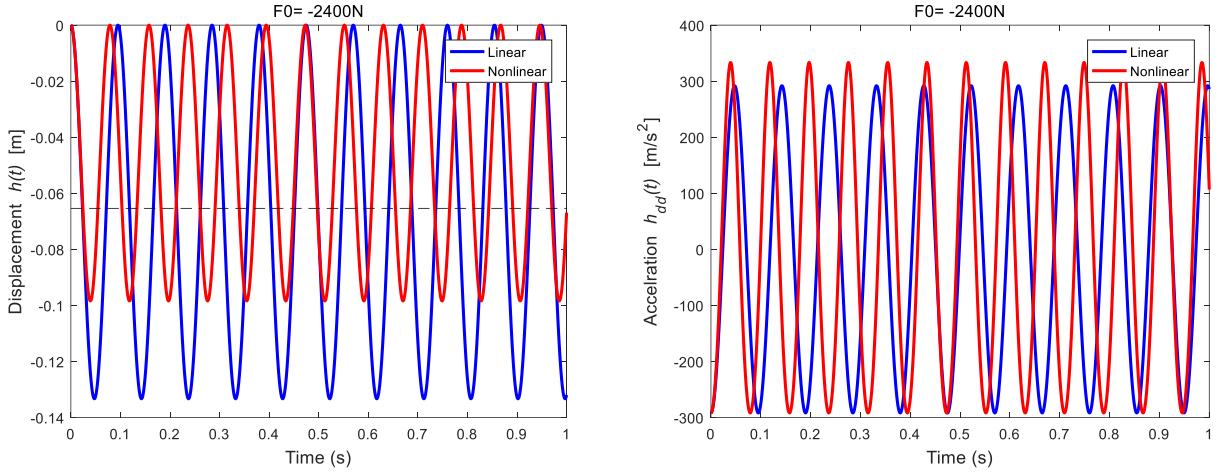

Figure 8.2.2.2 – Displacement and acceleration response of two system when F_0=-2400N.

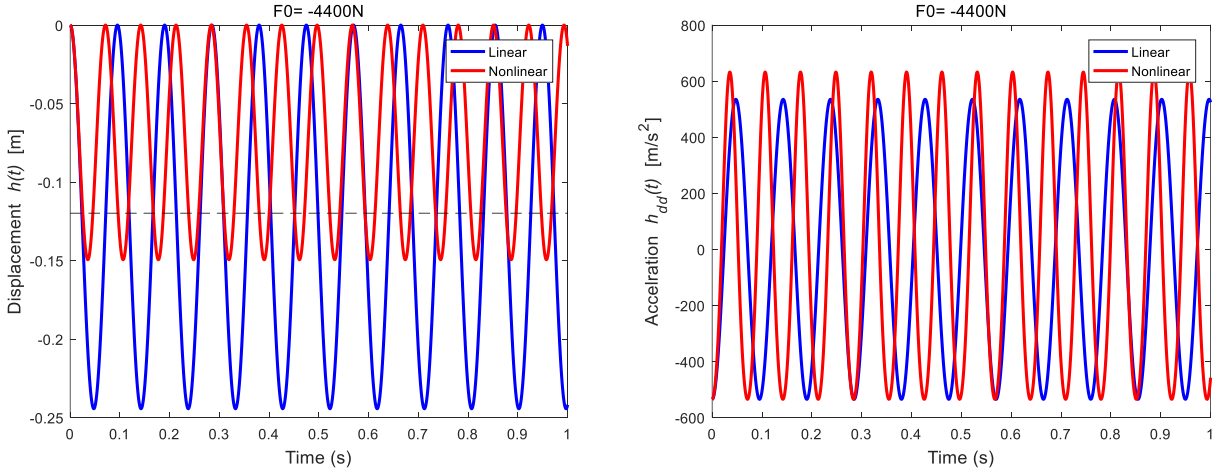

Figure 8.2.2.3 – Displacement and acceleration response of two system when F_0=-4400N.

Indeed, the hardening effect observed in the rebound phase plays a crucial role in enhancing the handling performance of the vehicle. The higher extension stiffness results in a greater recovery force from the loaded position. This is advantageous in preventing the suspension from fully

extending over large slopes, helping maintain tire contact with the road. Additionally, it facilitates the quick return of the wheel to the rest position. This feature can effectively compensate for the pitch motion of the vehicle, particularly when braking or accelerating, which is influenced by the softening effect observed in the jounce phase. The combined impact of softening in jounce and hardening in rebound contributes to an overall improved dynamic response of the vehicle suspension.

8.3 Effectiveness of the three nonlinear functions

The step response of our proposed system revealed a highly nonlinear behaviour in section 8.2 In contrast to the linear system, the response curve is severely distorted, and the time history displacement no longer follows a sinusoidal shape, indicating the significant impact of the system's nonlinearity during a severe impact. The relations of three nonlinear forces in the system with different step inputs are depicted in Figure 8.3.1 and Figure 8.3.2.

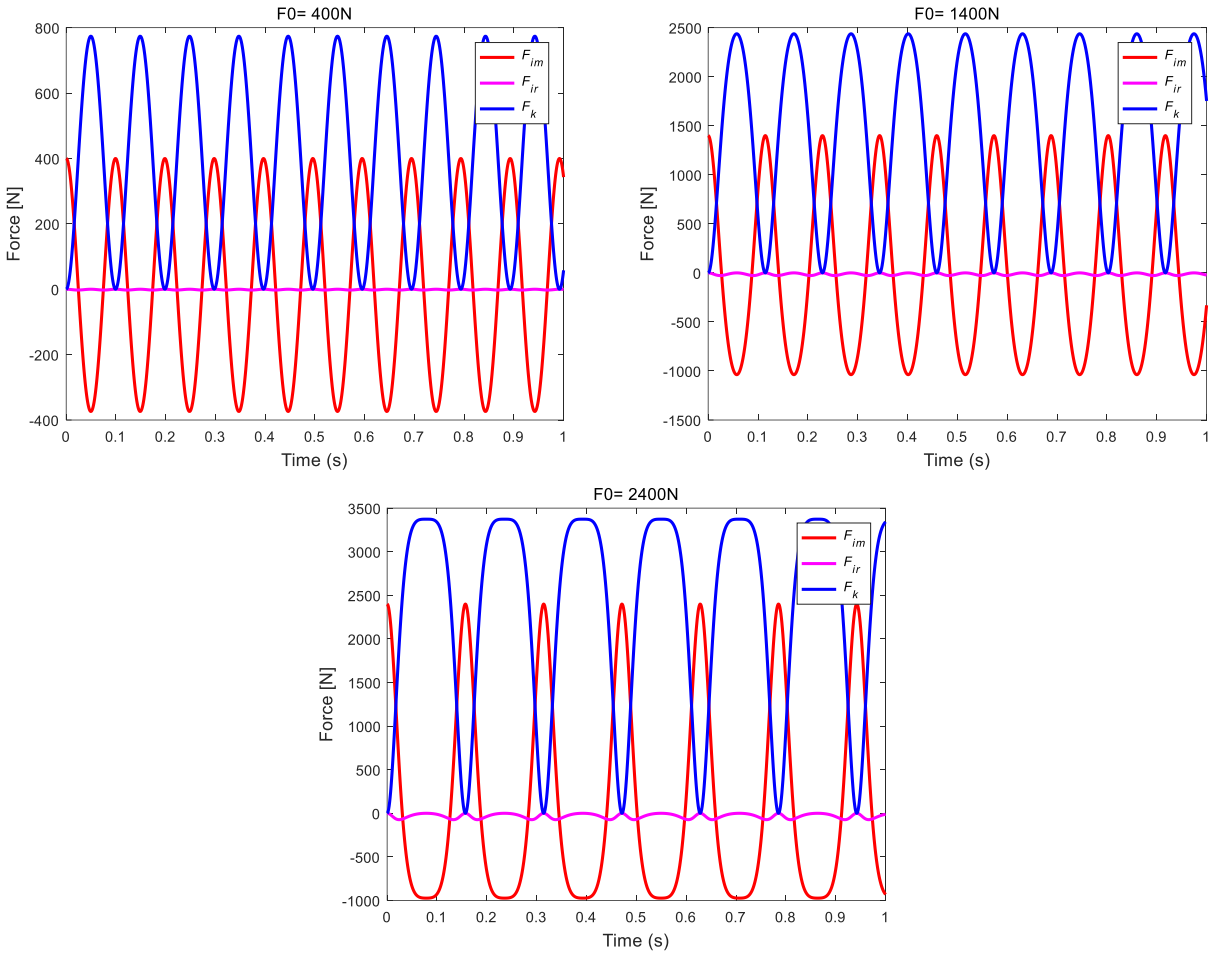

Figure 8.3.1 – Three nonlinear forces in the system with three different positive excitations.

In Figure 8.3.1, with positive step excitations, the stiffness force F_k is always positive. The inertial force incurred by the translational motion F_{im} oscillates within a certain a range with the same frequency as the stiffness force. While the frequency of inertia force incurred by the rotational unit F_{ir} is twice as high as the other two forces, given its relation to the square of the velocity. The force F_{ir} is always negative and maintains a relatively small magnitude compared to the other two forces. Throughout the range from the initial position to the upper boundary, the force F_{ir} helps alleviate

the bounce of the shock. In the return phase it promotes the restoration of the structure, contributing to the stability of the system. With increasing the magnitude of the excitation, the effect of nonlinear characteristic of the system becomes more and more apparent but still with a relatively small effect.

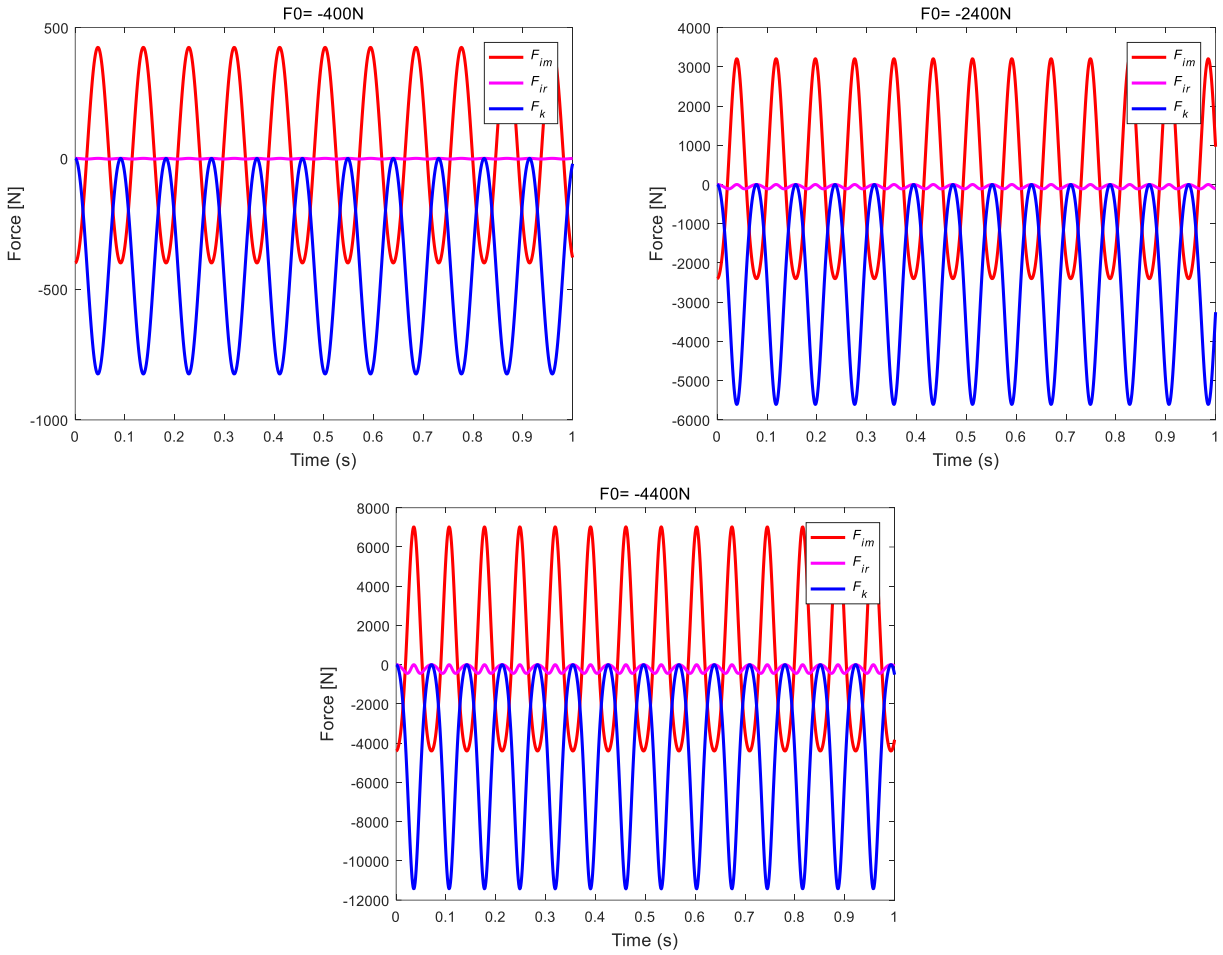

Figure 8.3.2 – Three nonlinear forces in the system with three different negative excitations.

By analysing Figure 8.3.2 with negative step excitations, the stiffness force F_k becomes negative. The inertia force F_{im} also oscillates relevantly with the stiffness force, sharing the same frequency. Similar to the case with positive step excitations, the frequency of the inertia force F_{ir} is twice that of the other two forces, maintaining negative sign. Due to the hardening effect other than softening in the extension phase, the force F_{ir} plays a role in propelling the system to the boundary position from the initial position, facilitating a faster reach to the limit and enhancing stability. In the recovery phase, it helps reduce the bounce of system caused by the hardening effect, resulting in a mitigated severe reactive acceleration.. With a larger excitation force, the effect of the force F_{ir} becomes more apparent, but still constitutes a relatively small part of the overall system.

In the analysis of the nonlinear characteristic of the system, three key nonlinear functions, namely $f_1(h)$, $f_2(h)$, and $f_3(h)$, correspond to the force F_{im}, force F_{ir} and force F_k respectively. To gain a deeper understanding of the nonlinear characteristic of the system, it's necessary to evaluate the effectiveness of each nonlinear function that contributes to its distinctive features. Derived from the step response we conducted before, the response shape of each nonlinear function in the time domain with different step inputs can be visualised from Figure 8.3.3 to Figure 8.3.8. These figures provide a clear comparison and evaluation of the influence of each nonlinear function on the overall softening or hardening performance of the system.

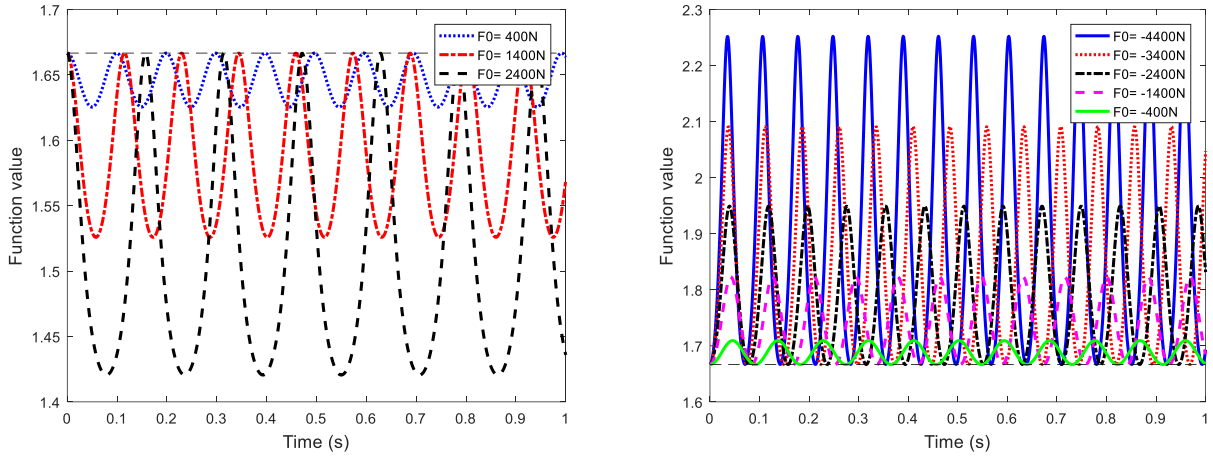

Figure 8.3.3 – Values of $f_1(h)$ with positive step forces (left) and negative step force (right).

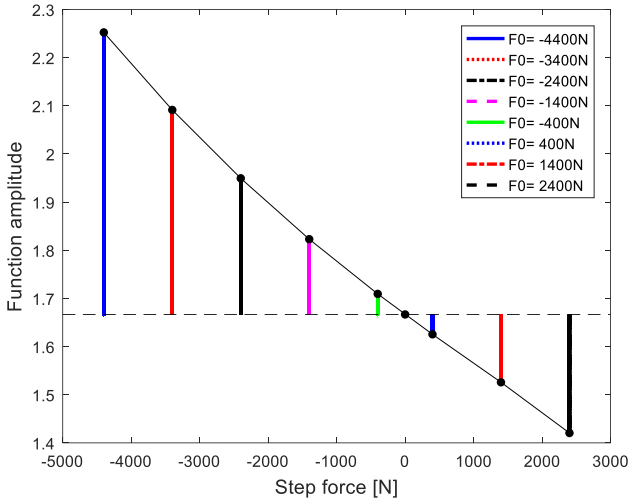

Figure 8.3.4 – Amplitudes of nonlinear function $f_1(h)$ with different step forces.

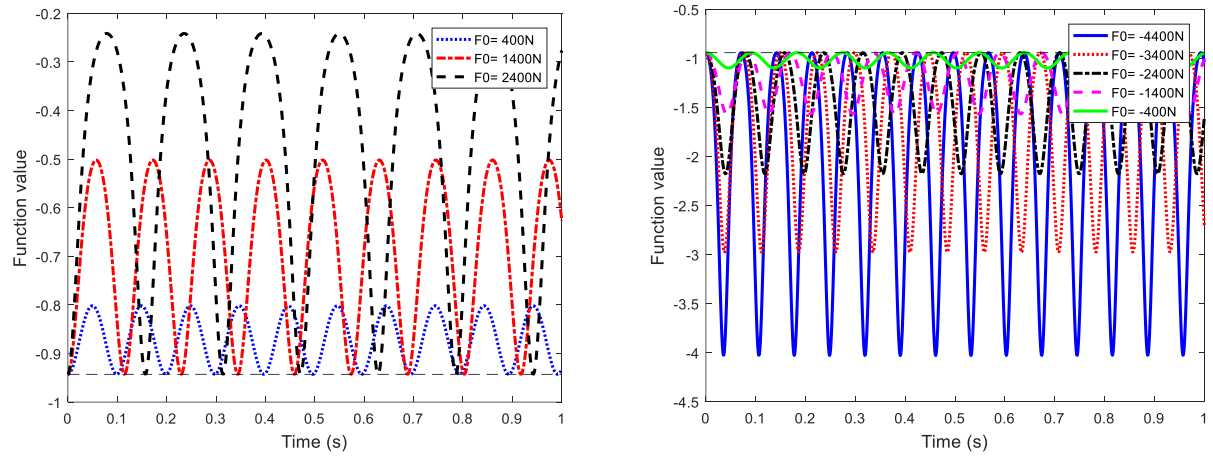

Figure 8.3.5 – Values of $f_2(h)$ with positive step forces (left) and negative step force (right).

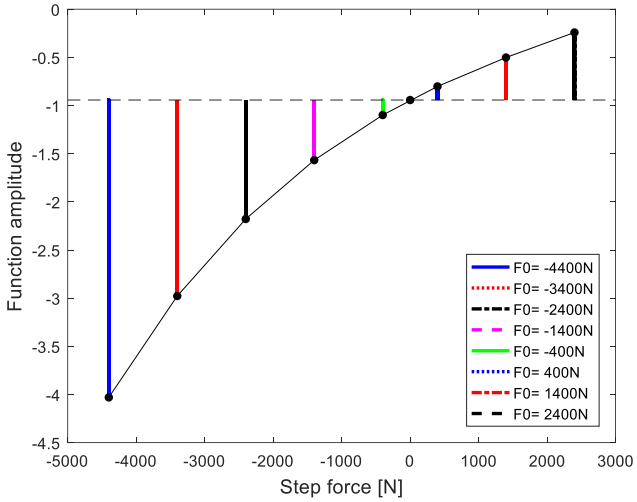

Figure 8.3.6 – Amplitudes of nonlinear function $f_2(h)$ with different step forces.

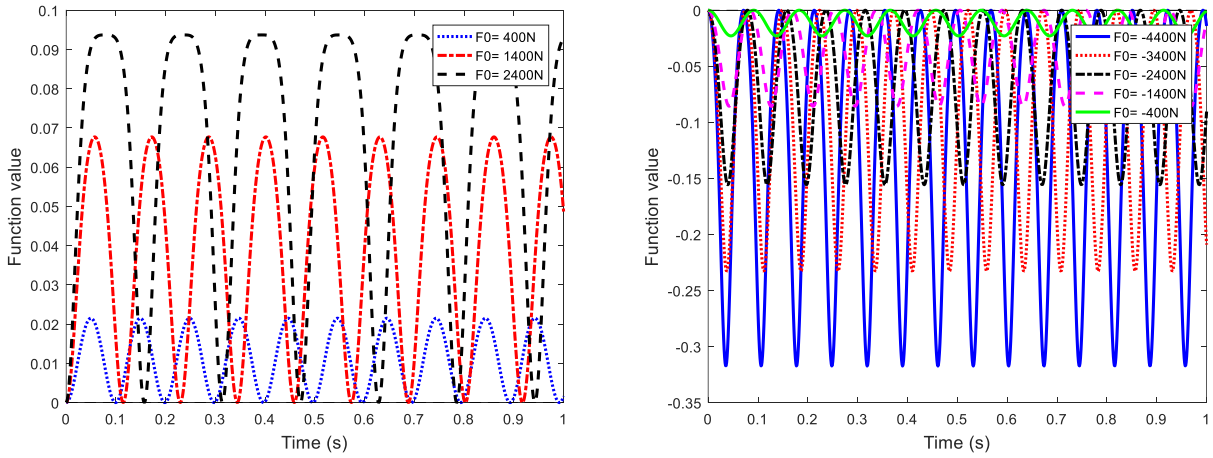

Figure 8.3.7 – Values of $f_3(h)$ with positive step forces (left) and negative step force (right).

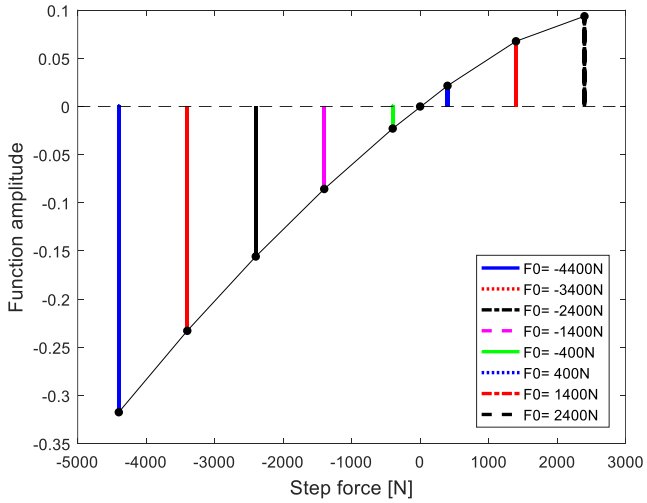

Figure 8.3.8 – Amplitudes of nonlinear function $f_3(h)$ with different step forces.

Focusing first on the softening effectiveness of each nonlinear function, as we talked in section 8.2, the softening effect becomes more evident with larger external excitation, leading to a smoothed reactive acceleration response and ensuring the ride comfort of the vehicle. Analysing the shapes of each nonlinear function under positive excitation condition, it is observed that, with increasing the excitation, the amplitudes of the three functions increase while their frequencies decrease, suggesting that they all contribute to the softening effect of the whole system. Nevertheless, the shape of f_3 (corresponding to the nonlinear stiffness force exhibits more pronounced deformation compared to the other two. Its amplitude change is more nonlinear as depicted in Figure 8.3.8, emphasizing the dominance of nonlinearity caused by the nonlinear stiffness force in the compression phase.

Moving to the negative step response of the system, a similar pattern emerges where greater excitation leads to more obvious nonlinearity. All the three amplitudes increase, and the three frequencies decreased, indicating a hardening effect in the rebound phase. Compared to the positive excitation, the amplitudes of the three functions all have larger values in the extension phase, demonstrating that all three nonlinear functions contribute to the hardening effect of the whole system. The changes in the shapes of three functions are quite similar, showcasing a strong hardening effect from every nonlinear part of the system. Notably, the inertia force F_{im} and stiffness force F_k have relevant shapes and larger magnitudes compared to the force F_{ir} as shown in Figure 8.3.2. Hence, we can anticipate a stronger hardening effect due to the two forces.

In conclusion, the nonlinear function f_3 (associated with the nonlinear stiffness force) consistently plays the most significant role in the system, whether in the jounce or rebound phase. The nonlinear functions f_1 contribute to the nonlinearity the system in the extension phase, which is comparable to f_3. On the other hand, the nonlinearity incurred by the rotational unit, represented by the nonlinear function f_2, is expected to benefit the dynamical performance of the system to some extent, although its influence is relatively small compared to f_1 and f_3.

8.4 Hilbert transform

With reference to the approach that has been developed to by Bonisoli E. et al. [32], the unforced behaviour of our undamped nonlinear dynamical single degree of freedom (SDOF) system can be expressed in the form:

$$m(h)\ddot{h}(t)+k(h)h(t)=0 \tag{8.4.1}$$

Where the equation seems link an ODE but in which the equivalent mass $m(h)$ and nonlinear stiffness coefficient $k(h)$ depend on the displacement h and the damping terms are absent for us undamped system. The linear canonical form of the equation can be written as follow:

$$\ddot{h}(t)+\omega_n^{\,2}(t)h(t)=0 \tag{8.4.2}$$

Where the natural frequency $\omega_n(t)$ are time dependent. By considering the definition of the complex analytic signal of $h(t)$, expressed in exponential form, it holds:

$$H(t)=h(t)+\mathrm{i}\,\tilde{h}(t)=A(t)e^{\mathrm{i}\Psi(t)} \tag{8.4.3}$$

Where $\tilde{h}(t)$ is the Hibert transform of the real signal $h(t)$. The real envelop function $A(t)$ and the real instantaneous phase function $\Psi(t)$, which are both time-dependent, result in respectively:

$$A(t)=\sqrt{h(t)^2+\tilde{h}(t)^2} \tag{8.4.4}$$

$$\Psi(t)=\tan^{-1}\frac{\tilde{h}(t)}{h(t)} \tag{8.4.5}$$

Where $\omega(t)=\dot{\Psi}(t)$ is the instantaneous angular frequency. Hence the time-dependent natural frequency $\omega_n(t)$ function is related to the envelope and phase function which is given by:

$$\omega_n(t)=\sqrt{\omega^2+\frac{\dot{A}\dot{\omega}}{A\omega}+2\frac{\dot{A}^2}{A^2}-\frac{\ddot{A}}{A}} \tag{8.4.6}$$

To delve into the nonlinear performance of the system, the Hilbert transform is applied for the analysis of the response signal from tests. This enables the evaluation of the instantaneous natural frequency of the system, providing insights into the system's nonlinearity. In the post-processing of the response signal using the Hibert transform, it's crucial to select an acquisition range in the middle of the tested time domain. This ensures stability in frequency evaluation, since the estimation at the beginning and at the end of the estimation is unbounded, as shown in Figure 8.4.1. If we encounter the two boundary bands, the accuracy of the frequency evaluation will be distorted critically. The chosen cut-off range spans from 0 to 25% at the beginning and from 75% to the end of the domain in our analysis, and the results show a reasonable behaviour, free from the influence of harmonics, as depicted in the plots of instantaneous frequency shown in Figure 8.4.2 and Figure 8.4.3.

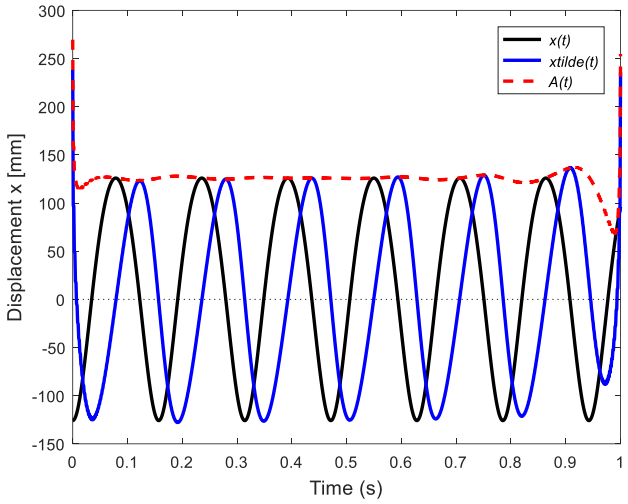

Figure 8.4.1 – Hilbert transform of the output signal with 2400N excitation force.

The numerical solution obtained through the Simulink model remains unaffected by environmental factors, instruments, and measurement errors, eliminating the presence of chaotic signals in the response. However, for experimental verification of the system, it becomes essential to consider a digital filter in the post-processing phase, which helps eliminate the influence of high-frequency harmonics induced by external sources. The instantaneous natural frequency of the undamped system with different positive and negative excitations is depicted in Figure 8.4.2 and Figure 8.4.3, correspondingly.

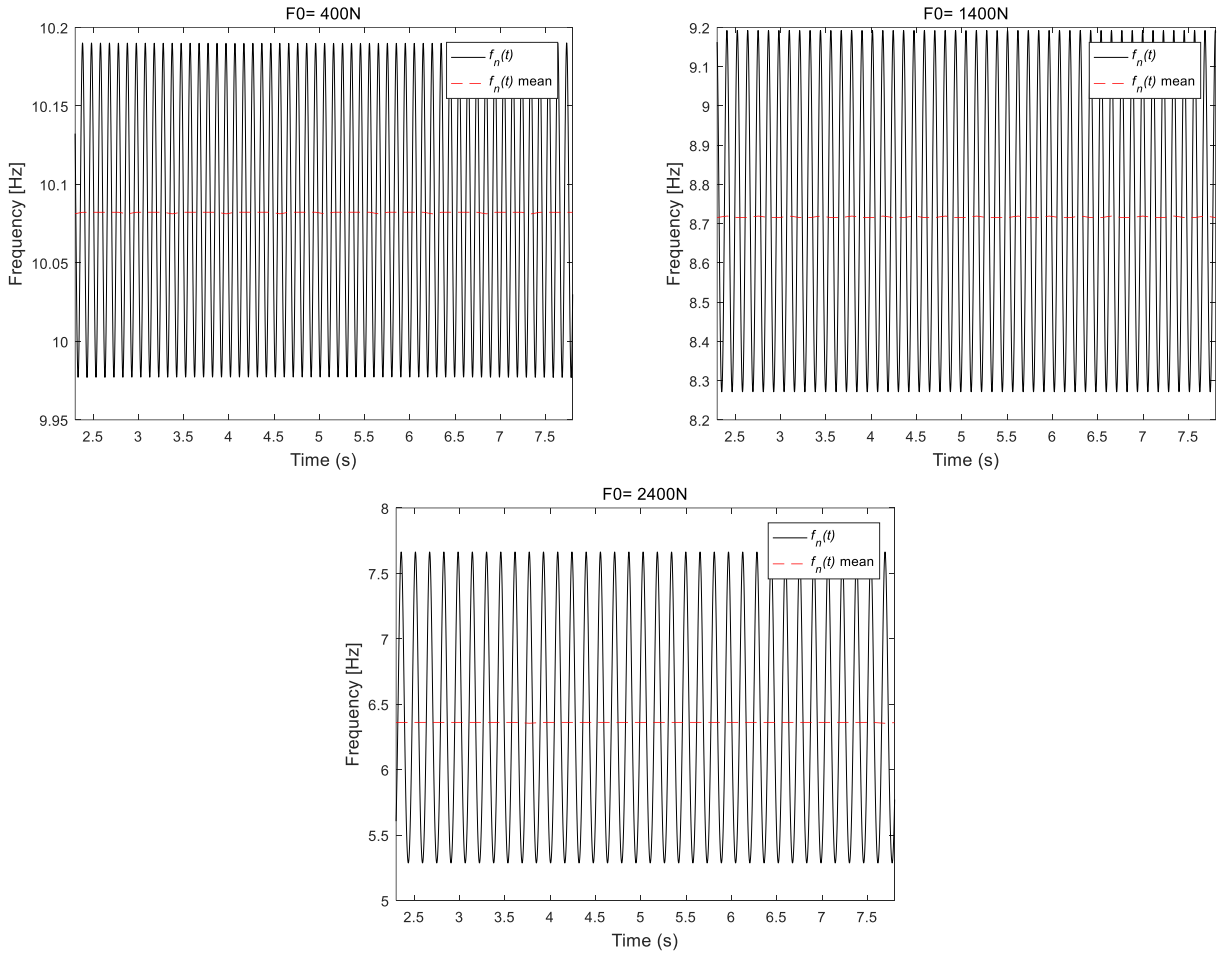

Figure 8.4.2 – Instantaneous natural frequency of the nonlinear system with positive excitations.

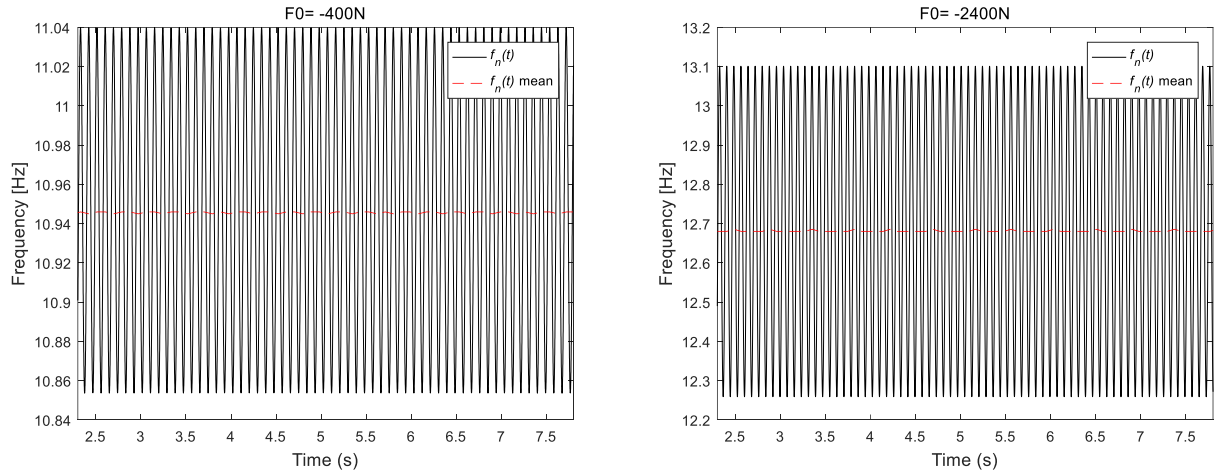

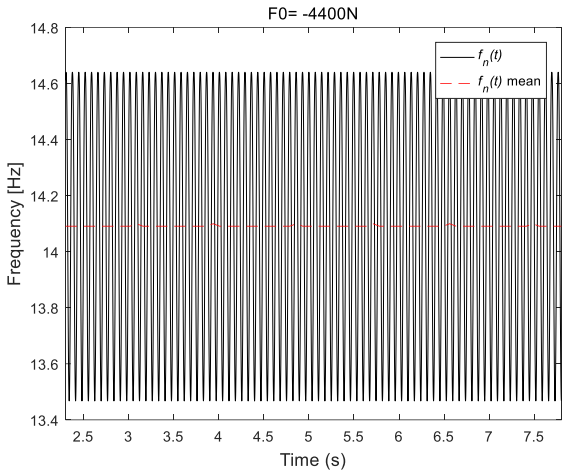

Figure 8.4.3 – Instantaneous natural frequency of the nonlinear system with negative excitations.

The figures illustrate an oscillatory phenomenon where the instantaneous natural frequency oscillates around a mean frequency This oscillation is attributed to the variable natural frequency of the nonlinear system, influenced by the displacement of the perch, as discussed in the preceding sections. The mean frequency is the natural frequency of the nonlinear system that equivalently behaves to the external environment. For the linearised system at the initial position, the neutral frequency is about 10.53Hz. By analysing the instantaneous frequency trends in the two figures above, it allows us to identify the softening and hardening behaviour induced by the nonlinearities inherent in the special quadrilateral structure: the softening effect occurs with a positive excitation, where the mean frequency is lower than the reference initial value and varies in the range [6.4Hz 10.53Hz] as shown in Figure 8.4.1, with different magnitude of inputs; while in the opposite case, the response is hardened in the rebound phase, where the mean frequency is in the range [10.53Hz 14.15Hz] as illustrated by Figure 8.4.2, with different input magnitudes.

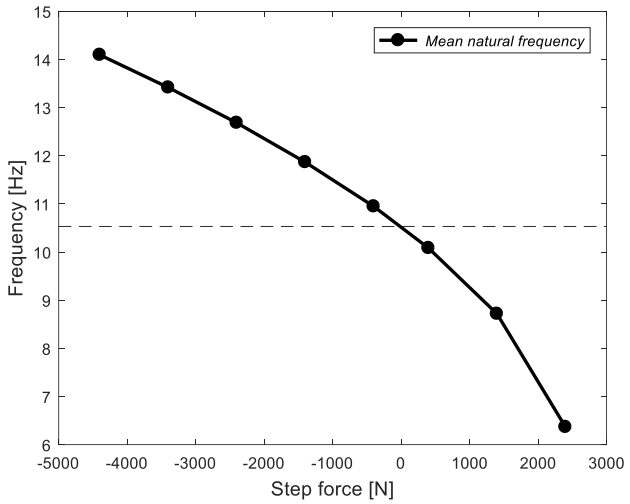

Figure 8.4.4 – Mean natural frequency of the nonlinear system vs. step excitations.

To better illustrate the frequency characteristics of the nonlinear system under a step excitation condition, the corresponding mean natural frequencies of the response with different excitations are plotted in Figure 8.4.4. From which we can tell that the system prone to be softened and more resistant to be hardened, as the frequency decrease dramatically with a positive excitation and the increasing tendency is less pronounced compared to the softening effect with a negative step input.

8.5 Considering the dissipation effect

The effects of components such as rolling bearings, hyperelastic springs/beams, non-holonomic constraints, play and hysteresis mechanisms, and friction are typically disregarded due to their minimal impact on the overall behaviour of the system at a macroscopic level. Predicting the specific influence of these factors in the analytical analysis process proves challenging. However, during experimental verification of our obtained simulation results, it becomes essential to account for energy dissipation within the system, as damping terms inherently exist in the instrumentation. To address this, we will refine the model by incorporating a damping term into the EOM, resulting in a revised expression for the equation, which is given by:

$$m(h)\ddot{h}(t)+c(t)\dot{h}(t)+k(h)h(t)=0 \tag{8.5.1}$$

Where the nonlinear damping coefficient $c(t)$ is related to the velocity, and we assume that the damping coefficient is proportional to the nonlinear function $f_1(h)$ (corresponding to the equivalent mass). The proportional coefficient is denoted by the constant c.

$$c(t)=cf_1(h) \tag{8.5.2}$$

The linear canonical form of the equation of motion is expressed as follow:

$$\ddot{h}(t)+2\zeta(t)\omega_n(t)\dot{h}(t)+\omega_n^2(t)h(t)=0 \tag{8.5.3}$$

Where the natural frequency $\omega_n(t)$ is dependent on the time. Similar to the Hilbert transform used in section 8.4, the complex analytic signal of $h(t)$, expressed in exponential form, holds:

$$H(t)=h(t)+\mathrm{i}\,\tilde{h}(t)=A(t)e^{\mathrm{i}\Psi(t)} \tag{8.5.4}$$

Where $\tilde{h}(t)$ is the Hibert transform of the real signal $h(t)$. The real envelop function $A(t)$ and the real instantaneous phase function $\Psi(t)$, both of which are time-dependent, are given by:

$$A(t)=\sqrt{h(t)^2+\tilde{h}(t)^2} \tag{8.5.5}$$

$$\Psi(t)=\tan^{-1}\frac{\tilde{h}(t)}{h(t)} \tag{8.5.6}$$

Where $\omega(t)=\dot{\Psi}(t)$ is the instantaneous angular frequency. Hence the time-dependent damping $\zeta(t)$ and natural frequency $\omega_n(t)$ functions are related to the envelope and phase function through the relations:

$$\zeta(t)=-\frac{1}{\omega_n}\left(\frac{\dot{A}}{A}+\frac{\dot{\omega}}{2\omega}\right) \tag{8.5.7}$$

$$\omega_n(t)=\sqrt{\omega^2+\frac{\dot{A}\dot{\omega}}{A\omega}+2\frac{\dot{A}^2}{A^2}-\frac{\ddot{A}}{A}} \tag{8.5.8}$$

If we initially set the coefficient c to 0.2, which should be specifically considered when calibrating the data, and perform a test similar to that as in section 8.4, the instantaneous natural frequency of the system, accounting for energy dissipation with different positive or negative step excitation forces, is shown in Figure 8.5.1 and Figure 8.5.2, respectively.

When considering energy dissipation in the system, the performance of the system deviates slightly from that of the undamped system. With positive excitations, the damping effect resists the motion of the system as shown in Figure 8.5.1, the instantaneous frequency of the nonlinear system gradually contract towards to the mean natural frequency. The effect becomes more pronounced as the excitation increases. The damping force dissipates the energy of the motion, leading to a progressive decrease in displacement amplitude and a mitigation of the system's softening effect.

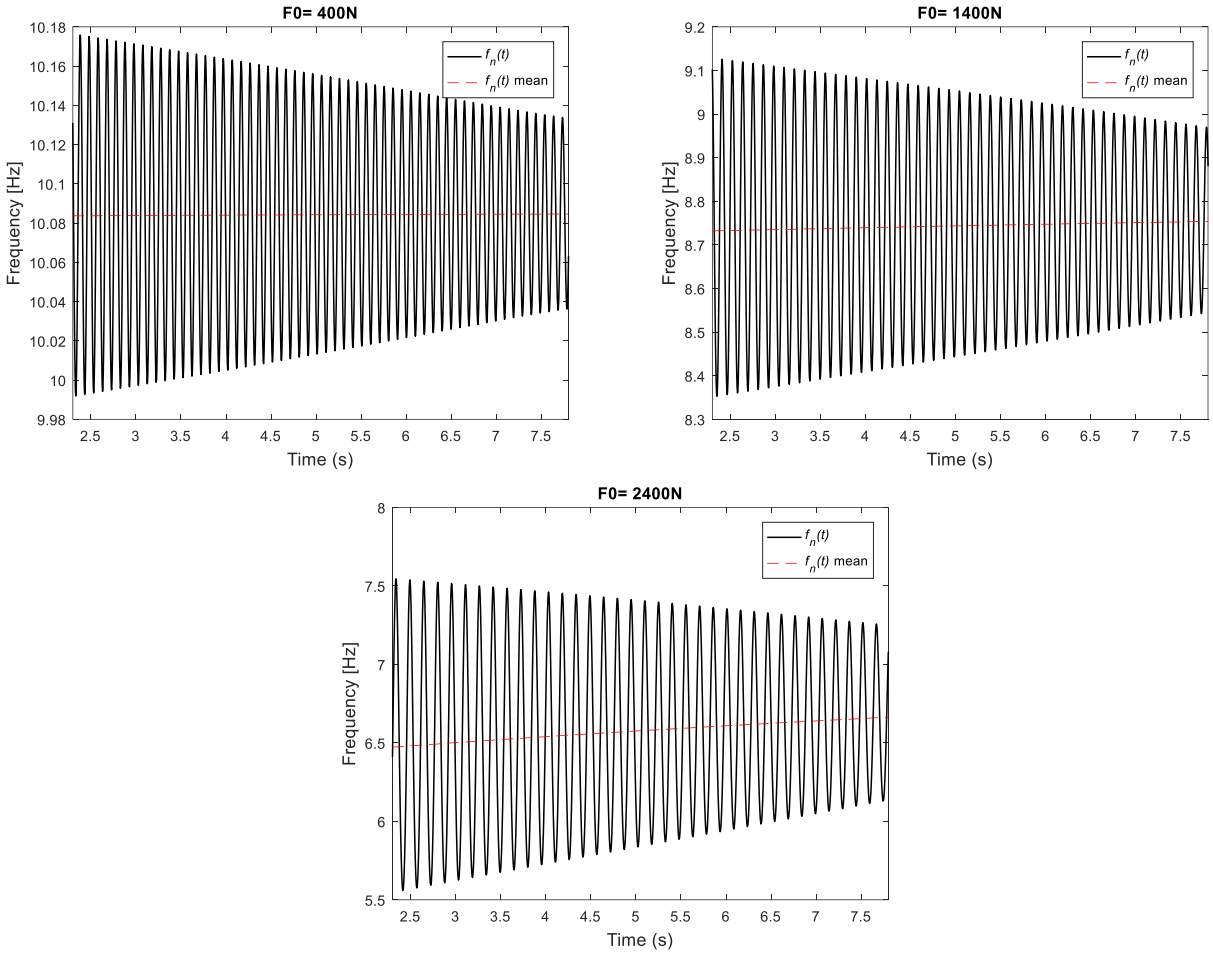

Figure 8.5.1 – Instantaneous natural frequency of the nonlinear system with negative excitations.

On the contrary, in a negative step response test, the damping effect with resist the downward motion of the system as shown in Figure 8.5.2. The instantaneous frequency of the nonlinear system also contracts towards the mean natural frequency, and this effect becomes more evident with increasing excitation. The reason for the shrinkage of the natural frequency is because the damping force dissipates the energy in the system, the amplitude of the displacement progressively decreases in the response process. The system tends to oscillate around a static position, leading to a smaller range of displacement and a tighter range of instantaneous frequencies.

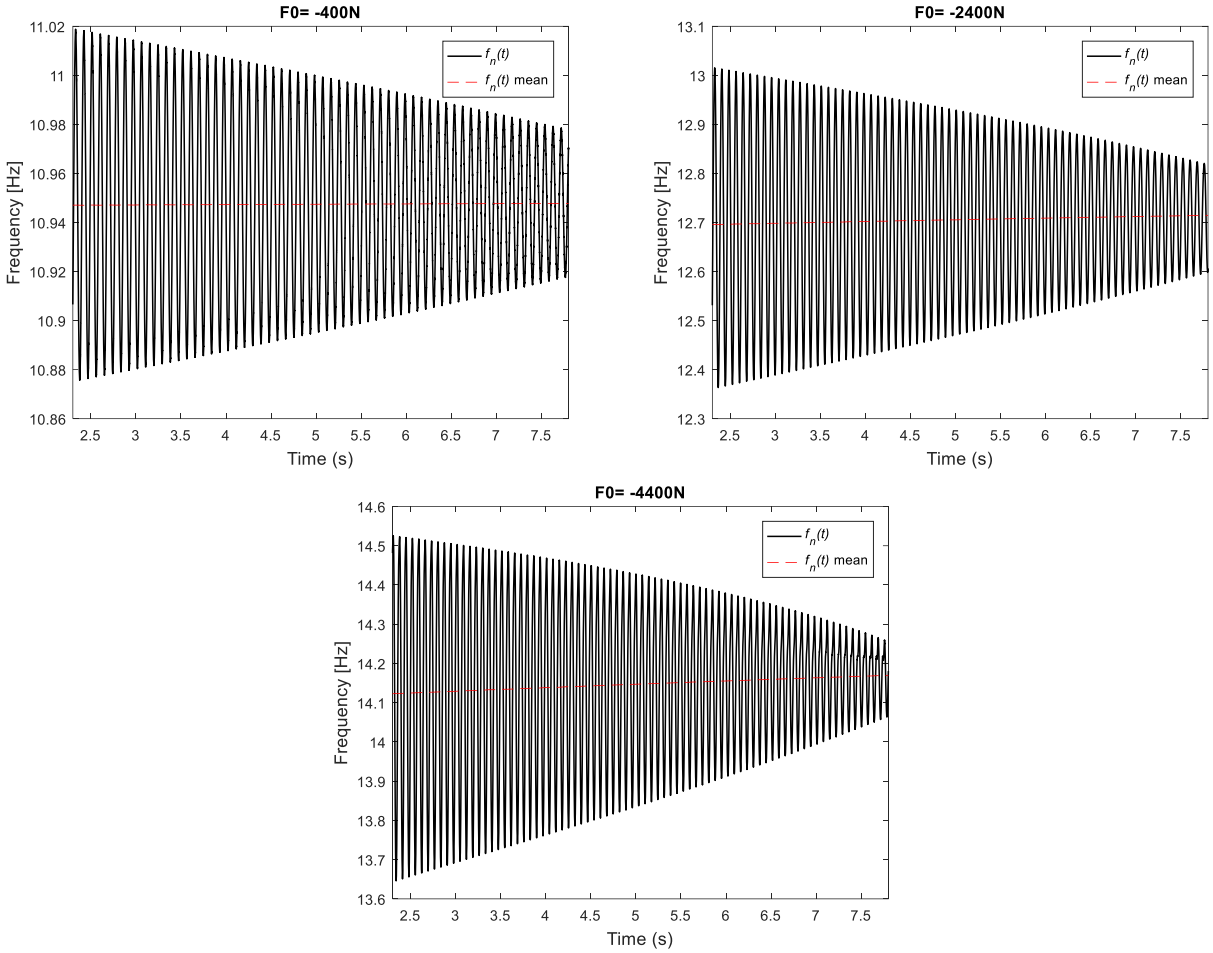

Figure 8.5.2 – Instantaneous natural frequency of the nonlinear system with negative excitations.

8.6 Conclusion

The analysis of the system's step response reveals several favourable characteristics of the equivalent suspension structure. A lower compression stiffness can effectively alleviate the impact of the bumps, enhancing the ride comfort of the vehicle. On the other hand, a higher extension stiffness contributes to more responsive handling, reducing body roll during cornering and thereby improving stability and agility. Furthermore, the evaluation of the three nonlinear functions reveals that both the nonlinear stiffness force and inertia effect significantly contribute to the nonlinearity of the system. Among them, the stiffness force consistently emerges as the most influential element in the system, dominating the overall nonlinearity of the system The application of the Hilbert transform provides insights into the instantaneous frequency characteristics of the nonlinear system under different excitations. This analysis not only confirms the softening and hardening effect during the jounce phase and extension phase, aligning with previous chapters' discussions, but also helps in comprehending the dynamic transition of the system's instantaneous frequency. Last but not least, the incorporation of energy dissipation considerations in the system during the verification experiment offers a crucial direction for aligning analytical and experimental results accurately. In summary, these findings contribute to a comprehensive understanding of the nonlinear performance of the novel suspension structure.

9. Verification with a specific Double-wishbone suspension

The verification of the novel suspension structure was conducted using a double-wishbone suspension configuration, which is a common and well-established type used in various vehicles, making it a suitable candidate for validation. Considering a specific double-wish-bone suspension designed for a high-performance Hyper-SUV, particularly the front left (FL) suspension. The vehicle data, including key parameters, is sourced from Manifattura Automobili Torino, as outlined in Table 9.1, and the suspension kinematic is referenced from Giulio Allora's prior research [20]. In Giulio Allora's research, two different suspension set-ups were evaluated for different working scenario, one is for the road use and the other is for the off-road use, called GT configuration and off-road configuration, respectively. For simplicity, discussion in this chapter concentrates on the GT configuration, as the off-road setting includes the rocker in between, demands higher ride height and increased wheel travel, and is excluded from this analysis for it falls outside the scope of the current design considerations. The suspension's hardpoints, crucial for geometry, are derived from the CAD model provided by Manifattura Automobili Torino, as detailed in Table 9.2. The kinematic of the FL suspension and the characteristic angles of the suspension as a function of the wheel travel have already been analysed and verified by Giulio Allora [19], in this chapter these characteristic angles will not be discussed in detail. The primary objective is to evaluate the vertical stiffness of the FL suspension, comparing a linear helical spring with the proposed nonlinear equivalent spring system. This comparison is crucial for understanding how the proposed novel suspension system performs in relation to a traditional linear spring in a real-world, high-performance vehicle application.

Table 9.1 – Vehicle data [20].

Configuration	Characteristic	Value	Unit of measure
General data	total weight (m_{total})	2000	kg
	unsprung masses ($m_{unsprung}$)	140	kg
	sprung masses (m_{sprung})	1860	kg
	wheelbase (wb)	3000	mm
	weight balance ($wt_{balance}$)	50/50	/
	motion ratio (MR)	0.6545	/
Wheel travel	ground clearance	140	mm
	jounce	60	mm
	rebound	100	mm
	wheel travel	160	mm
Tyre 325/30 R23	tyre sidewall	97.5	mm
	rim diameter	584	mm
	total wheel radius	389.5	mm

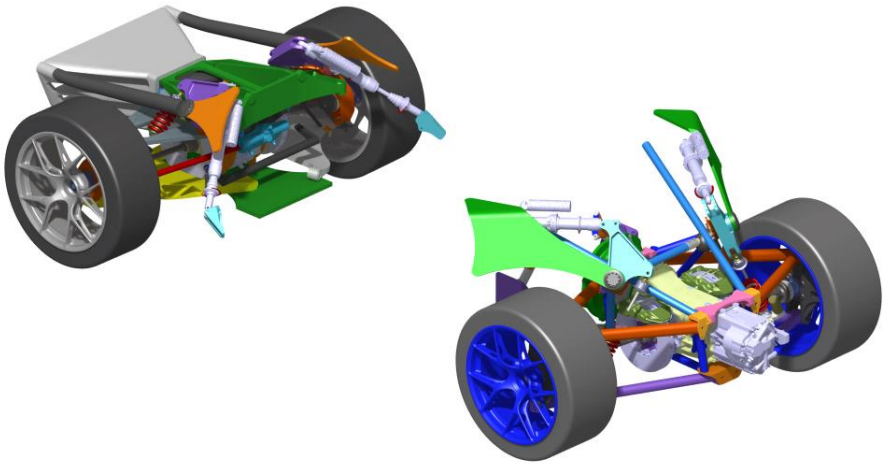

Figure 9.1 – 3D model of the Hyper-SUV (render) [20].

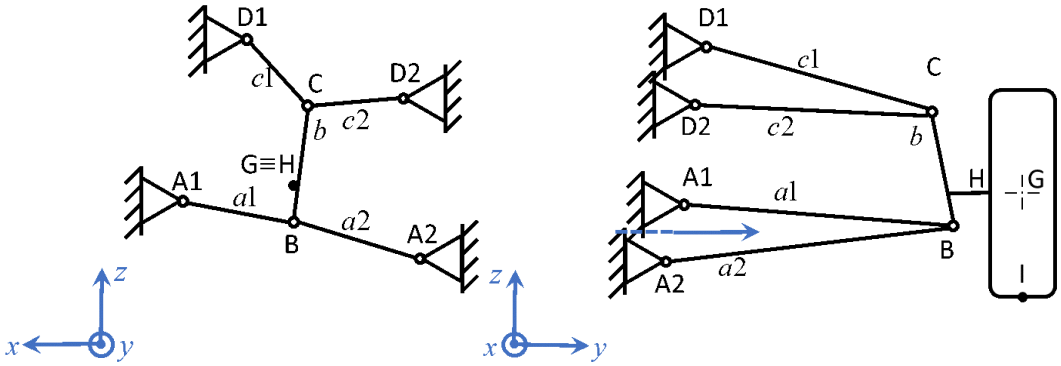

Figure 9.2 – FL 3D suspension layout right view (left) and front view (right) [20].

Table 9.2 – Suspension hardpoints in static state (GT mode) [20].

Name	Identification letter	Identification number	Front left hardpoints		
			X [m]	Y [m]	Z [m]
Lower control arm inner front	A1	101	2.40e-1	7.50e-2	1.50e-2
Lower control arm inner rear	A2	102	-2.40e-1	7.50e-2	-1.50e-2
Lower control arm outer	B	103, 104	7.52e-2	8.34e-1	3.77e-2
upper control arm inner front	D1	111	2.00e-1	1.75e-1	3.30e-1
upper control arm inner rear	D2	112	-2.29e-1	1.75e-1	3.00e-1
upper control arm outer	C	113, 114	2.01e-2	7.93e-1	3.52e-1
Tie rod Inner	E	121	-2.25e-1	9.00e-2	1.89e-1
Tie rod Outer	F	122, 123	-1.91e-1	7.52e-1	2.25e-1
Wheel centre	G	161, 162	5.03e-2	9.17e-1	1.82e-1
Upright	H	151	5.03e-2	8.57e-1	1.82e-1
Contact patch	I	192	5.03e-2	9.17e-1	-2.00e-1
Spring to LCA	P	131, 132	5.56e-2	6.62e-1	7.92e-2
Spring to car body	Q	133, 141	-3.74e-2	3.10e-1	5.00e-1

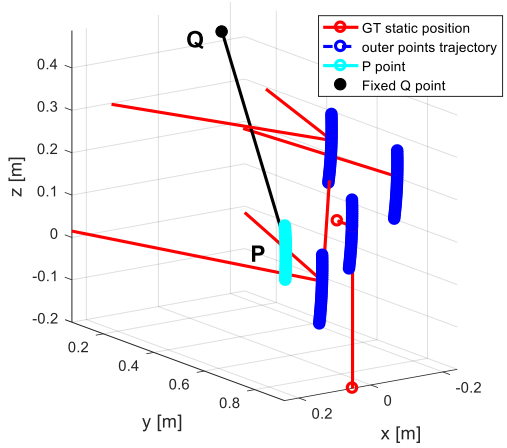

Figure 9.3 – FL suspension 3D layout and kinematics schematic.

9.1 Set the structural parameters of the proposed structure

To evaluate the effectiveness of the proposed novel structure, the particular setting of the nonlinear equivalent spring should be considered according to the provided vehicle data and suspension layout. Ensuring identical ground clearance and kinematics to the linear GT setup in a static state requires attention to the distance between points P and Q in two different configurations. To maintain the same length $\overline{PQ}$, the normal load at the wheel in static state must be concerned first, calculated by the total mass at each corner. Consequently, using the motion ratio of the suspension already evaluated from Table 9.1, the load at point P can be calculated using eq. (2.4.2). The values of these parameters are given in Table 9.1.1. The the wheel rate is determined using eq. (2.5.1) according to the imposed natural frequency, and the constant spring rate can be obtained with the wheel rate and the motion ratio (MR). As the equivalent structure features two springs, the effectiveness of the system will be discussed by considering only equipping the horizontal spring and equipping both of the two springs separately in the following subsections.

Table 9.1.1 – General data.

Configuration	Characteristic	Value	Unit of measure
General data	Normal load at each wheel	4905	N
	Load at point P	7494	N
	$\overline{PQ}$	0.5653	m
	Imposed natural frequency	1.5	Hz
	Wheel rate	44410	N/m
Linear spring	GT spring constant (k_{GT})	101958.7	N/m
	Static spring length	0.5653	m
	Spring length at rest	0.6388	m

9.1.1 Only equip the horizontal spring

For the initial evaluation, we assume that the quadrilateral structure still has four identical edges, simplifying the analysis. Assuming the PQ line as the vertical diagonal in the quadrilateral structure as shown in Figure 9.1.1.1, the length of the edges (L_1 and L_2) can be evaluated corresponding to the static angles of the system as shown in Table 9.1.1.2. We also suppose that the spring rate of the nonlinear system is same as the linear GT one. With obtained load at point P, the spring length at rest of the proposed structure can be extrapolated corresponding to the kinematic model, as shown in eq. (9.1.1.1).

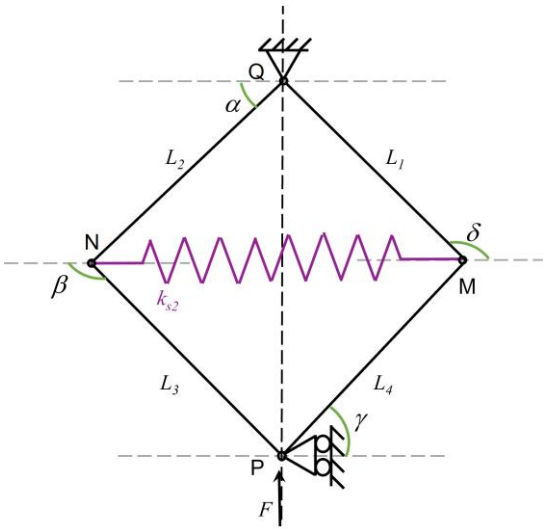

Figure 9.1.1.1 – Proposed equivalent structure only considering a horizontal spring.

$$l_{o2} = \overline{MN} + \frac{F}{k_{s2}\left(\frac{-\sin(\theta_2)-\cos(\theta_2)\tan(\alpha)}{\sin(\pi-\beta)+\cos(\pi-\beta)\tan(\alpha)}\sin(\pi-\beta)+\frac{\sin(\theta_2)-\cos(\theta_2)\tan(\pi-\delta)}{\sin(\gamma)+\cos(\gamma)\tan(\pi-\delta)}\sin(\gamma)\right)} \quad (9.1.1.1)$$

Where F is the load at point P in the static state.

Table 9.1.1.2 – Structural parameters of the equivalent system.

Configuration	Characteristic	Value	Unit of measure
Nonlinear spring (NL)	L_1	0.3997	m
	L_2	0.3997	m
	L_3	0.3997	m
	L_4	0.3997	m
	α	45	°
	β	135	°
	γ	45	°
	δ	45	°
	θ_1	0	°
	θ_2	0	°
	$\overline{OP}$	0.5653	m
	$\overline{MN}$	0.5653	m
	k_{s1}	0	N/m
	k_{s2}	101958.7	N/m

	l_{o1}	-	m
	l_{o2}	0.4918	m

Once the parameters of the proposed structure are individuated, creating a simplified model of the complete suspension becomes useful to visualize the working principle of the equivalent system. For this purpose, a MATLAB code-based software called Lupos [29] was selected. Lupos is a multi-body software with integrated FEM analysis and a wide range of applications. In this work, its use is limited to model visualization purposes, utilizing only the hardpoints coordinates for ease of manipulation and avoiding the complexity of a full CAD model.

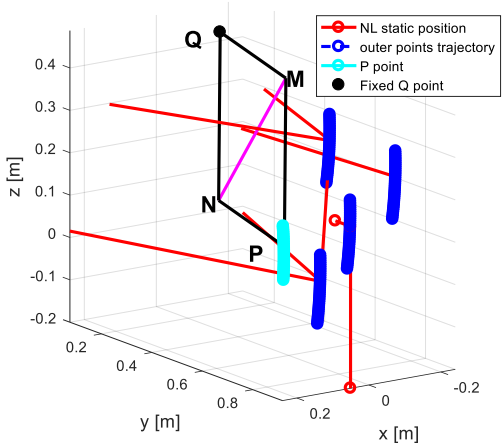

Figure 9.1.1.2 – 3D schematic of the proposed equivalent FL suspension.

A model of the suspension was created both for the vehicle set in GT configuration and for the vehicle set in nonlinear configuration (Figure 9.1.1.3 to Figure 9.1.1.6). The model is constructed by joining the hardpoints, marked by numbers in the code, and defining the sectioned geometry. It is noticeable that the suspension arms (in green) are represented with a square section beam, the steering rod (in blue) has a circular section, and the edges of the equivalent mechanism are built again using square beam elements (in violet). In contrast, the tyre and the springs were built using some commands inside the Lupos code: for the tyre, dimension and the rotation axis were specified, while the springs were built by inserting the starting and ending points and providing details such as wire section and number of spirals.

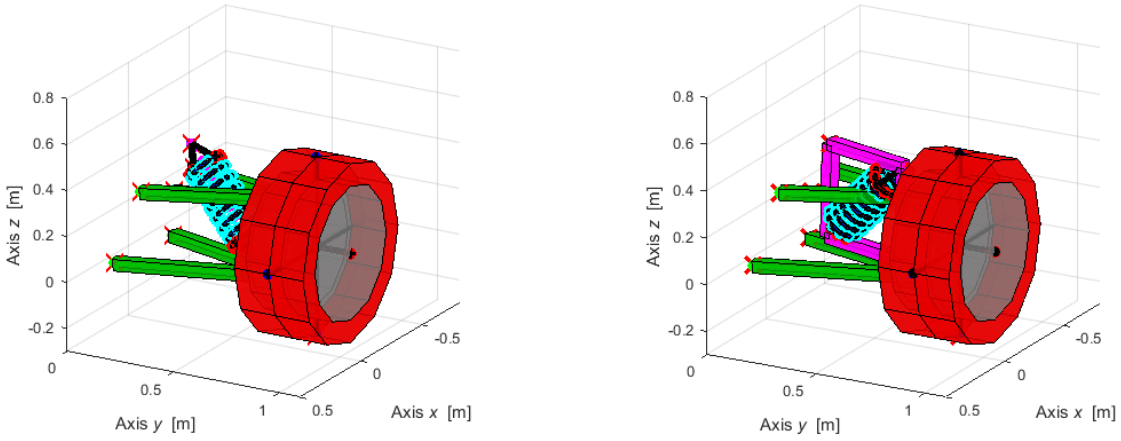

Figure 9.1.1.3 – Model of the suspension set in GT configuration and NL configuration (FL).

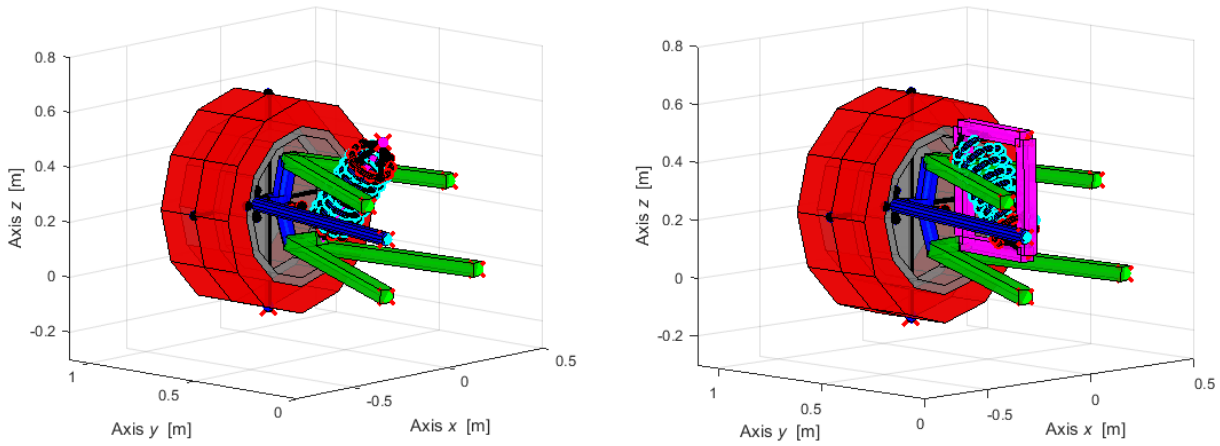

Figure 9.1.1.4 – GT inside view (left) and NL inside view (right).

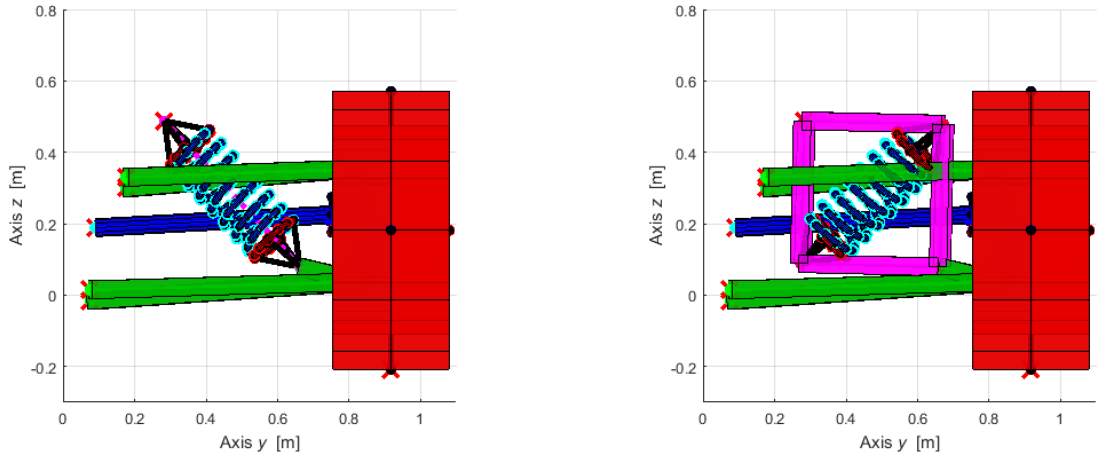

Figure 9.1.1.5 – GT front view (left) and NL front view (right).

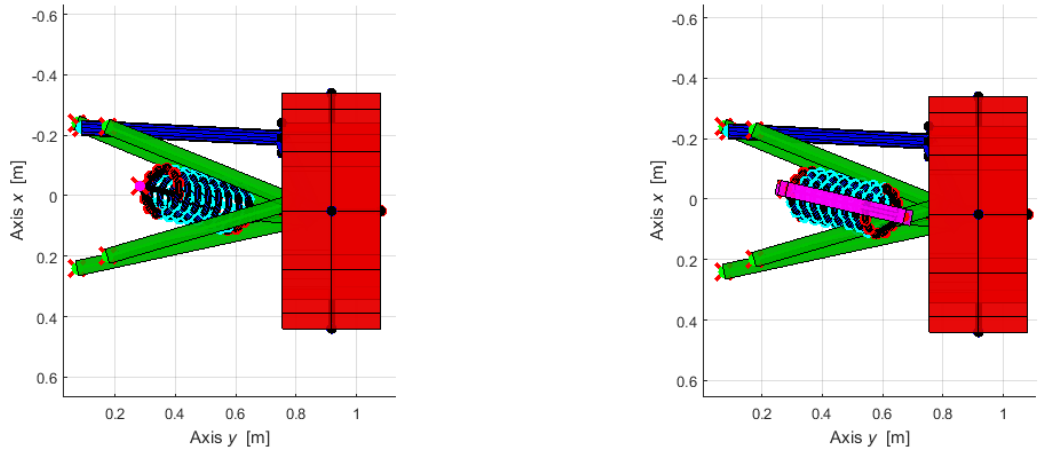

Figure 9.1.1.6 – GT top view (left) and NL top view (right).

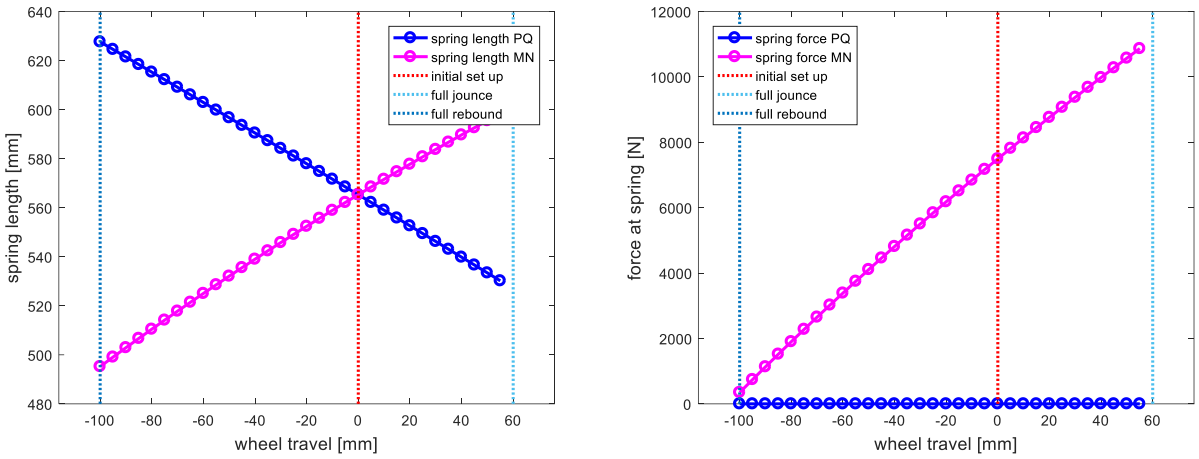

Figure 9.1.1.7 – Spring length (right) and force (left) of the proposed system vs. wheel travel.

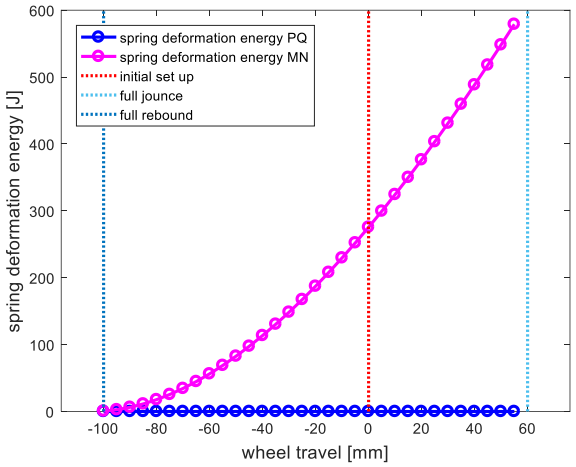

Figure 9.1.1.8 – Spring deformation energy vs. wheel travel.

The spring length is denoted by the distance between the point P and point Q, as well as the distance between the point M and point N. The deformation energy can be calculated consequently using the kinematic energy equation with the obtained parameters.

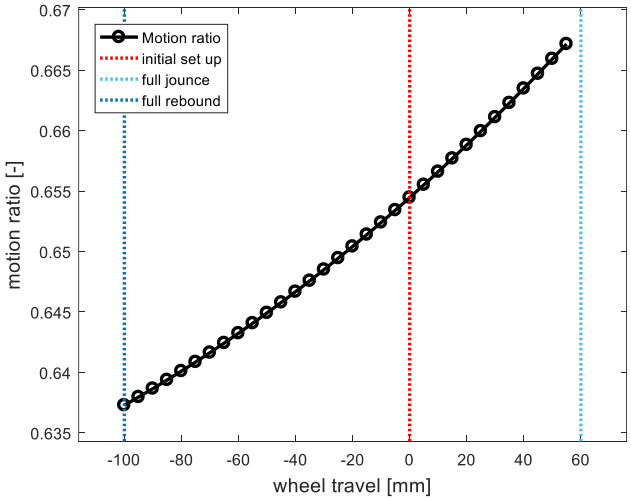

Figure 9.1.1.9 – Motion ratio of the suspension vs. wheel travel.

The motion ratio is a key parameter for evaluating the vertical performance of the suspension. As introduced in the initial sections of this work (Section 2.4), the instantaneous motion ratio of the suspension is calculated based on geometric measurements at each instant. Subsequently, the vertical stiffness at the wheel can be evaluated using the motion ratio.

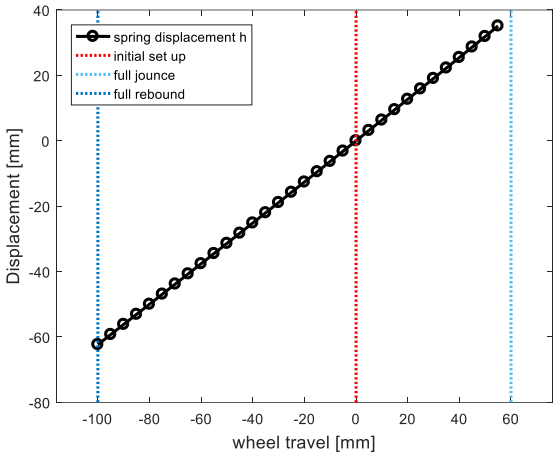

Figure 9.1.1.10 – Equivalent displacement of the structure vs. wheel travel.

The equivalent displacement of the equivalent structure is given by the variance between the static distance $\overline{PQ}$ and the instantaneous length $\overline{PQ}$, which is also considered as the input of the equivalent SDOF system. Recalling the previously derived kinematic model of the equivalent suspension system, once the structural parameters are defined, the equivalent load of the system and the equivalent stiffness of the system can be extrapolated. Having obtained the displacement as a function of the wheel position, the equivalent spring force and the equivalent stiffness of the system be calculated, and their variations with the instant wheel position are illustrated in Figure 9.1.1.11.

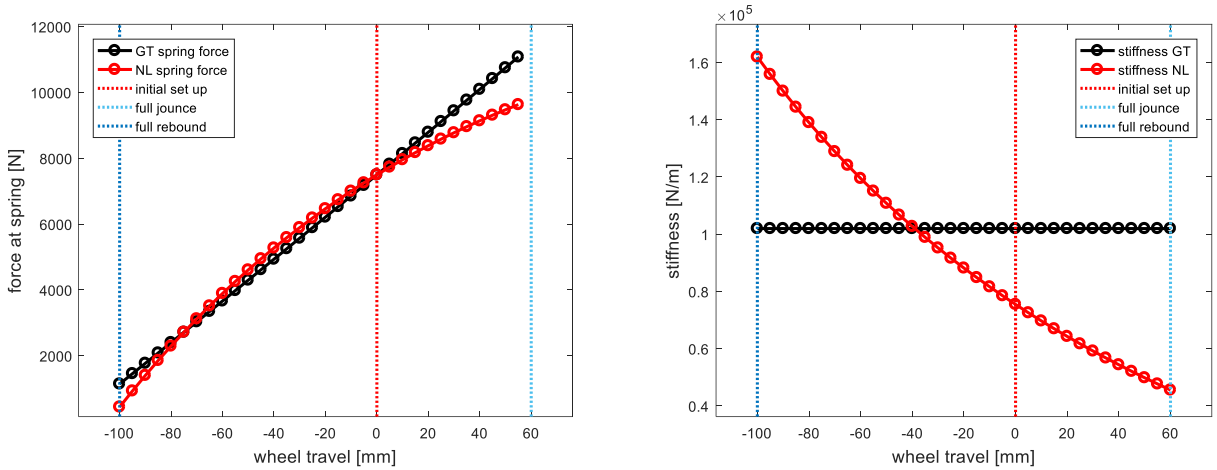

Figure 9.1.1.11 – Spring force (left) and equivalent stiffness (right) vs. wheel travel.

By adopting the equivalent structure with same constant spring rate as GT spring, the equivalent stiffness is softened to 73N/mm compared to the original 101.96N/mm in the initial set up. While the dual-response characteristic of the proposed structure causes the equivalent stiffness to increase

up to the same value as the GT setting with around 40mm of rebound travel, and the stiffness further successively increases up to 160N/mm until the wheel reaches the full rebound. With the obtained equivalent stiffness of the spring, applying eq. (2.4.3), we can determine the vertical stiffness at wheel level (wheel rate) as a function of the wheel position consequently.

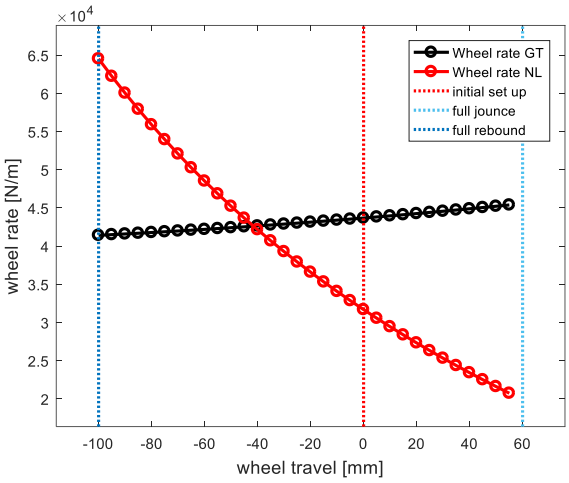

Figure 9.1.1.12 – Wheel rate vs. wheel travel.

In detail Figure 9.1.12, the wheel rate for the linear GT configuration, and the results of the nonlinear solution. Notably, from full rebound up to full jounce, the behaviours of the linear and nonlinear suspension are distinct, with the nonlinear configuration showing a wide variation in stiffness at the wheel level. A relevant aspect to be considered is the stiffness value reached by the nonlinear configuration. At full rebound it is about 50% stiffer than the linear one, while at full jounce, it is nearly 50% softer than the linear one. Finally, knowing the vertical stiffness and the vertical movement of the wheel, we can extrapolate the vertical force applied at the contact patch corresponding to the instant wheel position.

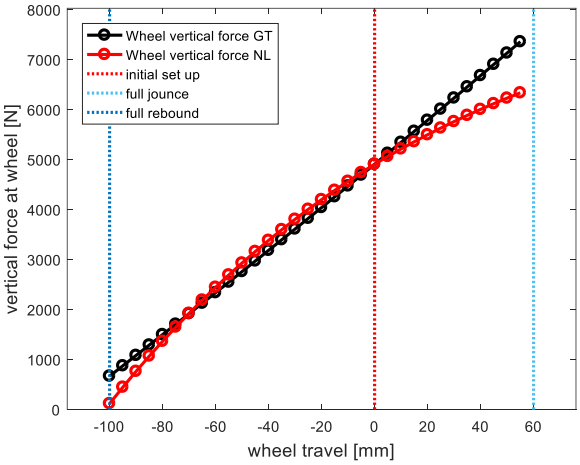

Figure 9.1.1.13 – Vertical wheel force vs. wheel travel.

Comparing the vertical force at wheel in Figure 9.1.1.13: from full rebound up to 70mm rebound, the nonlinear curve is lower than the linear one, indicating that the hardening effect will limit the extension range of the suspension, causing the wheel lose contact with the ground; from 70mm rebound to the initial position, the nonlinear configuration has a larger vertical force at wheel, which means that in this range the suspension provides more support force to provide more traction

force; and from the initial set up to the full jounce, the force is much alleviated by the nonlinear structure, demonstrating that the nonlinear system benefits the shock absorption and improves the ride comfort of the vehicle.
In conclusion, it is evident that the spring k_{s2} dominants the behavior of the system, given our consideration of only itself. By focusing on the horizontal spring, the proposed structure introduces an noticeable softening behavior: during compression, compared to a stiffer constant rate suspension, our design strategically introduces a engineered softening effect, effectively absorbing road imperfections, undulations, and shocks to create a plush and cushioned experience for the vehicle's occupants; conversely, in the rebound phase, our system employs a hardening effect, akin to a significantly softer suspension, delivering superior stability, control, and agility.
However, considering only one spring providing support to the vehicle and the system's nonlinearity simultaneously makes this configuration impractical for real-world application. Several challenges arise, such as the difficulty in determining the stiffness of the system in static state the stiffness of the system in static state, slow reaction to steering inputs, bottoming out during acceleration due to extreme softening effect, inadequate adaptation to changes in the road, and the inside cornering wheel's tendency to lose contact with the road and return at a much slower rate back to the road due to the strong hardening effect. Therefore, the system considering two springs will be discussed in the next section.

9.1.2 Equip two springs in the structure

Similarly, for the initial evaluation, we maintain the assumption of a quadrilateral structure with four identical edges. We consider the PQ line as the vertical diagonal in the quadrilateral structure as shown in Figure 9.1.2.1. The length of the edges can be evaluated based on the static angles of the system, as presented in Table 9.1.2.1. Supposing that the equivalent spring rate in the nonlinear system is tuned to be the same as the linear GT one, with both springs (k_{s1} and k_{s2}) having identical (half of the spring stiffness k_{GT}), and the normal load in static state being fully supported by spring k_{s1} while the spring k_{s2} withstands zero load in static state.

$$k_{s1} = k_{s2} = {k_{GT}}/{2} = 50979.35\text{N/m} \tag{9.1.2.1}$$

$$l_{o1} = \overline{OP} + \frac{F}{k_{s1}} = 0.6615\text{m} \tag{9.1.2.2}$$

Where F is the load at point P in static state.

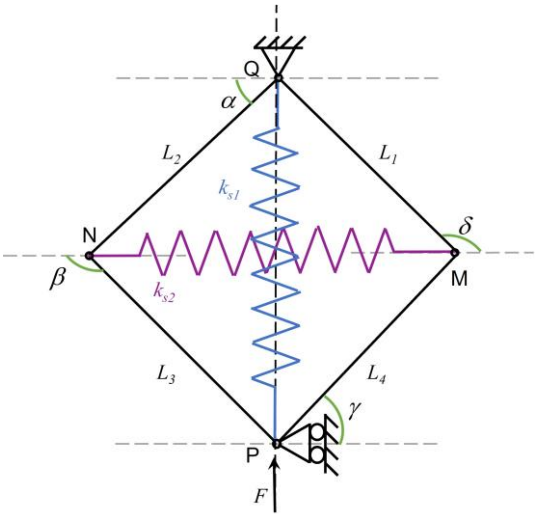

Figure 9.1.2.1 – Proposed equivalent structure with two springs.

Table 9.1.2.1 – Structural parameters.

Configuration	Characteristic	Value	Unit of measure
Nonlinear spring (NL)	L_1	0.3997	m
	L_2	0.3997	m
	L_3	0.3997	m
	L_4	0.3997	m
	α	45	°
	β	135	°
	γ	45	°
	δ	45	°
	θ_1	0	°
	θ_2	0	°
	$\overline{OP}$	0.5653	m
	$\overline{MN}$	0.5653	m
	k_{s1}	50979.35	N/m
	k_{s2}	50979.35	N/m
	l_{o1}	0.6615	m
	l_{o2}	$\overline{MN}$	m

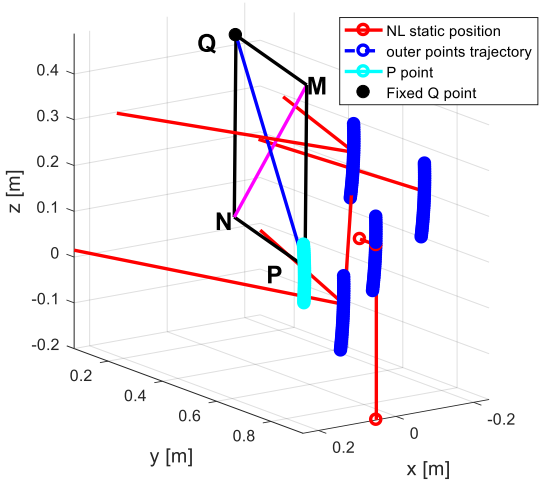

Figure 9.1.2.2 – 3D schematic of the proposed equivalent suspension.

Again, taking advantage of the Lupos model [29], we can visualize the suspension easily. Models of the suspension was created both for the vehicle set on GT configuration and the structure set with two springs (Figure 9.1.2.3 to Figure 9.1.2.6). In the substituted configuration, the horizontal spring is built inserting the starting and ending points and giving the wire section and number of spirals, while the vertical spring is represented by a lump spring with a dotted line to avoid the superimposition of the two springs.

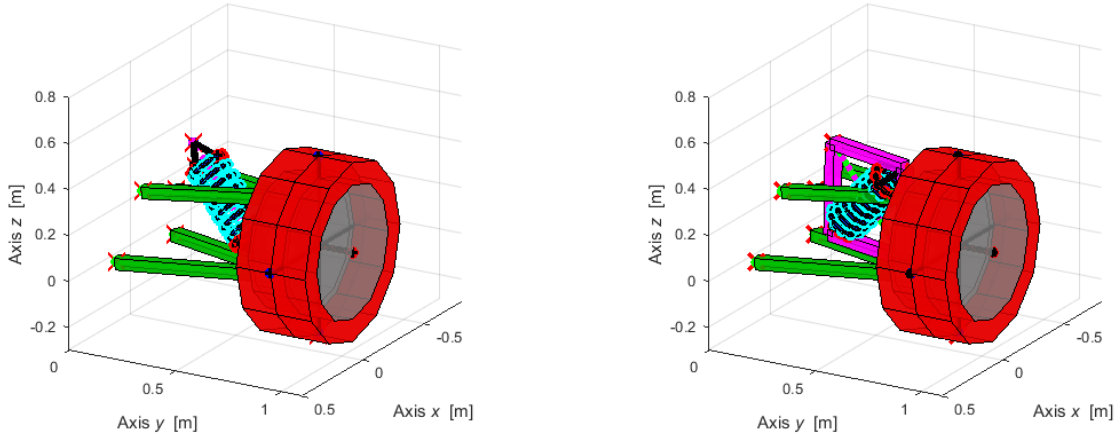

Figure 9.1.2.3 – Model of the suspension set on GT configuration and NL configuration (FL).

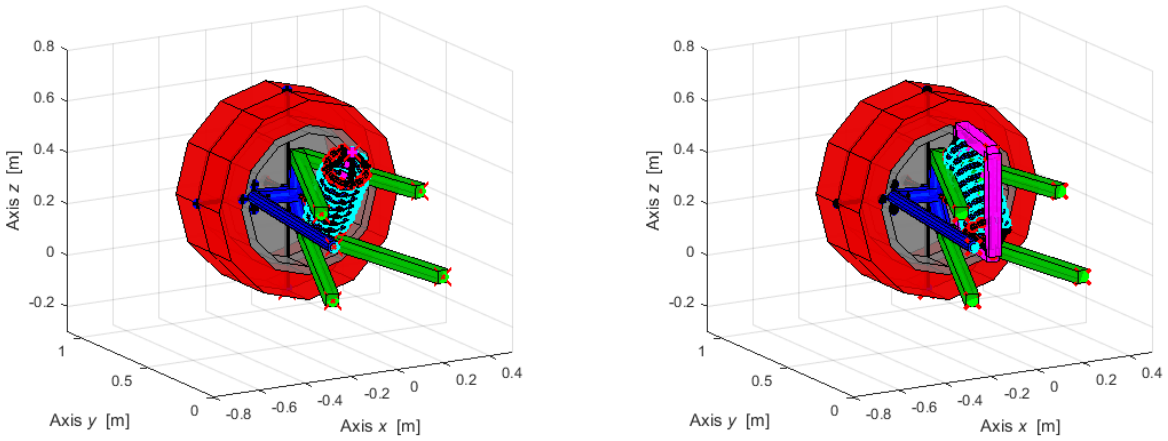

Figure 9.1.2.4 – GT inside view (left) and NL inside view (right).

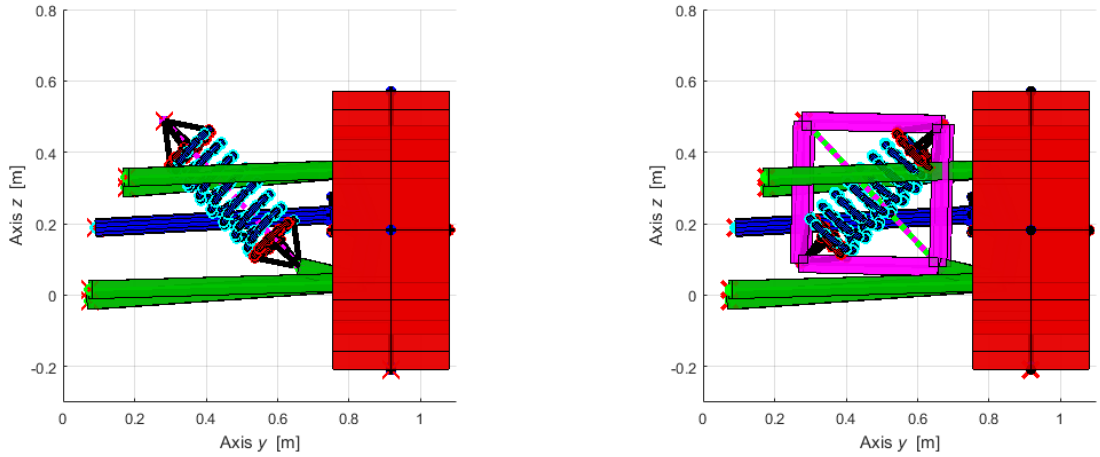

Figure 9.1.2.5 – GT front view (left) and NL front view (right).

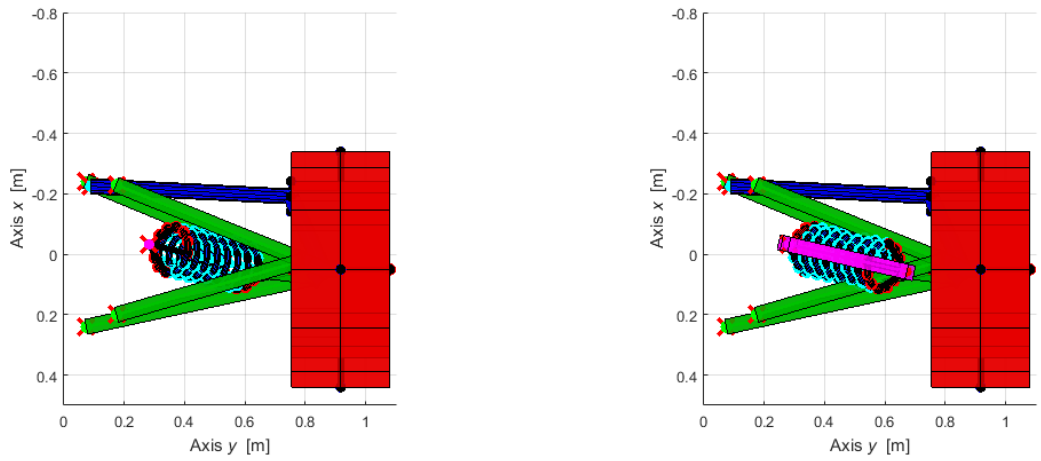

Figure 9.1.2.6 – GT top view (left) and NL top view (right).

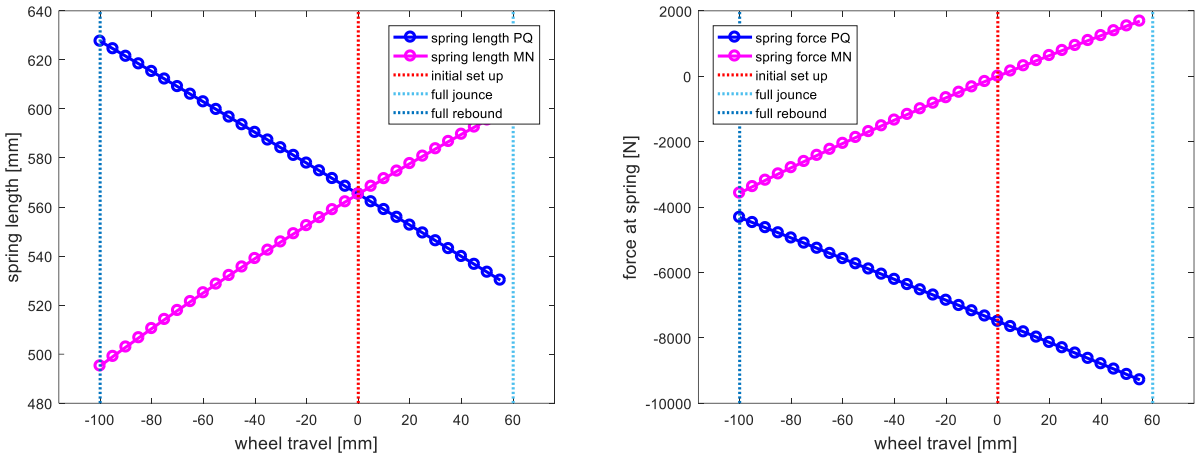

Figure 9.1.2.7 – Spring length (right) and force (left) of the proposed system vs. wheel travel.

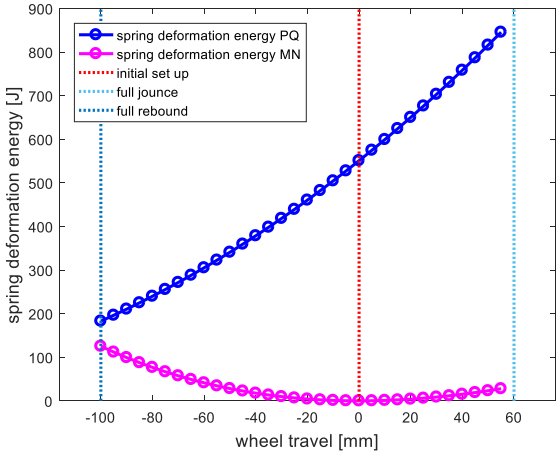

Figure 9.1.2.8 – Spring deformation energy vs. wheel travel.

The spring length and spring force versus the wheel travel of the two springs are shown in Figure 9.1.2.7. Instead of the single spring configuration, the behavior of the system is influenced by the cooperation of the two springs. In this configuration, the vertical spring stands most of the

load, and the horizontal spring serves as an auxiliary component. The storing energy in spring k_{s1} is larger than that in spring k_{s2} as shown in Figure 9.1.1.8, and the nonlinearity of spring k_{s2} is also indicated.
The motion ratio, and the equivalent displacement of the system have already been discussed in section 9.1.1, here we will not delve into the details again. With the obtained displacement as a function of the wheel position, again, the equivalent spring force and the equivalent stiffness of the system are calculated as a function of the instant wheel position as shown in Figure 9.1.2.9, based on the kinematic model of the proposed system.

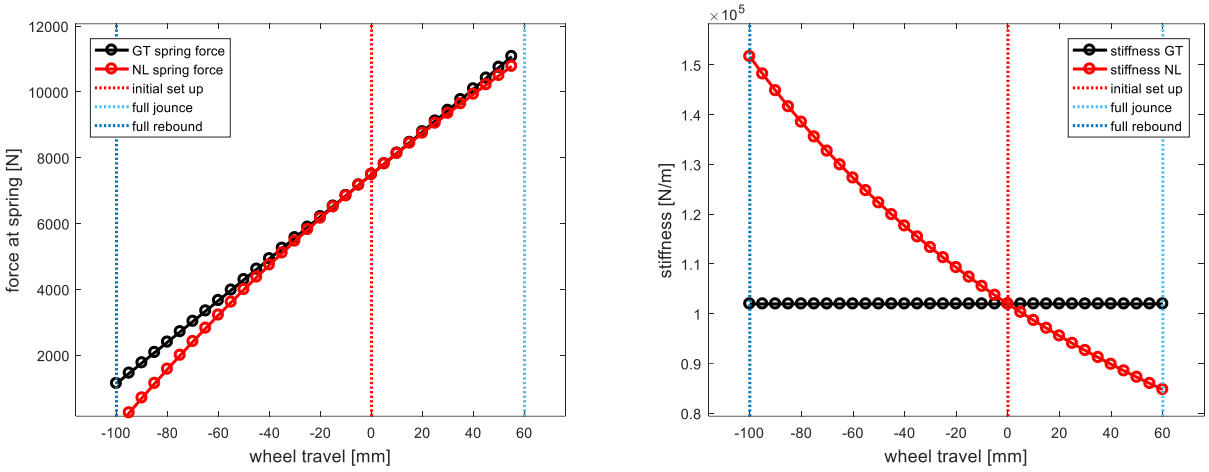

Figure 9.1.2.9 – Spring force (left) and equivalent stiffness (right) vs. wheel travel.

With the same equivalent stiffness in static state, in full bounce, the equivalent stiffness is softened to 85N/mm instead of the original GT stiffness 101.96N/mm, which is about 15.6% softened. While the dual-response characteristic of the proposed structure causes the equivalent stiffness to increase in the rebound phase, and it successively increases up to the 152N/mm at full rebound, which is about 49% stiffer than the GT setting. Consequently, with the obtained equivalent stiffness of the system, applying eq. (2.4.3), we can determine the wheel rate as a function of the wheel position.

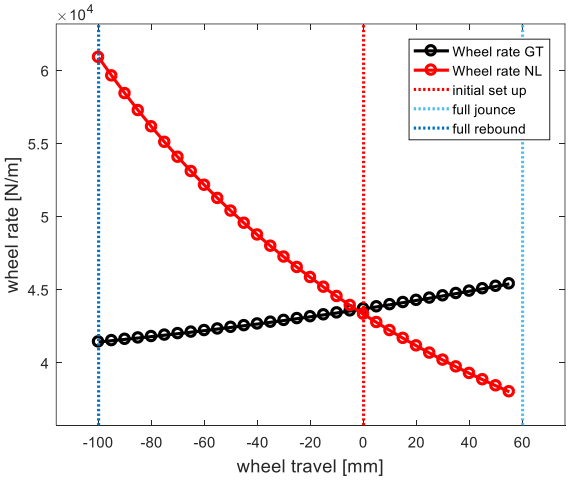

Figure 9.1.2.10 – Wheel rate vs. wheel travel.

In detail, Figure 9.1.2.10 reports the wheel rate for the linear GT configuration, and the results of the nonlinear solution. Notably, from full rebound up to full jounce, the GT and nonlinear configuration show a very different behaviour. The GT setting demonstrates a gradually hardening

effect from full rebound to full jounce, mainly influenced by the suspension geometry. However, the nonlinear configuration exhibits a wide softening effect of stiffness at the wheel level. A relevant aspect to be considered is the stiffness value, which is modified by the nonlinear configuration. At full rebound, it is about 50% stiffer than the linear one, while at the full jounce, it is nearly 15% softer than the linear one. Finally, knowing the vertical stiffness and the vertical movement of the wheel, we can extrapolate the vertical force applied at the contact patch corresponding to the instant wheel position.

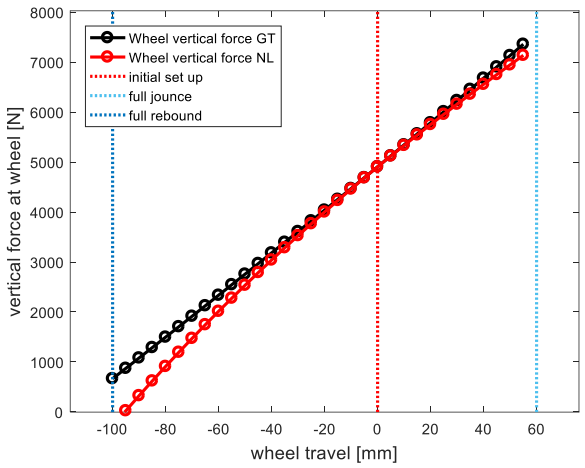

Figure 9.1.2.11 – Vertical wheel force vs. wheel travel.

Comparing the vertical force at wheel in Figure 9.1.2.11: in the full rebound phase, the wheel force in nonlinear structure is lower than the linear one, indicating that the hardening effect makes the vehicle more sensitive and handling, stabling the vehicle and enabling the driver to receive more information from the road, while it also imposed a limitation on the extension range of the suspension, potentially causing the wheel to lose contact with the ground; from the initial position to full jounce, the wheel force is mitigated by the nonlinear structure, showing that the nonlinear system enhances shock absorption and the ride comfort of the vehicle.
In conclusion, this configuration addresses some of the limitations observed in the single-spring system, such as the difficulty in determining the stiffness of the system in static state and the potential for bottoming out during acceleration, bringing more flexibility to adjust the performance of the system. The two-spring configuration offers improved responsiveness to steering inputs and better adapts to changes in the road, and provides a more balanced performance that enhances both handling and ride comfort. However, it's evident that the initial evaluation of the novel system is not without its shortcomings, particularly the pronounced hardening effect in the extension phase, posing challenges to ride quality and potentially causing the wheel to lose contact with the road. Further refinement is necessary to optimize the system's overall performance.

9.1.3 Sensitivity and consistency analysis

Fortunately, due to the tuneability and ease of design in our system, we have the capability to fine-tune its performance by setting the desired stiffness curve. Analysing the sensitivity of the design parameters is crucial to learn the correct direction for tunning our system. The performance of the structure is primarily determined by the typology of the quadrilateral shape and the stiffness of the springs, assuming the geometry of the suspension is given. In this section, we focus on assessing the sensitivity of the system's behaviour by varying the spring rates while keeping the quadrilateral shape unchanged.

Strating from the initial configuration, as detailed in section 9.1.2, where we set the spring rate k_{s1} and k_{s2} equal to half of the spring rate k_{GT} (50979.35N/m), ensuring that the equivalent wheel rate in the static state matches the GT configuration. To guarantee the same wheel rate in the static state, we need to impose a constraint on the two spring rates, expressed in eq. (9.1.3.1), where the sum of two spring rates equals k_{GT}. By gradually increasing the spring rate k_{s1} up to k_{GT}, as shown in Figure 9.1.3.1, we can anticipate that the proposed system behaves like a traditional system, with performance equivalent to GT configuration.

$$k_{s1} + k_{s2} = k_{GT} = 101958.7\text{N/m} \tag{9.1.3.1}$$

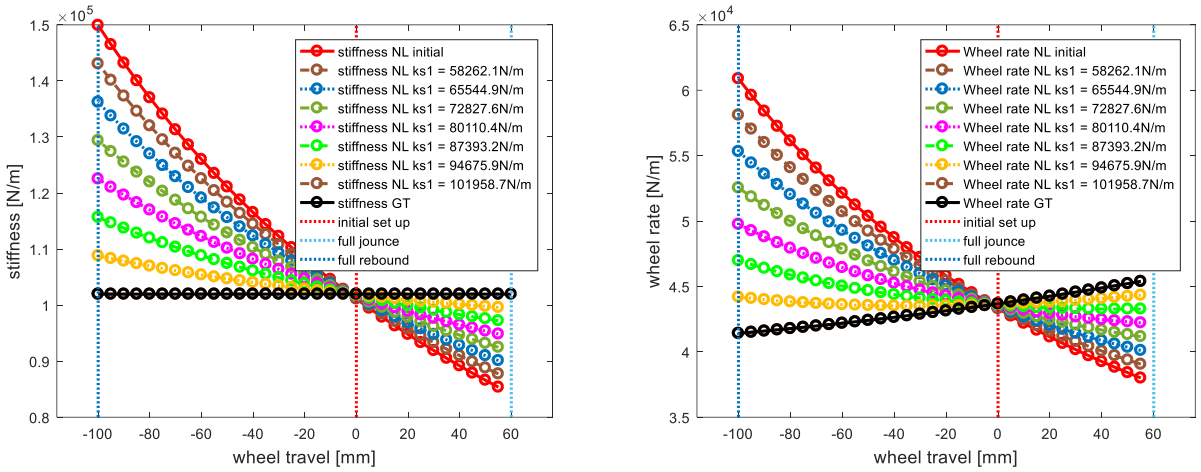

Figure 9.1.3.1 – Equivalent stiffness (left) and wheel rate (right) by modifying the spring rates.

In detail of Figure 9.1.3.1, k_{s1} is evaluated in the range of [50979.35N/m 101958.7N/m], with eight values extracted evenly. Consequently, k_{s2} should be in the range of [0N/m 50979.35N/m], complementing k_{s1}. The red solid line indicates the initial configuration discussed in section 9.1.2, and the solid black line indicates the GT configuration. From the initial condition in which the spring rates are identical, the six lines in between showcase the variation in the structure's performance by increasing k_{s1} successively. When k_{s1} equals k_{GT} at the end, the brown dashed line superimposes with the solid black line, indicating that the equivalent system is consistent with the traditional system. Hence, by modifying the spring rates, the wheel rate of suspension with the proposed system can be effectively designed across a wide range: increasing k_{s1} alleviates the nonlinearity of the system, while in the opposite direction, increasing k_{s2} leads to the dominance of the behaviour of the system by the softening effect.

9.2 Fit the suspension

Now, considering a new GT configuration in which the hardpoint of the pivot Q is modified compared to the original GT configuration as shown in Table 9.2.1. All the other hardpoints are remain constant with referential GT configuration.
As a result of the modification, the motion ratio of the suspension is different from the original one. In the static state, the motion ration in the new GT configuration is 0.4858 which is lower than the reference 0.6545. Additionally, the slope of the motion ratio curve is more vertically inclined than the original one as depicted in Figure 9.2.1.

Table 9.2.1 – Hardpoint of Q in static state in ref. GT and new GT mode

Configuration	Name	Identification letter	Identification number	Front left hardpoints		
				X [m]	Y [m]	Z [m]
Referential	Spring to car body	Q	133, 141	-3.74e-2	3.10e-1	5.00e-1
New	Spring to car body	Q	133, 141	-3.74e-2	1.00e-2	5.00e-1

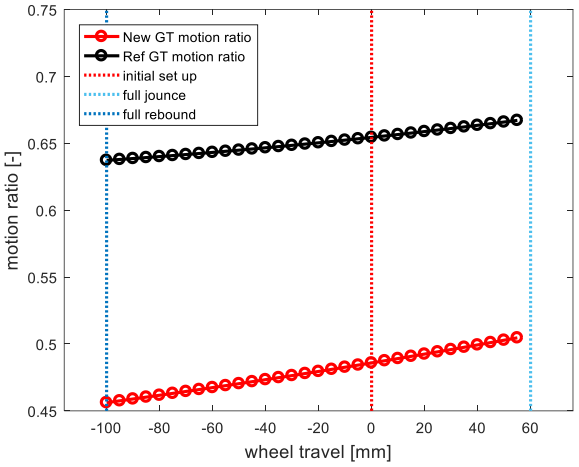

Figure 9.2.1 – Motion ratio of referential GT configuration and new GT configuration.

To keep the wheel rate of the suspension in the static state in new configuration constant with the original condition, we need to fit the spring rate in new GT mode to ensure the same wheel rate. As we already know, the wheel rate in the original GT mode in the static state is 44410N/m, by applying eq. (2.5.1), the value of k_{GT} in the ew configuration can be extrapolated as shown below.

$$k_{GT} = \frac{WR}{MR^2} = \frac{44410\text{N/m}}{0.4858^2} = 188176.7\text{N/m} \tag{9.2.1}$$

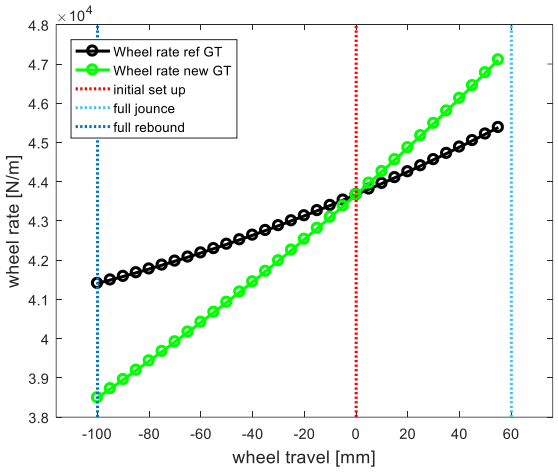

Figure 9.2.2 – Wheel rate of referential and new GT configuration.

By fitting the spring rate, the wheel rate of the new GT configuration can be individuated, as shown in Figure 9.2.2 with a green solid line. Compared to the reference GT configuration, the new one exhibits a more evident hardening effect since a stiffer spring is used. Considering the GT mode pursues the driving comfort and agility simultaneously, the ride quality could be affected by the severe hardening effect in the new GT configuration. Therefore, the goal is to flatten the wheel rate

of the new configuration, and the slope of original configuration serves as a corking reference for this fitting.
Unfortunately, when considering a traditional method to fit the wheel rate, as shown in Figure 9.2.3, tunning the spring rate k_{GT} only to try to algin the new and referential curves. It can be observed that by decreasing the value of k_{GT} by 10000N/m, 40000N/m, and 80000N/m, the wheel rate curve is flattened effectively, however, at same time, the initial wheel rate in the static sate is also impacted by the change, compromising the dynamic behaviour of the suspension. With this method, it is unfeasible to permit the desirable wheel rate curve and the imposed natural frequency of the suspension at the same time.

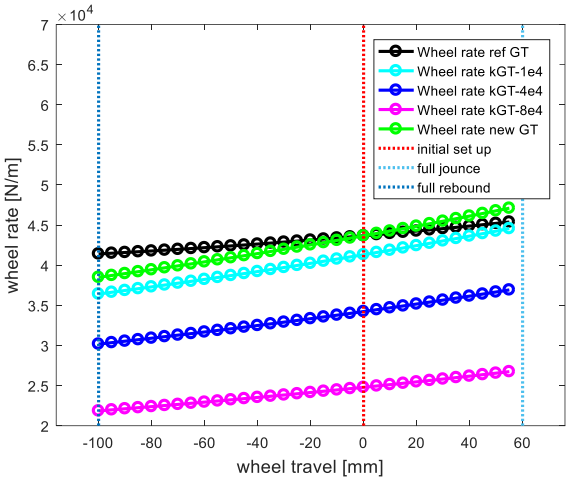

Figure 9.2.3 – Fitting the wheel rate of the new GT configuration by modifying k_{GT}.

However, with our proposed structure, tuning the wheel rate becomes straightforward by coordinating the two springs in the system, ensuring the designed dynamic characteristics of the suspension. To evaluate the equivalent system, we start from the initial setting, as performed in section 9.1.2, where the spring rates k_{s1} and k_{s2} are still equal to half of k_{GT} (188176.7N/mm), which is 94088.35N/m in the new NL configuration. As shown in Figure 9.2.4, the initial evaluation of the wheel rate with the proposed structure is indicated by the red solid line, and the green solid line represents the wheel rate of new GT mode with the traditional structure. Since we have discussed the sensitivity and consistency of the proposed system in section 9.1.3, it can be inferred that the wheel rate in the range between the red and green line should be possible to achieve.

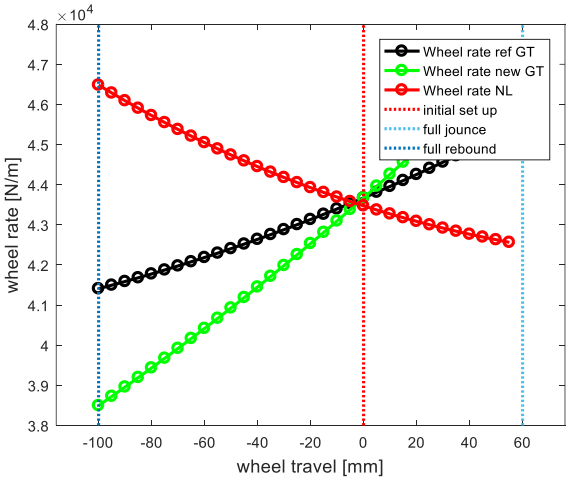

Figure 9.2.4 – The wheel rate of the referential GT, new GT, and initial NL configuration.

Consequently, a setting of the equivalent structure exists to align with the referential black line, and through trial and error, we finally found the corresponding setting as shown in Table 9.2.2. Where the spring rate k_{s1} is tuned up, and the spring rate k_{s2} is tuned down, while keeping identical geometric parameters. With this spring setting, the performance of the equivalent suspension is modified significantly compared to the GT configuration and algins well with the referential configuration as shown in Figure 9.2.5.

Table 9.2.2 – Initial and fitted settings of the equivalent structure.

Configuration	Characteristic	Value	Unit of measure
Quadrilateral shape	L_1	0.5646	m
	L_2	0.5646	m
	L_3	0.5646	m
	L_4	0.5646	m
	α	45	°
	β	135	°
	γ	45	°
	δ	45	°
	θ_1	0	°
	θ_2	0	°
	$\overline{OP}$	0.7985	m
	$\overline{MN}$	0.7985	m
Initial conf.	k_{s1}	94088.35	N/m
	k_{s2}	94088.35	N/m
	l_{o1}	0.9077	m
	l_{o2}	$\overline{MN}$	m
Fitted conf.	k_{s1}	152088.35	N/m
	k_{s2}	36088.35	N/m
	l_{o1}	0.8656	m
	l_{o2}	$\overline{MN}$	m

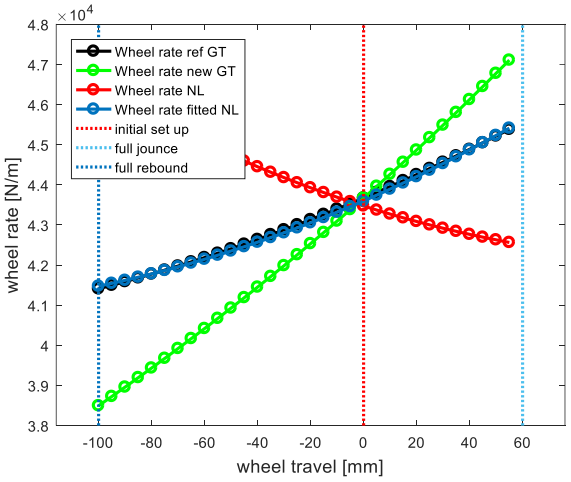

Figure 9.2.5 – The fitted wheel rate by tunning the spring rates of NL configuration.

In this figure, the blue line is the wheel rate after the fitting process, and compared to the green line, the slope is strategically flattened without changing the static property and scarifying the dynamic performance. The proposed equivalent suspension offers an easy and flexible way to fit the desired characteristic of the suspension, even when the suspension geometry is fixed, which is unfeasible if we aim for a similar function with traditional suspension.

9.3 Tune the equivalent structure

Although the proposed system showed a quite unique softening effect compared to the traditional suspension with a hypothetical setting in section 9.1, a suspension with an excessively strong softening effect throughout its working range is impractical in real condition. The driver would lose the feedback from the road, and the response of the vehicle will become more bulk, resulting in an unpredictable driving experience. While it would be appreciated if we fine-tune the softening effect to some extend to improve the ride quality of the vehicle, which means we intend to adjust the wheel rate of the suspension using the proposed structure to compensate the hardening effect due to the geometric characteristic and aligning the target wheel rate. By doing so, the wide tunability of and the utility of the system will be assessed.
Given that the problem has been set and solved analytically, and the structure of the system can be easily altered, it is intuitively to think about a tuning process for the equivalent suspension. As the effectiveness of the structure relies on the shape of the quadrilateral and the rate of the springs, the optimization is confined to few parameters, and the optimization process is established as an exercise to verify whether the problem is well written and suitable for an optimization run.
Optimization is the process of maximizing or minimizing an objective function considering the design constraints and acting on some defined input parameters, called decision variables. The first step is the individuation of the objective function, specifying the criteria for optimization. In general, there may be multiple criteria, and it's essential to clearly establish the relative importance of each criterion. The next step is the individuation of the decision variables, which are the input parameters that can be changed and impact the system's behaviour, dimension, properties, etc. Modifying these decision variables should result in the changes to the output of the system, which is included in the objective function. The design or external constraints depend on the nature of the problem, involving the maximum dimension or weight of the system and some geometric constraints.
In this case study, the optimization problem is formulated in the following way: the target output is a modified wheel rate curve, which can be obtained by modifying the lengths and angles of the quadrilateral. Since the volume of the system is not considered for the theoretical analysis, the optimization process is limited to this set up.
The objective function of this problem is set as follow:

$$f(\mathbf{x}) = \left| \frac{k_w - k_{ref}}{k_{ref}} \right| \text{ where} \tag{9.3.1}$$

$$k_w = \text{ evaluated wheel rate}$$

$$k_{ref} = \text{ target wheel rate}$$

Where the evaluated wheel rate is the output of the system, like the curves reported in Figure 9.1.1.12 and Figure 9.1.2.10, and is evaluated at each optimization iteration with varying values of the decision variables. The target wheel rate, reported with the blue line in Figure 9.3.1 along with the wheel rate of the original GT configuration and initial NL configuration of the structure, serves as the reference that the optimization aims to achieve. The objective of this optimization is to mitigate the hardening effect in the rebound phase, resulting from the

characteristics of the equivalent system, and alleviate the hardening effect in the jounce phase, caused by the suspension geometry, ultimately achieving a smoother wheel rate.
Meanwhile the target is impossible to realize due mainly to the fact that to identify an optimal trend for the vehicle here analysed. The objective function, in this context, assigns a value for each instantaneous wheel position, reflecting the difference between the target and evaluated values, the error between the two curves. Since the target is to have an objective function able to include the error between the two curves for the whole wheel travel, the objective function is modified as to include the sum of all the errors between the two curves. This formulation of the objective function explains why in this case the process is framed as a minimization task. The system tries to modify the decision variables to minimize the objective function. In a hypothetical scenario where the optimization procedure identifies a suspension configuration precisely matching the target wheel rate, the objective function would be reduced to zero.
To obtain this target wheel rate, the quadrilateral geometry and spring rates are designed as decision variables. The input vector, denoted as **x,** contains the length L_1, and L_2 angles α , and δ ,and spring rates k_{s1}, and k_{s2}. Note that the distance between P and Q in static state remains constant during the optimization. The lengths are allowed to vary within a range of ± 0.2 m from the original coordinates, the angles with ± 15 degrees, the spring rate k_{s1} within the range of [25489.67N/m, 101958.7N/m], and the spring rate ks2 is set as the value of k_{GT} minus k_{s1}. These limitations on the selected values can be considered as design constraints within the optimization process.

$$\min f(\mathbf{x}) \tag{9.3.2}$$

$$f(\mathbf{x}) = \sum_{i=1}^{n_w} \left| \frac{k_w - k_{ref}}{k_{ref}} \right| \tag{9.3.3}$$

where $n_w =$ evaluated suspension positions

$$\mathbf{x} = \{L_1, L_2, \alpha, \delta, k_{s1}, k_{s2}\} \tag{9.3.4}$$

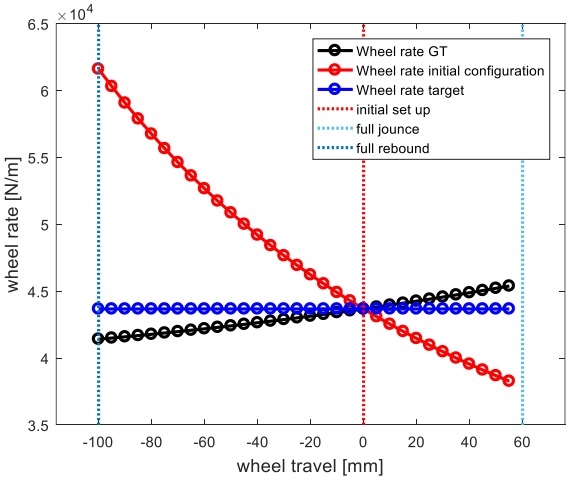

Figure 9.3.1 – Wheel rate target used for the optimization (FL).

Table 9.3.1 – Decision variables and range of variability.

Decision variable	Minimum value	Initial value	Maximum value
L1 [m]	0.1997	0.3997	0.5997
L2 [m]	0.1997	0.3997	0.5997
α [°]	30	45	60

δ [°]	120	135	150
k_{s1} [N/m]	25489.67	50979.35	101958.7
k_{s2} [N/m]	k_{GT}-k_{s1}		

Once the optimization parameters are all defined, the optimization is launched. At each iteration, the software solves the system with a different set of input variables and evaluates the objective function value. In other words, it launches the code used to solve the springs system of the previous section with a different starting position and dimension of the quadrilateral. While the suspension kinematics remains constant, the dynamic equilibrium condition of the quadrilateral is adjusted at each iteration throughout the whole wheel travel.
Figure 9.3.2 and Figure 9.3.3 report the input decision variables for the whole optimization process. The first figure presents the real values, while the second one normalizes these values. Figure 9.3.4 displays the objective function values for each iteration, with the ordinate axis depicted logarithmically to accentuate errors and convergence trends.
It is noticeable that at some iterations, just one input coordinate is modified, while for other iterations, the coordinates are changed in combination. This way, called one parameter sensitivity analysis, consists in changing one input parameter per time. Once all the parameters are modified and the impact on the objective function is evaluated for each decision variables, the optimization seeks the best combination of them. Every time a lower objective function is obtained, the procedure restarts, modifying one parameter at a time, and so on.

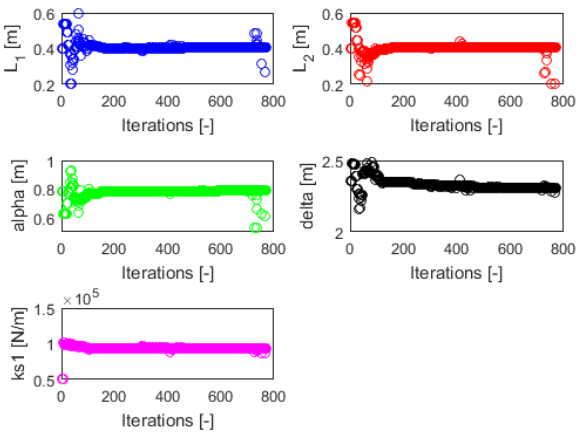

Figure 9.3.2 – Decision variables of the optimization problem (FL).

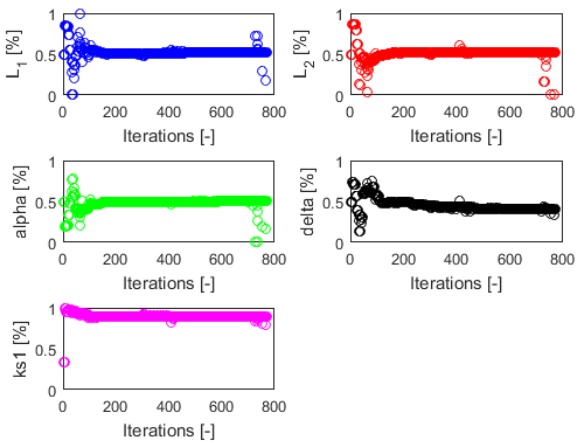

Figure 9.3.3 – Normalized decision variables of the optimization problem (FL).

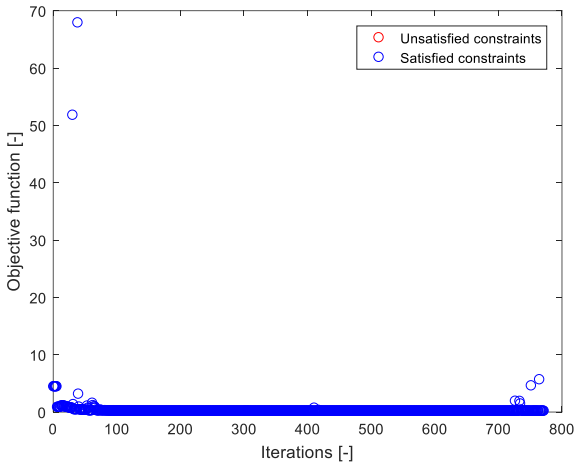

Figure 9.3.4 – Objective function values as a function of the iteration (FL).

At each iteration, the optimization process gives back a summary of the input variables and the objective function value. This entails executing the entire MATLAB code used to evaluate the system behaviour, modifying the starting position and geometry of the quadrilateral based on the values evaluated by the optimization procedure. The decision variables and the objective function values for the lowest error are reported in the table below, alongside the original values, to facilitate the comparison.

Table 9.3.2 – Optimized results.

Variable	Original value	Optimization value
L1 [m]	0.3997	0.4088
L2 [m]	0.3997	0.4064
α [°]	45	45.2
δ [°]	135	132.2
k_{s1} [N/m]	50979.35	94224.44
k_{s2} [N/m]	50979.35	7734.3
Objective function	4.4018	0.1468

Before reporting the results with the optimized setting, a focus on highlighting the differences in geometric parameters is proposed. Figure 9.3.5 to Figure 9.3.8 show the comparison between original and optimized geometry. The left ones represent the original configuration, while the right ones depict the optimized configuration.

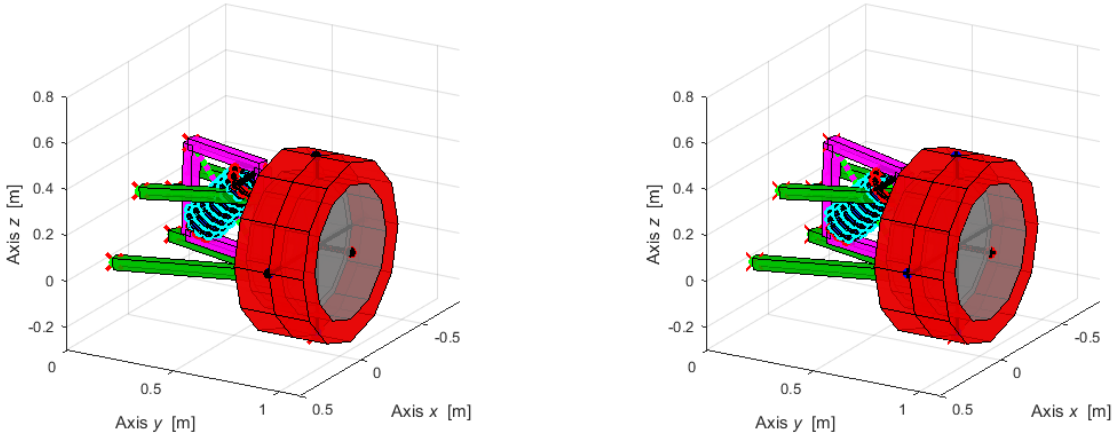

Figure 9.3.5 – Initial (left) and tunned (right) equivalent configuration (FL).

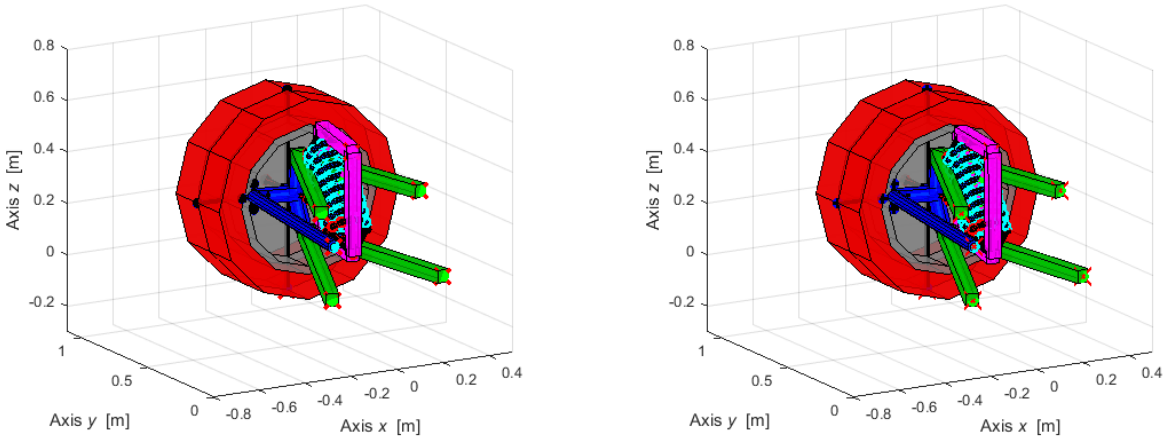

Figure 9.3.6 – Initial (left) and tunned (right) configuration (FL) inside view.

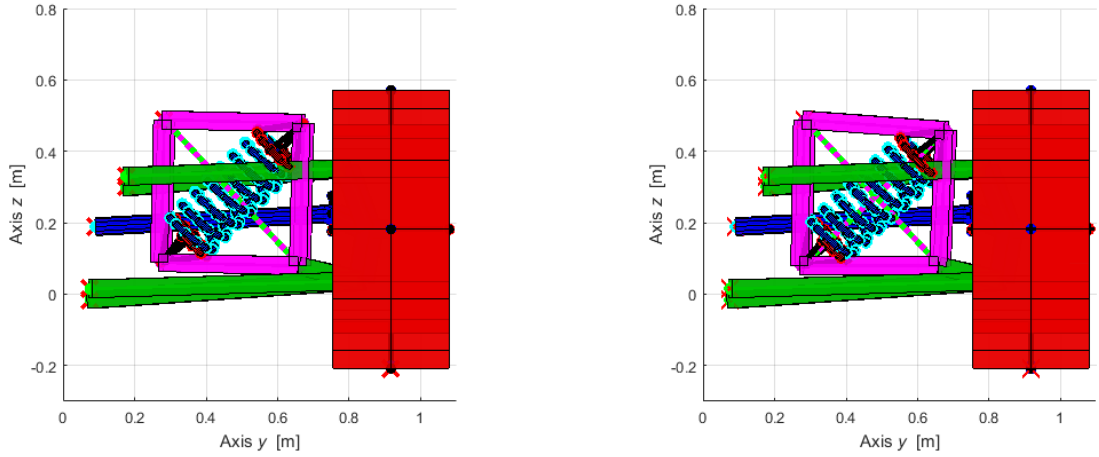

Figure 9.3.7 – Initial (left) and tunned (right) configuration (FL) front view.

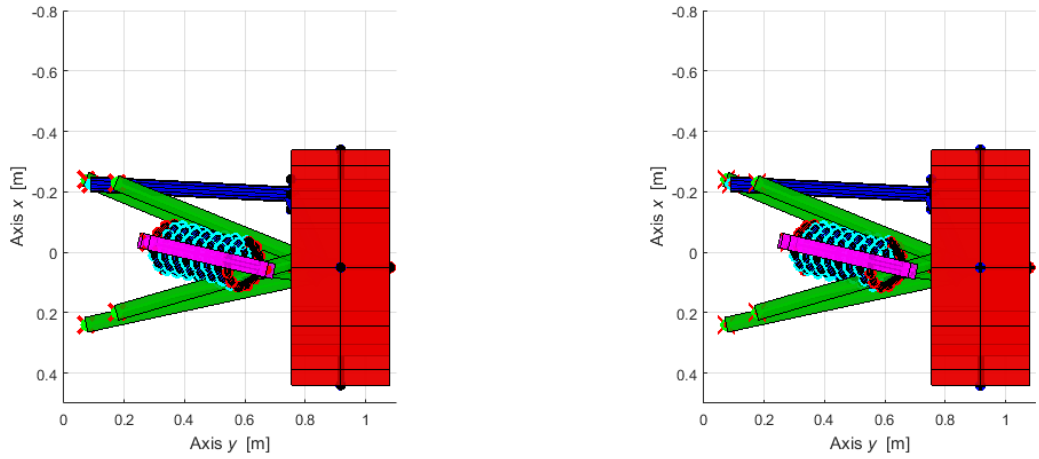

Figure 9.3.8 – Initial (left) and tunned (right) configuration (FL) top view.

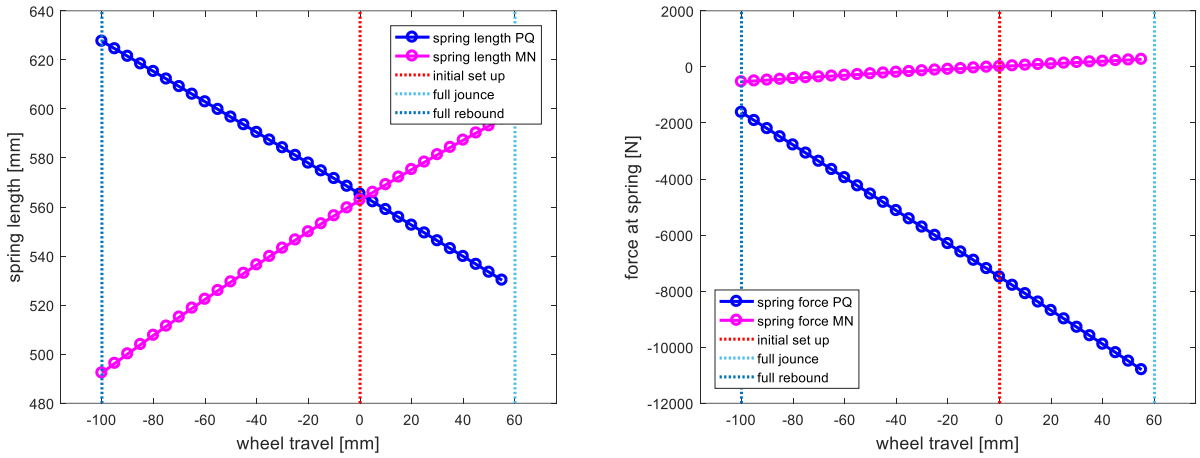

Figure 9.3.9 – Spring length (right) and force (left) of the tunned system vs. wheel travel.

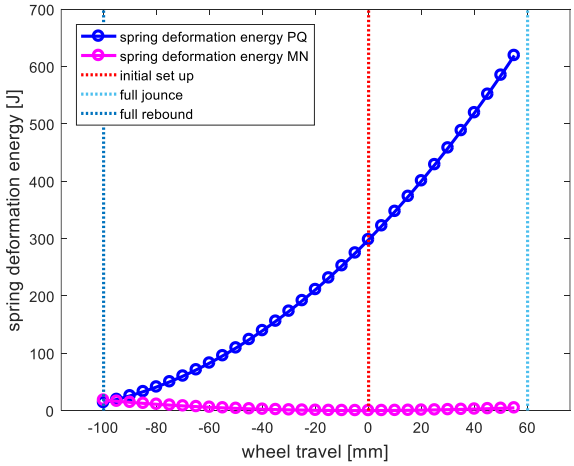

Figure 9.3.10 – Spring deformation energy vs. wheel travel.

Since the geometry of the structure is modified, the spring length MN consequently varies differently compared to initial configuration, and the structure is not in a square shape in the static state either. The spring rates are tunned according to the target stiffness at the same time, k_{s1} is

increased up to 94224.44N/m instead of 50979.35N/m, and k_{s2} is decreased to 7734.3N.m instead of 50979.35N/m. This indicates that spring k_{s2} dominates the nonlinearity of the system, and a higher k_{s2} brings more softening effect into the system. With the tunned spring rates, the spring k_{s1} withstands more loads and absorbs more kinematic energy compared to the initial configuration, while k_{s2} acts as an auxiliary partition in the system to adjust nonlinear performance of the structure. The following figures report the major results for the optimized configuration, individuated by the optimized setting. To facilitate the comparison, the curves for the original GT configuration and the initial nonlinear configuration are also included in the same graph.

In Figure 9.3.11, the wheel rate for the initial nonlinear configuration, the target wheel rate considered as reference in the objective function, and the results of the optimized solution are depicted. It is noticeable that the wheel rate is well-modified according to the target line, and from full rebound up to full jounce, the target and the optimized curves closely algin. Only in the two ends, there is a slight increase in the error between the two curves. This indicates the successful realization of our target and highlights the tunability of the structure.

Another relevant aspect to be considered is the stiffness value reached by the optimized configuration, as shown in Figure 9.3.12. In static state, the equivalent stiffness is a slightly lower than the initial one. Throughout the whole wheel travel of the suspension, the wheel rate is controlled in the narrow range of [43500N/m 44700N/m], it achieves a more constant and flattened wheel rate compared to the GT configuration, despite the tunned structure shows a nonmonotonic behaviour. The proposed structure introduces a unique effect to the suspension, compensating the hardening effect of the linear GT configuration and improving the ride quality with reference to the traditional suspension.

Figure 9.3.13 shows that the force of the equivalent spring varies in a more similar range for the optimized configuration compared to GT configurations, aligning with our intentions. In the last figure, which reports the vertical force at the wheel as a function of the wheel travel, minor differences are observed reaching full rebound and full jounce. Compared to the GT configuration, the optimized structure maintains a similar level of wheel load, effectively balancing the burdensome hardening effect. This promotes mechanical traction force during acceleration, and the nearly constant wheel rate contributes to an improved ride quality for the vehicle.

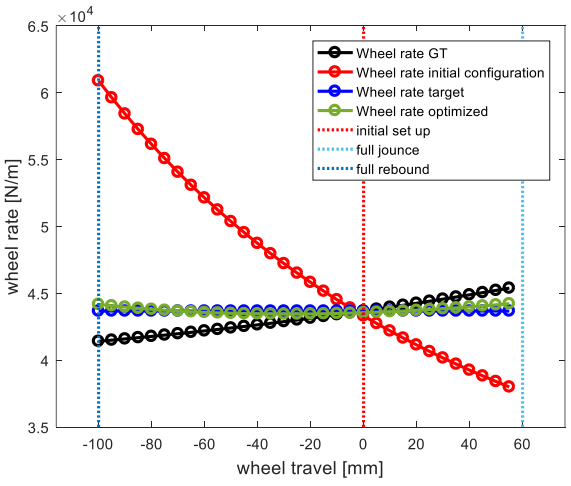

Figure 9.3.11 – Wheel rate comparison (FL).

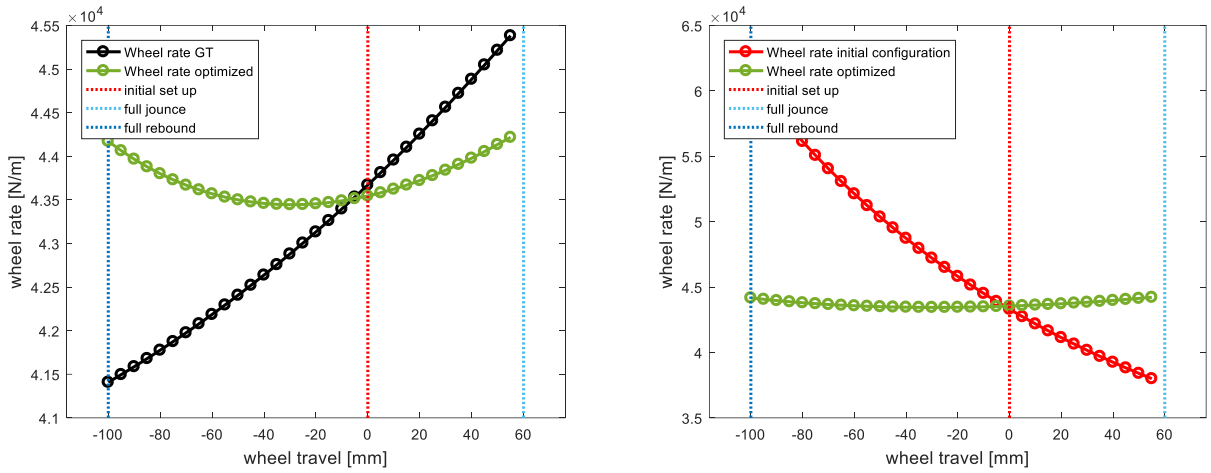

Figure 9.3.12 – Wheel rate of GT, initial nonlinear and optimized nonlinear configurations (FL).

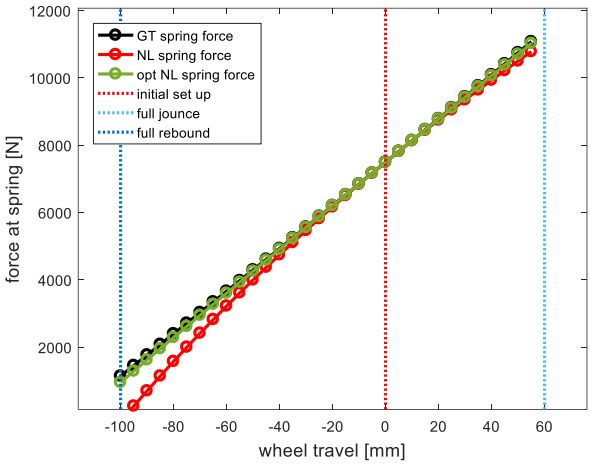

Figure 9.3.13 – Equivalent spring force in GT, initial NL and optimized NL configurations (FL).

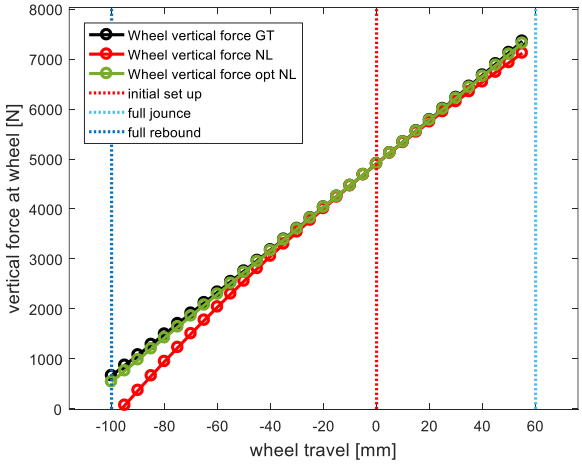

Figure 9.2.14 – Vertical force at wheel in GT, initial NL and optimized NL configurations (FL).

Conclusions and future work

In this research, drawing inspiration from the QZS system in the field of vibration isolation and building on recent studies exploring the feasibility of utilizing QZS in vehicle suspension, we have proposed a new typology of structure with a unique quadrilateral shape, featuring a delightful performance in terms of the vehicle dynamical response. In the initial stage of our research, we conducted a comprehensive analysis of both a coarse model and a refined modal to establish the kinematic model of the innovative quadrilateral structure. By analysing the FBDs of the system, we obtain the dynamical model of the system, with the motion of the system dictated by the displacement h. This allowed us to represent the structure as a SDOF system, providing an effective means to describe its dynamics. The EOM of the whole system was then derived from the ODE of each component, revealing a highly nonlinear characteristic arising from both the nonlinear inertia force and the nonlinear stiffness force. To delve into the nonlinear characteristics, we initially simplified the problem by analysing the linearized response at three specific positions. This involved exploring the equivalent mass, equivalent stiffness, and frequency response at these positions, as detailed in Chapter 7. To gain a more profound understanding of the system's nonlinear behaviour, we employed Simulink to model the nonlinear system numerically. With the analysis of the step response of the nonlinear model in Chapter 8, unique performances of the equivalent suspension structure are highlighted. The analysis reveals that the effectiveness of the nonlinear stiffness dominants the nonlinearity of the system, with the rotational unit's inertia effects being negligible. The application of Hilbert transform further illustrates the instantaneous frequency characteristics of the nonlinear system, indicating varied behaviour at each instance while maintaining an equivalent response to external environment. Finally, we validated our system by comparing it with a double-wishbone suspension in a conventional configuration, reaffirming the tuneable and customable advantages of our innovative structure.

Aimed at optimizing ride comfort for road vehicles, our new suspension system employs a dual-phase response, incorporating a softening effect during compression to effectively absorb road shocks. In the rebound phase, it introduces a hardening effect, enhancing stability and agility. This groundbreaking approach not only enhances passenger ride comfort but also bolsters vehicle handling, resulting in a smoother ride and better tire-road contact. Also, this system exhibits a wide tunability aligned with the design target with a simple method and low cost.

However, it's important to strike the right balance to achieve the optimal suspension characteristics. An extreme soft suspension increases the rattle space requirements, while an overly stiff suspension can compromise ride comfort, leading to a harsher and less comfortable driving experience, especially on rough roads. Moreover, further analysis is necessary to assess the sensitivity of the typology of the structural to the nonlinearity of the system, unlocking more potential in the structure. To uncover more nonlinear behaviour of the structure, other types of excitations such as impulse, pulse and ramp inputs could be explored to evaluate the performance of the nonlinear system in comparison to the linear one. Since we only verified the structure with a double-wishbone structure, considering other types of suspensions for evaluating the performance with this innovative structure is a potential avenue for future research. And a comprehensive examination of the longitudinal and lateral performance of a full vehicle model, incorporating such a novel structure, is essential. The presence of residual displacement in the response of the vehicle, especially with low damping ratios due to the lower effective stiffness of the QZS suspension, prompts the need for more sophisticated models, including the damping terms. Finally, this thesis provides a first insight to comprehend such a new structure, the limitations, such as space constraints and assembly methods, should be addressed for potential commercial applications of this innovative suspension system.

In summary, suspension design is a complex process that requires a delicate balance between ride comfort and handling. Fortunately, now we are feasible to adjust the performance of the suspension using such a sample and novel structure, which provides a smoother ride and enables fine-tuning of

the suspension to meet specific ride comfort and performance goals in a simple manner and with relatively low cost.

Appendix

A

Matrix **M** column 1-6:

$$\mathbf{M}=\begin{bmatrix}
\left(\frac{1}{2}-\frac{\tan(\pi-\delta)}{4D_1(h)}\right)m_1 & -\frac{m_1}{4D_1(h)} & -\frac{I_1}{L_1D_1(h)\cos(\pi-\delta)} & 0 & 0 & 0\\
-\left(\frac{1}{4}-\frac{\tan(\pi-\delta)}{4D_1(h)}\right)\tan(\pi-\delta)m_1 & \left(\frac{1}{4}+\frac{\tan(\pi-\delta)}{4D_1(h)}\right)m_1 & -\frac{I_1\tan(\gamma)}{L_1D_1(h)\cos(\pi-\delta)} & 0 & 0 & 0\\
\left(\frac{1}{4}-\frac{\tan(\pi-\delta)}{4D_1(h)}\right)\tan(\pi-\delta)m_1 & \left(\frac{1}{4}-\frac{\tan(\pi-\delta)}{4D_1(h)}\right)m_1 & \frac{I_1\tan(\gamma)}{L_1D_1(h)\cos(\pi-\delta)} & 0 & 0 & 0\\
\left(\frac{1}{2}-\frac{\tan(\alpha)}{4D_2(h)}\right)m_2 & \frac{m_2}{4D_2(h)} & 0 & \left(\frac{1}{2}-\frac{\tan(\alpha)-\tan(\pi-\beta)}{4D_2(h)}\right)m_2 & \frac{m_2}{2D_2(h)} & -\frac{I_2}{L_2D_2(h)\cos(\alpha)}\\
\frac{\tan(\alpha)\tan(\pi-\beta)}{4D_2(h)}m_2 & \left(\frac{1}{2}-\frac{\tan(\pi-\beta)}{4D_2(h)}\right)m_2 & 0 & \left(\frac{1}{4}+\frac{\tan(\alpha)-\tan(\pi-\beta)}{4D_2(h)}\right)\tan(\pi-\beta)m_2 & \left(\frac{3}{4}-\frac{\tan(\pi-\beta)}{2D_2(h)}\right)m_2 & \frac{I_2\tan(\pi-\beta)}{L_2D_2(h)\cos(\alpha)}\\
-\frac{\tan(\alpha)\tan(\pi-\beta)}{4D_2(h)}m_2 & \frac{\tan(\pi-\beta)}{4D_2(h)}m_2 & 0 & -\left(\frac{1}{4}+\frac{\tan(\alpha)-\tan(\pi-\beta)}{4D_2(h)}\right)\tan(\pi-\beta)m_2 & \left(-\frac{1}{4}+\frac{\tan(\pi-\beta)}{2D_2(h)}\right)m_2 & -\frac{I_2\tan(\pi-\beta)}{L_2D_2(h)\cos(\alpha)}\\
\frac{\tan(\alpha)}{4D_2(h)}m_3 & -\frac{m_3}{4D_2(h)} & 0 & \left(\frac{1}{2}+\frac{\tan(\alpha)-\tan(\pi-\beta)}{4D_2(h)}\right)m_3 & -\frac{m_3}{2D_2(h)} & \frac{I_2}{L_2D_2(h)\cos(\alpha)}\\
-\frac{\tan(\alpha)\tan(\pi-\beta)}{4D_2(h)}m_3 & \frac{\tan(\pi-\beta)}{4D_2(h)}m_3 & 0 & -\left(\frac{1}{4}+\frac{\tan(\alpha)-\tan(\pi-\beta)}{4D_2(h)}\right)\tan(\pi-\beta)m_3 & \left(\frac{1}{4}+\frac{\tan(\pi-\beta)}{2D_2(h)}\right)m_3 & -\frac{I_2\tan(\pi-\beta)}{L_2D_2(h)\cos(\alpha)}\\
\frac{\tan(\alpha)\tan(\pi-\beta)}{4D_2(h)}m_3 & -\frac{\tan(\pi-\beta)}{4D_2(h)}m_3 & 0 & \left(\frac{1}{4}+\frac{\tan(\alpha)-\tan(\pi-\beta)}{4D_2(h)}\right)\tan(\pi-\beta)m_3 & \left(\frac{1}{4}-\frac{\tan(\pi-\beta)}{2D_2(h)}\right)m_3 & \frac{I_2\tan(\pi-\beta)}{L_2D_2(h)\cos(\alpha)}\\
\frac{\tan(\pi-\delta)}{4D_1(h)}m_4 & \frac{m_4}{4D_1(h)} & \frac{I_1}{L_1D_1(h)\cos(\pi-\delta)} & 0 & 0 & 0\\
\left(\frac{1}{4}-\frac{\tan(\pi-\delta)}{4D_1(h)}\right)\tan(\pi-\delta)m_4 & \left(\frac{1}{4}-\frac{\tan(\pi-\delta)}{4D_1(h)}\right)m_4 & \frac{I_1\tan(\gamma)}{L_1D_1(h)\cos(\pi-\delta)} & 0 & 0 & 0\\
-\left(\frac{1}{4}-\frac{\tan(\pi-\delta)}{4D_1(h)}\right)\tan(\pi-\delta)m_4 & \left(-\frac{1}{4}+\frac{\tan(\pi-\delta)}{4D_1(h)}\right)m_4 & -\frac{I_1\tan(\gamma)}{L_1D_1(h)\cos(\pi-\delta)} & 0 & 0 & 0
\end{bmatrix}$$

Matrix **M** column 7-12:

$$\begin{bmatrix}
\frac{\tan(\gamma)}{4D_1(h)}m_1 & -\frac{m_1}{4D_1(h)} & 0 & \left(\frac{1}{2}-\frac{\tan(\pi-\delta)-\tan(\gamma)}{4D_1(h)}\right)m_1 & -\frac{m_1}{2D_1(h)} & -\frac{I_4}{L_4D_1(h)\cos(\gamma)}\\
-\frac{\tan(\gamma)\tan(\pi-\delta)}{4D_1(h)}m_1 & \frac{\tan(\pi-\delta)}{4D_1(h)}m_1 & 0 & \left(-\frac{1}{4}+\frac{\tan(\pi-\delta)-\tan(\gamma)}{4D_1(h)}\right)\tan(\pi-\delta)m_1 & \left(\frac{1}{4}+\frac{\tan(\pi-\delta)}{2D_1(h)}\right)m_1 & \frac{I_4\tan(\pi-\delta)}{L_4D_1(h)\cos(\gamma)}\\
\frac{\tan(\gamma)\tan(\pi-\delta)}{4D_1(h)}m_1 & -\frac{\tan(\pi-\delta)}{4D_1(h)}m_1 & 0 & \left(\frac{1}{4}-\frac{\tan(\pi-\delta)-\tan(\gamma)}{4D_1(h)}\right)\tan(\pi-\delta)m_1 & \left(\frac{1}{4}-\frac{\tan(\pi-\delta)}{2D_1(h)}\right)m_1 & -\frac{I_4\tan(\pi-\delta)}{L_4D_1(h)\cos(\gamma)}\\
\frac{\tan(\pi-\beta)}{4D_2(h)}m_2 & \frac{m_2}{4D_2(h)} & -\frac{I_3}{L_3D_2(h)\cos(\pi-\beta)} & 0 & 0 & 0\\
\left(\frac{1}{4}-\frac{\tan(\pi-\beta)}{4D_2(h)}\right)\tan(\pi-\beta)m_2 & \left(\frac{1}{4}-\frac{\tan(\pi-\beta)}{4D_2(h)}\right)m_2 & -\frac{I_3\tan(\alpha)}{L_3D_2(h)\cos(\pi-\beta)} & 0 & 0 & 0\\
-\left(\frac{1}{4}-\frac{\tan(\pi-\beta)}{4D_2(h)}\right)\tan(\pi-\beta)m_2 & \left(-\frac{1}{4}+\frac{\tan(\pi-\beta)}{4D_2(h)}\right)m_2 & \frac{I_3\tan(\alpha)}{L_3D_2(h)\cos(\pi-\beta)} & 0 & 0 & 0\\
\left(\frac{1}{2}-\frac{\tan(\pi-\beta)}{4D_2(h)}\right)m_3 & -\frac{m_3}{4D_2(h)} & \frac{I_3}{L_3D_2(h)\cos(\pi-\beta)} & 0 & 0 & 0\\
-\left(\frac{1}{4}-\frac{\tan(\pi-\beta)}{4D_2(h)}\right)\tan(\pi-\beta)m_3 & \left(\frac{1}{4}+\frac{\tan(\pi-\beta)}{4D_2(h)}\right)m_3 & \frac{I_3\tan(\alpha)}{L_3D_2(h)\cos(\pi-\beta)} & 0 & 0 & 0\\
\left(\frac{1}{4}-\frac{\tan(\pi-\beta)}{4D_2(h)}\right)\tan(\pi-\beta)m_3 & \left(\frac{1}{4}-\frac{\tan(\pi-\beta)}{4D_2(h)}\right)m_3 & -\frac{I_3\tan(\alpha)}{L_3D_2(h)\cos(\pi-\beta)} & 0 & 0 & 0\\
\left(\frac{1}{2}-\frac{\tan(\gamma)}{4D_1(h)}\right)m_4 & \frac{m_4}{4D_1(h)} & 0 & \left(\frac{1}{2}+\frac{\tan(\pi-\delta)-\tan(\gamma)}{4D_1(h)}\right)m_4 & \frac{m_4}{2D_1(h)} & \frac{I_4}{L_4D_1(h)\cos(\gamma)}\\
\frac{\tan(\gamma)\tan(\pi-\delta)}{4D_1(h)}m_4 & \frac{1}{2}-\frac{\tan(\pi-\delta)}{4D_1(h)} & 0 & \left(\frac{1}{4}-\frac{\tan(\pi-\delta)-\tan(\gamma)}{4D_1(h)}\right)\tan(\pi-\delta)m_4 & \left(\frac{3}{4}-\frac{\tan(\pi-\delta)}{2D_1(h)}\right)m_4 & -\frac{I_4\tan(\pi-\delta)}{L_4D_1(h)\cos(\gamma)}\\
-\frac{\tan(\gamma)\tan(\pi-\delta)}{4D_1(h)}m_4 & \frac{\tan(\pi-\delta)}{4D_1(h)}m_4 & 0 & \left(-\frac{1}{4}+\frac{\tan(\pi-\delta)-\tan(\gamma)}{4D_1(h)}\right)\tan(\pi-\delta)m_4 & \left(-\frac{1}{4}+\frac{\tan(\pi-\delta)}{2D_1(h)}\right)m_4 & \frac{I_4\tan(\pi-\delta)}{L_4D_1(h)\cos(\gamma)}
\end{bmatrix}$$

B

$$\mathbf{F_k} = F_{s2}\begin{Bmatrix} -\frac{N_1(h)}{D_1(h)} + \cos(\theta_2) \\ \left(\frac{N_1(h)}{D_1(h)} - \cos(\theta_2)\right)\tan(\pi-\delta) \\ \left(-\frac{N_1(h)}{D_1(h)} + \cos(\theta_2)\right)\tan(\pi-\delta) \\ \frac{N_2(h)}{D_2(h)} - \cos(\theta_2) \\ -\frac{N_2(h)}{D_2(h)}\tan(\pi-\beta) + \sin(\theta_2) \\ \frac{N_2(h)}{D_2(h)}\tan(\pi-\beta) - \sin(\theta_2) \\ -\frac{N_2(h)}{D_2(h)} \\ \frac{N_2(h)}{D_2(h)}\tan(\pi-\beta) \\ -\frac{N_2(h)}{D_2(h)}\tan(\pi-\beta) \\ \frac{N_1(h)}{D_1(h)} \\ \left(-\frac{N_1(h)}{D_1(h)} + \cos(\theta_2)\right)\tan(\pi-\delta) - \sin(\theta_2) \\ \left(\frac{N_1(h))}{D_1(h)} - \cos(\theta_2)\right)\tan(\pi-\delta) + \sin(\theta_2) \end{Bmatrix}$$

C

$$\mathbf{M} = \begin{bmatrix} \frac{3}{8}m & -\frac{m}{8\tan(\alpha)} & -\frac{I_1}{2L_1\sin(\alpha)} & 0 & 0 & 0 & \frac{1}{8}m & -\frac{m}{8\tan(\alpha)} & 0 & \frac{1}{2}m & -\frac{1}{4\tan(\alpha)}m & -\frac{I_4}{2L_4\sin(\alpha)} \\ -\frac{\tan(\alpha)}{8}m & \frac{3}{8}m & -\frac{I_1}{2L_1\cos(\alpha)} & 0 & 0 & 0 & -\frac{\tan(\alpha)}{8}m & \frac{1}{8}m & 0 & -\frac{\tan(\alpha)}{4}m & \frac{1}{2}m & \frac{I_4}{2L_4\cos(\alpha)} \\ \frac{\tan(\alpha)}{8}m & \frac{1}{8}m & \frac{I_1}{2L_1\cos(\alpha)} & 0 & 0 & 0 & \frac{\tan(\alpha)}{8}m & -\frac{1}{8}m & 0 & \frac{\tan(\alpha)}{4}m & 0 & -\frac{I_4}{2L_4\cos(\alpha)} \\ \frac{3}{8}m & \frac{m}{8\tan(\alpha)} & 0 & \frac{1}{2}m & \frac{m}{4\tan(\alpha)} & -\frac{I_2}{2L_2\sin(\alpha)} & \frac{1}{8}m & \frac{m}{8\tan(\alpha)} & -\frac{I_3}{2L_3\sin(\alpha)} & 0 & 0 & 0 \\ \frac{\tan(\alpha)}{8}m & \frac{3}{8}m & 0 & \frac{\tan(\alpha)}{4}m & \frac{1}{2}m & \frac{I_2}{2L_2\cos(\alpha)} & \frac{\tan(\alpha)}{8}m & \frac{1}{8}m & -\frac{I_3}{2L_3\cos(\alpha)} & 0 & 0 & 0 \\ -\frac{\tan(\alpha)}{8}m & \frac{1}{8}m & 0 & -\frac{\tan(\alpha)}{4}m & 0 & -\frac{I_2}{2L_2\cos(\alpha)} & -\frac{\tan(\alpha)}{8}m & -\frac{1}{8}m & \frac{I_3}{2L_3\cos(\alpha)} & 0 & 0 & 0 \\ \frac{1}{8}m & -\frac{m}{8\tan(\alpha)} & 0 & \frac{1}{2}m & -\frac{m}{4\tan(\alpha)} & \frac{I_2}{2L_2\sin(\alpha)} & \frac{3}{8}m & -\frac{m}{8\tan(\alpha)} & \frac{I_3}{2L_3\sin(\alpha)} & 0 & 0 & 0 \\ -\frac{\tan(\alpha)}{8}m & \frac{1}{8}m & 0 & -\frac{\tan(\alpha)}{4}m & \frac{1}{2}m & -\frac{I_2}{2L_2\cos(\alpha)} & -\frac{\tan(\alpha)}{8}m & \frac{3}{8}m & \frac{I_3}{2L_3\cos(\alpha)} & 0 & 0 & 0 \\ \frac{\tan(\alpha)}{8}m & -\frac{1}{8}m & 0 & \frac{\tan(\alpha)}{4}m & 0 & \frac{I_2}{2L_2\cos(\alpha)} & \frac{\tan(\alpha)}{8}m & \frac{1}{8}m & -\frac{I_3}{2L_3\cos(\alpha)} & 0 & 0 & 0 \\ \frac{1}{8}m & \frac{m}{8\tan(\alpha)} & \frac{I_1}{2L_1\sin(\alpha)} & 0 & 0 & 0 & \frac{3}{8}m & \frac{m}{8\tan(\alpha)} & 0 & \frac{1}{2}m & \frac{1}{4\tan(\alpha)}m & \frac{I_4}{2L_4\sin(\alpha)} \\ \frac{\tan(\alpha)}{8}m & \frac{1}{8}m & \frac{I_1}{2L_1\cos(\alpha)} & 0 & 0 & 0 & \frac{\tan(\alpha)}{8}m & \frac{3}{8}m & 0 & \frac{\tan(\alpha)}{4}m & \frac{1}{2}m & -\frac{I_4}{2L_4\cos(\alpha)} \\ -\frac{\tan(\alpha)}{8}m & -\frac{1}{8}m & -\frac{I_1}{2L_1\cos(\alpha)} & 0 & 0 & 0 & -\frac{\tan(\alpha)}{8}m & \frac{1}{8}m & 0 & -\frac{\tan(\alpha)}{4}m & 0 & \frac{I_4}{2L_4\cos(\alpha)} \end{bmatrix}$$

D

$$\mathbf{F_k} = F_{s2}\begin{Bmatrix} \frac{1}{2} \\ -\frac{\tan(\alpha)}{2} \\ \frac{\tan(\alpha)}{2} \\ -\frac{1}{2} \\ -\frac{\tan(\alpha)}{2}) \\ \frac{\tan(\alpha)}{2} \\ -\frac{1}{2} \\ \frac{\tan(\alpha)}{2} \\ -\frac{\tan(\alpha)}{2} \\ \frac{1}{2} \\ \frac{\tan(\alpha)}{2} \\ -\frac{\tan(\alpha)}{2} \end{Bmatrix}$$

E

$$\ddot{\mathbf{z}} = \begin{Bmatrix} \ddot{x}_O \\ \ddot{y}_O \\ \ddot{\delta} \\ \ddot{x}_N \\ \ddot{y}_N \\ \ddot{\alpha} \\ \ddot{x}_P \\ \ddot{y}_P \\ \ddot{\beta} \\ \ddot{x}_M \\ \ddot{y}_M \\ \ddot{\gamma} \end{Bmatrix} = \begin{Bmatrix} 0 \\ 0 \\ \frac{1}{\sqrt{4L^2 - (y_{Po}+h)^2}} \\ \frac{y_{Po}+h}{2\sqrt{4L^2 - (y_{Po}+h)^2}} \\ 1/2 \\ -\frac{1}{\sqrt{4L_2{}^2 - (y_{Po}+h)^2}} \\ 0 \\ 1 \\ \frac{1}{\sqrt{4L^2 - (y_{Po}+h)^2}} \\ -\frac{y_{Po}+h}{2\sqrt{4L^2 - (y_{Po}+h)^2}} \\ 1/2 \\ -\frac{1}{\sqrt{4L^2 - (y_{Po}+h)^2}} \end{Bmatrix} \ddot{h} + \begin{Bmatrix} 0 \\ 0 \\ \frac{y_{Po}+h}{\left(4L^2 - (y_{Po}+h)^2\right)^{3/2}} \\ \frac{2L^2}{\left(4L^2 - (y_{Po}+h)^2\right)^{3/2}} \\ 0 \\ -\frac{y_{Po}+h}{\left(4L^2 - (y_{Po}+h)^2\right)^{3/2}} \\ 0 \\ 0 \\ \frac{y_{Po}+h}{\left(4L^2 - (y_{Po}+h)^2\right)^{3/2}} \\ -\frac{2L^2}{\left(4L^2 - (y_{Po}+h)^2\right)^{3/2}} \\ 0 \\ -\frac{y_{Po}+h}{\left(4L^2 - (y_{Po}+h)^2\right)^{3/2}} \end{Bmatrix} \dot{h}^2$$

F

```
function [f1,f2,f3] = EOM_nl(h)

% It shows the three nonlinear functions in the EOM of the whole system
% The EOM of the whole is given by
%
% m*f1(h)*d2h/dt2 + m*f2(h)*(dh/dt)^2+ ks1*h + ks2*f3(h) = F
%
% where h is the displacement, m is the mass of the beams, ks1 and ks2 are
% the spring stiffness correspondingly
% f1(h), f2(h), f3(h) are three nonlinear functions incurred by the
% nonlinear inertia and nonlinear stiffness correspondingly

% INPUT:  double  h
%
% OUTPUT: double    f1
%         double    f2
%         double    f3
%         double    Fk
%
%[f1,f2,f3,Fk] = nl(h)

% structural parameters of the system
L = 0.5;       %length [m]
lo2 = 2^0.5/2;  %length at rest of spring2 [m]
yp = -2^0.5/2;  %ordinate of point P at static position [m]
% ks1 = 0;        %spring stiffness1 [N/m]
% ks2 = 36000;    %spring stiffness2 [N/m]
alpha = pi/2-acos((-yp-h)./2/L);
% m = 4.9323;     %mass [kg]
b = (4*L^2-(yp+h)^2); %homogeneous denominator
% nonlinear function f1(h)
f1 = (5/4+(L./(6.*cos(alpha))-(yp+h).*tan(alpha)./4)./b.^0.5);
% nonlinear function f2(h)
f2 = -(L^2.*tan(alpha)-L.*(yp+h)./(6.*cos(alpha))).*b.^1.5;
% nonlinear function f3(h)
f3 = 2*L.*sin(alpha)-lo2.*tan(alpha);
% nonlinear inertia incurred equivalent mass [kg]
% meq = m.f1;
% stiffness force [N]
% Fk = ks1*h+ks2*f3;

end
```

Reference

[1] Technical Committee ISO/TC 108, “Mechanical vibration and shock - Human exposure - Vocabulary,” *International Organization for Standardization*. ISO, 1997

[2] M. J. Johnston, “Development and evaluation of vehicle suspension tuning metrics,” M.A.Sc. thesis, Dept. of Mechanical, Automotive, and Materials Engineering, University of Windsor, Windsor, ON, 2010.

[3] Aizuddin F. M. R., Noreffendy T., Ajat S., Fauzi A., “Review on active suspension system,” *SHS Web of Conferences 49*, 02008, 2018.

[4] Y. M. Elattar, S. M. Metwalli, M. G. Rabie, “PDF VERSUS PID CONTROLLER FOR ACTIVE VEHICLE SUSPENSION”, *AMME-17*, Cairo, Egypt, Apr. 2016.

[5] Muhammad Z. H., Mohd Kamarul H. A. A., Frank D., Matthias R., “Numerical Analysis of Spring Stiffness in Vehicle Design Development Stage,” *International Journal of Applied Engineering*, 2016, pp. 5163-5168.
Numerical analysis of spring stiffness in vehicle design development stage.pdf

[6] Joseph Jerz Jr, “Variable stiffness suspension system”, US Patent 3,559,976, 02-02-1971.
US3559976A - Variable stiffness suspension system - Google Patents.pdf

[7] Jacky Rhein, “Variable-stiffness vehicle suspension system”, US20070013161A1, 18-01-2007.
US20070013161A1 - Variable-stiffness vehicle suspension system - Google Patents.pdf

[8] https://www.steeda.com/mustang-progressive-linear-springs available in 2023-10-25.
Mustang Progressive vs Linear vs Dual-Rate Springs _ Steeda.pdf

[9] https://www.promecha.com.au/springs_advanced.htm available in 2023-10-25.
ProMechA Motorcycle Springs Advanced.pdf

[10] Yanqing Liu, Hiroshi Matsuhisa, Hideo Utsuno, “Semi-active vibration isolation system with variable stiffness and damping control”, *Journal of Sound and Vibration*, 1(2), 2008, pp. 16-28, ISSN 0022-460X.
Semi-active vibration isolation system with variable stiffness.pdf

[11] Shuaishuai Sun, H. Deng, Haiping Du, Weihua Li, Jian Yang, “A Compact Variable Stiffness and Damping Shock Absorber for Vehicle Suspension”, *IEEE/ASME Transactions on Mechatronics*, 20, 2015, pp. 1-9.
A Compact Variable Stiffness and Damping Shock Absorber for Vehicle Suspension.pdf

[12] Olugbenga Anubi, Darsan R. Patel, C. D. Crane, “A new variable stiffness suspension system: Passive case”, *Mechanical Sciences*, 4(1), 2013, pp. 139-151.
A_new_variable_stiffness_suspension_system_Passive.pdf

[13] Alabuzhev P., *Vibration protection and measuring systems with quasi-zero stiffness*, Washington (DC), Hemisphere, 1989.

[14] Chen Z., Chen Z., Wei Y., “Quasi-Zero Stiffness-Based Synchronous Vibration Isolation and Energy Harvesting: A Comprehensive Review”, *Energies 2022*, 15(19), 2022, 7066.
Quasi-Zero Stiffness-Based Synchronous Vibration Isolation and Energy Harvesting_A Comprehensive Review.pdf

[15] Wei Zou, Chun Cheng, Ran Ma, Yan Hu, Weiping Wang, “Performance analysis of a quasi-zero stiffness vibration isolation system with scissor-like structures”, *Archive of Applied Mechanics*, 91(1), 2021, pp. 1-17.
Performance analysis of a quasi-zero stiffness vibration isolation system with scissor-like structures.pdf

[16] Meng Li, Xingjian Jing, “A bistable X-structured electromagnetic wave energy converter with a novel mechanical-motion-rectifier: Design, analysis, and experimental tests”, *Energy Conversion and Management*, 2021, 114466, ISSN 0196-8904.

A bistable X-structured electromagnetic wave energy converter with a novel mechanical-motion-rectifier.pdf

[17] Abolfathi Ali., "Can a nonlinear Quasi-Zero-Stiffness spring improve the ride quality of a vehicle?", *Vehicle System Dynamics*, 2023, pp. 1-17.
Can a nonlinear quasi-zero-stiffness_spring improve the ride quality of a vehicle.pdf

[18] Youcheng Zeng, Hu Ding, Rong-Hua Du, Liqun Chen, "A suspension system with quasi-zero stiffness characteristics and inerter nonlinear energy sink", *Journal of Vibration and Control*, 2020, 0(0) 1–16.
A suspension system with quasi-zero stiffness characteristics and inertrer nonlinear energy sink.pdf

[19] https://www.linkedin.com/pulse/what-difference-between-double-wishbone-mcpherson-multi-link-alex-ren available in 2023-07-03.
What is the difference between Double wishbone, McPherson, Multi-link independent suspension and How them work_LinkedIn.pdf

[20] Carlo N.Belluomo, *Design, Analysis and Investigation of an Independent Suspension for Passenger cars*, MSc Thesis, Politecnico di Torino, Torino, Italy, 2018.

[21] Giulio Allora., *Kinematic and dynamic design of a multi-terrain double-wishbone suspension*, MSc Thesis, Politecnico di Torino, Torino, Italy, 2023.

[22] Gysen B.L.J, Paulides Johannes, Lomonova E.A, *Generalized Harmonic Modeling Technique for 2D Electromagnetic Problems Applied to the Design of a Direct-Drive Active Suspension System*, Phd Thesis, Eindhoven University of Technology, Eindhoven, Netherlands, 2011.

[23] https://www.suspensiondesigner.com/kpi-wheel-rate available in 2023-07-03.
KPI Wheel Rate Suspension Designer.pdf

[24] https://www.focusrs.org/threads/motion-ratios.89266 available in 2023-07-03.
Motion ratio of suspension.pdf

[25] Milliken W.F., Milliken D.L*., Race car vehicle dynamics*, Society of automotive Engineers Inc., Warrendale, 1995.

[26] Woods D.E., Jawad B.A*.,* "Numerical design of racecar suspension parameters", SAE paper 1999-01-2257, 1999.

[27] A. Tonoli, "Car body design chapter 5: NVH." Politecnico di Torino, Torino, pp. 3–3, 2020.

[28] https://www.cs.cmu.edu/~rapidproto/mechanisms/chpt4.html. available in 2023-07-03.
Chapter 4. Basic Kinematics of Constrained Rigid Bodies.pdf

[29] Bonisoli E., Dimauro L., Venturini S., *Lupos: Open-source Scientific Computing in Structural Dynamics*, Politecnico di Torino, Torino, 2022.

[30] Giancarlo Genta, *Vibration dynamics and control*, Politecnico di Torino, Torino, Italy, 2009.

[31] Xiao Feng, Xingjian Jing, Zhaodong Xu, Yingqing Guo, "Bio-inspired anti-vibration with nonlinear inertia coupling", *Mechanical Systems and Signal Processing*, 2019, pp. 562-595, ISSN 0888-3270.
Bio-inspired anti-vibration with nonlinear inertia coupling.pdf

[32] Bonisoli E., Dimauro L, Venturini S., Cavallaro S.P., "Experimental Detection of Nonlinear Dynamics Using a Laser Profilometer", *Appl. Sci*., 2023, 13, 3295. https:// doi.org/10.3390/app13053295.
Bonisoli,DImauro,Venturini,Cavallaro_Experimental detection of nonlinear dynamics using a laser profilometer_MDPI2023_Cover.pdf